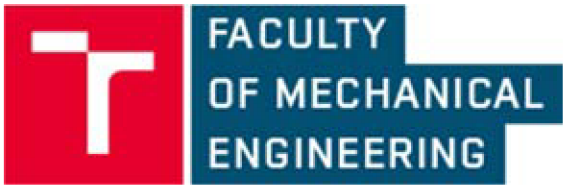

INSTITUTE OF MATERIALS SCIENCE AND ENGINEERING

MECHANICAL REINFORCEMENT OF BIOGLASS®-BASED SCAFFOLDS

DOCTORAL THESIS

AUTHOR Ing. LUCA BERTOLLA

SUPERVISOR Prof. Ing. IVO DLOUHÝ, CSc.

BRNO 2015

Abstract

Bioactive glasses exhibit unique characteristics as a material for bone tissue engineering. Unfortunately, their extensive application for the repair of load-bearing bone defects is still limited by low mechanical strength and fracture toughness. The main aim of this work was two-fold: the reinforcement of brittle Bioglass®-based porous scaffolds and the production of bulk Bioglass® samples exhibiting enhanced mechanical properties. For the first task, scaffolds were coated by composite coating constituted by polyvinyl alcohol (PVA) and microfibrillated cellulose (MFC). The addition of PVA/MFC coating led to a 10 fold increase of compressive strength and a 20 fold increase of tensile strength in comparison with non-coated scaffolds. SEM observations of broken struts surfaces proved the reinforcing and toughening mechanism of the composite coating which was ascribed to crack bridging and fracture of cellulose fibrils. The mechanical properties of the coating material were investigated by tensile testing of PVA/MFC stand–alone specimens. The stirring time of the PVA/MFC solution came out as a crucial parameter in order to achieve a more homogeneous dispersion of the fibres and consequently enhanced strength and stiffness. Numerical simulation of a PVA coated Bioglass® strut revealed the infiltration depth of the coating until the crack tip as the most effective criterion for the struts strengthening. Contact angle and linear viscosity measurements of PVA/MFC solutions showed that MFC causes a reduction in contact angle and a drastic increase in viscosity, indicating that a balance between these opposing effects must be achieved. Concerning the production of bulk samples, conventional furnace and spark plasma sintering technique was used. Spark plasma sintering performed without the assistance of mechanical pressure and at heating rates ranging from 100 to 300°C /min led to a material having density close to theoretical one and fracture toughness nearly 4 times higher in comparison with conventional sintering. Fractographic analysis revealed the crack deflection as the main toughening mechanisms acting in the bulk Bioglass®. Time–dependent crack healing process was also observed. The further investigation on the non-equilibrium phases crystallized is required. All obtained results are discussed in detail and general recommendations for scaffolds with enhanced mechanical resistance are served.

Keywords

Bioactive glass, scaffolds, composite material, mechanical properties, tensile test, SPS.

Bibliographic citation

BERTOLLA, L. *Mechanical Reinforcement of Bioglass®-Based Scaffolds.* Brno: Brno University of Technology, Faculty of Mechanical Engineering, 2016. 123 pp. Supervisor Prof. Ing. Ivo Dlouhý, CSc..

Acknowledgments

My greatest gratitude and appreciation goes to my supervisor Prof. Ing. Ivo Dlouhý, CSc. who gave me the opportunity to start my doctoral studies at the Institute of Physics of Materials in Brno in the framework of the European project GlaCERCo. I want to thank him for his support, trust and advices during all stages of my Ph. D. and also for giving me the freedom to develop my own research ideas. I also want to thank him for encouraging me to participate to several conferences and working experiences abroad, including stays in Erlangen, Torino, London, Bremen, Limoges, Phoenix and Vinci, which have had huge impact both on my scientific career and on my personal growth. I want to thank Dr. Zdeněk Chlup who has been supporting me from the very beginning of my doctoral studies, by helping me with my experiments and any practical issue I faced in the laboratory. He has always succeeded to motivate me in all my efforts and I also thank him for creating an extremely nice working atmosphere. I gratefully acknowledge Prof. Aldo Boccaccini for the support and the availability he always offered me along these three years, giving me the chance to stay at the Biomaterials department in Erlangen-Nurnberg University for the accomplishment of my preliminary experiments. My gratitude goes also to his Ph. D. students as well, in particular to Anahi Phillippart who gave me very useful tips on the production of scaffolds at the beginning of my research activity. I thank Dr. Luděk Stratil for the restless support he always provided me, for helping me with computational analysis and for solving the demanding bureaucratic issues connected to my studies. I also want to thank Dr. Peter Tatarko, who supported me since the very beginning of my stay in Brno and helped me to solve several practical issues. I also thank him for the help he gave me for the production of sample by spark plasma sintering at Nanoforce and for the hilarious talks we had, which definitely cheered me up and helped me to overcome difficult hours in the lab. I want to thank Prof. Nikilesh Chawla, Dr. Jason Williams and Dr. James Mertens for the kindness and help they offered me during my stay at Arizona State University and the μ-tomography scans of scaffolds. All collaborators who contributed to the completion of this Ph. D. work are gratefully acknowledged, in particular: Dr. Eva Bartoníčkova for the viscosimetry analysis, Dr. James Mertens, Dr. Jiří Buršík for TEM images of boron nitride nanosheets, Dr. Pavla Roupcová for the XRD analysis of sintered Bioglass samples, Dr. Ali Moosavifar and Borregard for supplying the microfibrillated cellulose, Ing. Pavel Čupera, Ing. Radek Vácha for the help with sample preparation and settings of machines and Dr. Oldřich Ševeček for the evaluation of μ-tomography results. Immense gratitude goes also to Prof. Milena Salvo, Prof. Monica Ferraris and Dr. Cristiana Contardi, who made my long journey started through the project GlaCERCo and provided me constant support along these three years.

I would like to heartily thank one by one all my colleagues from Brittle Fracture Group in IPM and all the new friends I met in Brno, who shared with me many experiences and moments, for their warm welcome and honest friendship which rendered these three years unforgettable. My final thank goes to my parents and to Lydia for the love and support they gave me along all these years.

Financial support from GlaCERCo - ITN EU project, Contract No. 264526 within Marie-Curie Action “Initial Training Networks” is acknowledged. A part of the research has been carried out thanks to financial support of Czech Science Foundation, project Nr. 14-112345.

Claim

I hereby confirm that I am the sole author of the written work here enclosed and that I have compiled it in my own words. The work was made under the supervision of Prof. Ing. Ivo Dlouhý, CSc..

Brno, 5.11.2015 …….

Ing. Luca Bertolla

Institute of Materials Science and Engineering
Faculty of Mechanical Engineering
Brno University of Technology

and

Institute of Physics of Materials
Academy of Science of the Czech Republic
Brno

bertolla@ipm.cz

Content

1. Introduction

Diseases, injuries and traumas might lead to damage and degeneration of human tissues, which then necessitate to be treated in order to facilitate its repair or regeneration. Nowadays, millions of implants are needed to improve the standards of life of the aging population. As a consequence, the materials science is facing since decades the challenge of developing advanced and multifunctional biomaterials able to substitute, permanently or temporarily the damaged parts. In the case of bone tissue engineering, such materials are required when a section of bone is missing and the gap needs to be filled in, for instance following an accident or after the removal of a tumor. There are several options for this type of bone replacement [1, 2]:

- *Allografts* involve using material from another patient. However, there are risks of infection and the implant being rejected, and the strength of the replacement bone may be reduced due to sterilization.
- *Autografts* involve using material from the same patient, but from a different site (such as the pelvis). Although this reduces the chances of rejection, there is a limited amount of material available, and two surgical procedures are needed, leading to more pain and a higher risk of infection.
- *Synthetic materials* are gradually becoming more popular. They can be prepared in laboratory, and properties can be tailored according to the specific clinical requirement.

Anyhow these methods still face serious constraints due to problems with accessing enough tissue for all of the patients who require them and the fact that there are risks of rejection by the patient's immune system. The possibility of introducing infections or diseases from the donor to the patient also constitutes an additional risk. A suitable alternative is offered by tissue engineering (TE), whose aim is to regenerate damaged tissues, instead of replacing them, by developing artificial biological substitutes that restore, maintain or improve tissue function [3]. From this standpoint, it can be stated that the main aim of bone TE is to restore and maintain the function of human bone tissues. To accomplish such demanding task, three-dimensional resorbable porous structures, able to trigger the formation of living tissue are required. Their surface should allow cells to attach, proliferate and differentiate [4]. Specialized scientific literature termed these structures as “scaffolds”. During the last 20 years, ceramics started to be widely used in medical applications. According to their interaction with the surrounding living tissue, they can be classified in four categories [5]:

- *Nearly inert* whose fixation take place by mechanical interaction or morphological fixation (e. g. alumina and zirconia femoral heads);
- *Porous* whose fixation is due biological ingrowth into implant pores (e. g. hydroxyapatite (HA) and HA–coated porous metals used for femoral stems);
- *Bioactive* for which the fixation occurs by chemical bonding with implant and tissues (e. g. bioactive glasses (BGs) used for dental and orthopaedic devices);
- *Resorbable* if the fixation occurs through replacement of the implant by living tissue.

Unfortunately biologically derived transplants appear to be imperfect solutions, mainly due to a restricted quantity of donor tissues, donor site morbidity as well as potential risks of an immunological incompatibility and disease transfer [2]. In this light, manmade materials (alloplastic or synthetic bone grafts) stand out as a reasonable option, because they are easily available and might be processed and modified to suit the specific needs of a given application [6]. Concerns about potential infections, immunological incompatibility, sterility or donor site morbidity are thus avoided.

The concept of bioactive ceramics was introduced in 1969 by Hench et al. [7]. This led to the standard definition of bioactivity: a "bioactive" material is one that elicits a specific biological response at the interface of the material which results in the formation of bond between tissues and material itself. Bioactive glasses and in particular, 45S5 Bioglass®, started to be intensively studied for the production of scaffolds because of their outstanding ability to transform in the human body, into hydroxyapatite and bond to living bone. Anyhow, one of the biggest difficulties in the production of porous bioactive scaffolds from 45S5 Bioglass® is due that the crystallization of different phases, which hinder the densification process. Progresses have been achieved from this perspective, by understanding how the glass composition can be tailored to prevent crystallization or by modifying the processing parameters in certain way. The problems encountered during sintering can be avoided by synthesizing sol–gel glass, where the silica network is assembled at room temperature. Developments in foaming, solid freeform fabrication and nanofibre spinning have now allowed the production of porous bioactive glass scaffolds from both melt– and sol–gel–derived glasses [8].

Beside the difficulties encountered during sintering, the low strength and intrinsic brittleness which characterize these materials still constitute a further crucial issue, which prevents their extensive use in all the load-bearing applications. The key-problem is that most of materials suitable for in-vivo application are not simultaneously mechanically competent and bioresorbable [9]. Mechanically strong materials are usually bioinert, while bioresorbable and degradable materials are in general mechanically weak [10]. This aspect becomes even more critical as these materials are processed in order to obtain highly porous reticulated structures. Therefore, a methodology which enables the production of BGs-based scaffolds with superior mechanical properties has to be developed. Bone is considered to be a composite material consisting of a high elastic modulus mineral 'fibres' embedded in a low elastic modulus organic matrix permeated with pores filled with liquids [11]. Thus, the combination of softer synthetic polymers and stiff inorganic materials such as glasses and ceramics has been attempted in order to obtain scaffolds which somehow mimic the structure of living bone [12]. Ideally, composites should provide enhanced mechanical performances and obtain properties that are unavailable from the individual constituent materials.

2. Theoretical background

Tissue engineering is emerging as a significant potential alternative or complementary solution, whereby tissue and organ failure is addressed by implanting natural, synthetic, or semisynthetic tissue and organ mimics that are fully functional from the start, or that grow into the required functionality. An increasing number of tissue types are now being engineered, as well as biomaterials and scaffolds used as delivery systems. A variety of approaches are used to entice differentiated or undifferentiated cells, such as stem cells, into the desired cell type. Notable results include tissue-engineered bone, blood vessels, liver, muscle, and even nerve conduits. As a result of the medical and market potential, there is significant academic and corporate interest in this technology.

2.1. Scaffolds for hard tissue engineering

As they are implanted into bone defects, these structures should induce and direct the growth of new bone in three dimensions and simultaneously undergo progressive degradation. In other words, scaffolds should act as temporary template to guide bone repair. Additional elements, such as growth factors, cells (seeded on template surface and cultured in vitro), can be coated onto the surface or even incorporated into them. An ideal scaffold should therefore exhibit the following properties [13]:

- Biocompatibility and bioactivity, promoting osteogenic cell attachment and osteogenesis;
- To avoid the formation of fibrous tissue;
- To exhibit an interconnected porous structure allowing fluid flow, cell migration, bone in growth and vascularization of tissue;
- To have suitable degradation rate;
- An appropriate level of mechanical properties in order to avoid failure during and after surgery;
- To be sterilizable and meet regulatory requirements for clinical use.

Some of these properties are interlinked and opposing. Scaffolds development is therefore a demanding task since it requires multi-disciplinary knowledge of biology, chemistry and materials engineering. Bioactive glass-ceramics belong to the group of Class A bioactive materials, which are characterized by both osteoconduction (*i.e.*, growth of bone at the implant surface) and osteoinduction (*i.e.*, activation and recruitment of osteoprogenitor cells by the material itself stimulating bone growth on the surface of the material) [14]. Differences between Class A and B bioactive materials are discussed elsewhere [15].

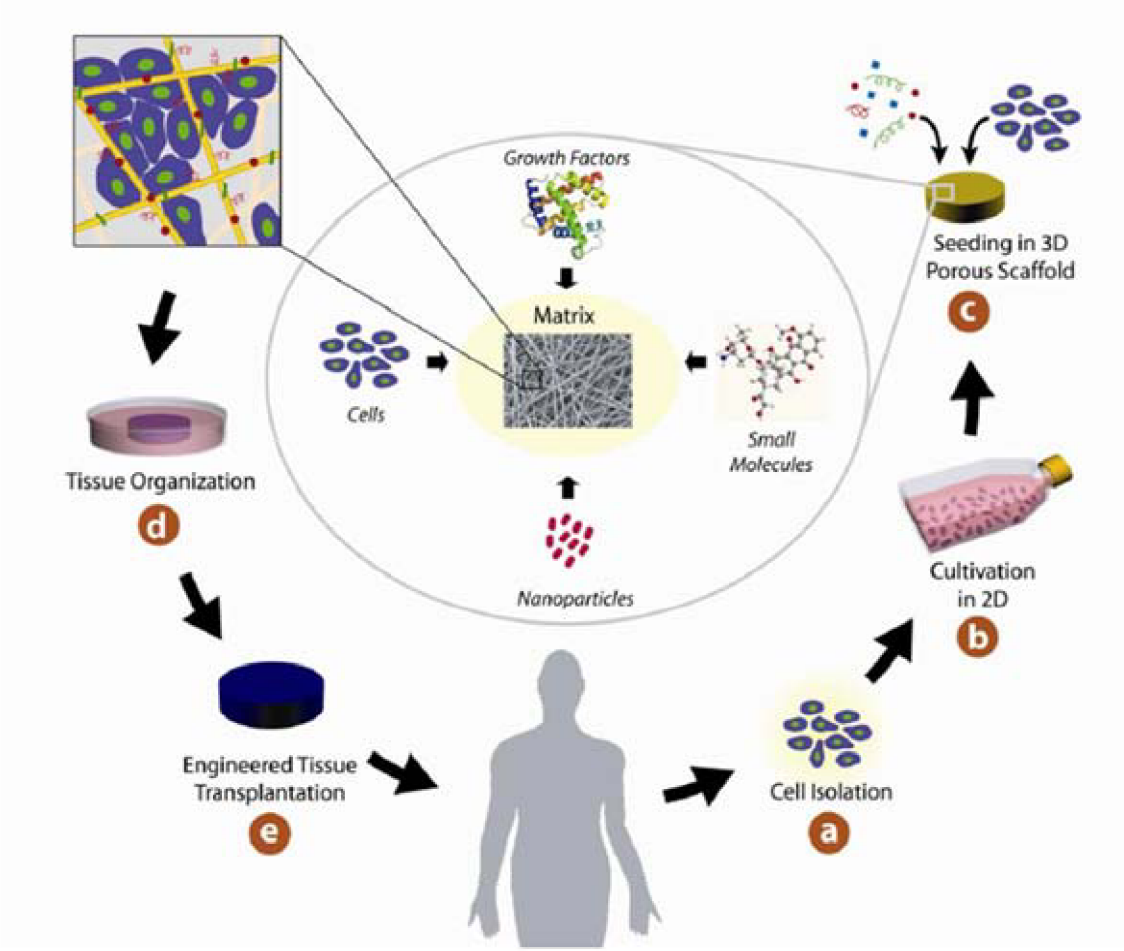

Fig. 1. Bioactive glass scaffold as a three-dimensional support for cells proliferation and regeneration [16].

In Fig. 1 is shown a schematic overview of the steps involved in the tissue engineering process *in-vivo*. After cells are withdrawn from the patient and could be cultivated, they can be seeded into the scaffolds with addition of targeted drugs, grow factors, nanoparticles or metallic ions in order to trigger specific reaction of cells [16].

2.1.1. Bioglass® 45S5

In 1969, Hench and co-workers discovered that certain silica based glasses can chemically bond to bone. It was later elucidated that this process is the result of a sequence of reactions involving ionic exchange for the glass surface wetted by biological fluids which lead to the formation of a hydroxycarbonate apatite (HCA) layer. More specifically, the processes on the glass surface are characterized by ion leaching/exchange, dissolution of the glass network and precipitation and growth of a calcium-deficient HCA layer, whereas cellular reactions include colonization, proliferation and differentiation of relevant bone cells [17]. This process has been termed as "bioactivity" and its stages are summarized in Tab. 1 [18]. The development of such a bioactive apatite layer is the common characteristic of all known inorganic materials used for bone replacement, orthopaedic implants and bone tissue engineering scaffolds. Further studies led to the establishment of a silica-based bioactive glass as having the following composition: 45 wt % SiO_2,

24.5 wt % Na_2O, 24.5 wt % CaO and 6 wt % P_2O_5. Its atomic structure can be visualized as a collection of silica tetrahedra connected by –Si–O–Si– bridging oxygen bonds. This composition was patented under the denomination of 45S5 Bioglass® or Bioglass®. Since this breakthrough discovery, many other bioactive glass compositions were developed and tested. Nevertheless, Bioglass® is still considered one of the most promising materials for bone tissue engineering [19]. Further studies have shown encouraging results regarding potential angiogenic effects of Bioglass®, i.e. increased secretion of vascular endothelial growth factor (VEGF) and VEGF gene expression *in vitro*, as well as enhancement of vascularization *in vivo* [20]. Beside the HCA–formation capability, recent studies have proven that Ca^{2+} and Si^{4+} ions release during dissolution can trigger the gene expression in osteogenitor cells giving rise to enhanced bone regeneration (intracellular effects) [21]. In addition, the incorporation of particular ions into the silicate network, such as silver [22], copper [23] strontium [24] and boron [25], has been investigated in order to develop antibacterial and antimicrobial materials.

N°	***Process***
1 & 2	Initiation and formation of SiOH bonds on the surface of Bioglass®
3	Polycondensation of SiOH+SiOH → Si-O-Si
4	Adsorption of amorphous Ca^{2+} + PO^4 + CO_3^{2-} + OH^-
5	Crystallization of hydroxycarbonate apatite (HCA)
6	Adsorption of biological moieties in HCA layer
7	Action of macrophages
8	Attachment of stem cells
9	Differentiation of stem cells
10	Generation of matrix
11	Crystallization of matrix

Tab. 1. Sequence of interfacial reactions occurring on Bioglass® surface in vivo [18].

By varying the CaO content, the bioactive behaviour can be changed by [26]. In fact, CaO modifies the network connectivity and textural properties. Many compositions containing SiO_2, CaO and P_2O_5 are found to be biologically active, and at first it was concluded that PO_5 was required for a glass to be bioactive. Nevertheless, a number of investigations have shown that two component SiO_2-CaO glasses with a maximum SiO_2 content of 65 mol% also possess in vitro and in vivo bioactivity [27]. Therefore, the key to bioactivity is not the phosphorus in the glass structure, but rather the surface reaction. A hydrated silica gel layer, which contains Si–OH groups, is believed to play a key role in apatite nucleation. However, many glasses that are able to form this layer are still not bioactive. The chemical composition, structure, and textural properties (pore's size, volume and structure) of a scaffold influence the appearance and growth of the hydroxyapatite layer. Certainly, the surface chemistry plays the main role in the bioactive layer, which controls the adsorption of phosphate salts and modifies the chemical state of the adsorbed phosphate ions.

Fabrication techniques for BGs include both traditional melt-quenching and sol-gel techniques [28-29]. The melt-quenching process, oxides are melted together at high temperatures (above 1300°C) in a platinum crucible and quenched in a graphite mold or in water (frit). The scaffolds produced in this work are obtained from melt-derived glassed therefore details about sol-gel process will be not reviewed here.
Bioglass®–based scaffolds produced by foam replication can be classified as open-cell reticulated brittle foams according to their three-dimensional morphology. What has been clearly assessed is that four factors mainly influence the mechanical response of ceramic foams [30]:

1. The topology (connectivity) and shape of the cells.
2. The properties of the solid of which the foam is made.
3. The relative density ρ_f/ρ_s of the foam, where ρ_f is the density of the foam and ρ_s that of the solid of which it is made.
4. The amount and type of defects depending on process used.

2.1.2. Sintering of 45S5 Bioglass®

One of the requisites for optimizing the fabrication of Bioglass® scaffolds is the understanding the phase transformations and thermodynamics and kinetics processes which occur during the sintering. Several studies have been conducted with the aim of investigate this aspects. In this way, the heating treatment can be tailored in order to achieve the highest density either of a bulk Bioglass® piece or of the struts constituting porous open-cell foams. Sintering of glass particles occurs by viscous flow and this process is hindered as crystallization starts [31]. During heating of Bioglass® particles at constant rate, five structural transformations and three main steps of densification were detected by differential thermal analysis (DTA) [32–34]. The first densification step occurs between 550 and 620°C , in correspondence of the first glass transition (T_{g1}). Around 570°C , a glass-in-glass transition takes places (T_s). Between 620 and 675°C , minor second step of densification is observed. This domain corresponds to the crystallization of the $Na_2CaSi_2O_6$ from the silica-rich phase (T_{c1}) [33]. The sintering process stops at 850°C . At this temperature, a third step of shrinkage begins, due to the second glass transition (T_{g2}) and at 1000°C a density of 85% is obtained. At 1100°C , the maximum density is achieved. By increasing further the temperature up to 1200°C, melting occurs. The crystallization temperatures detected by DTA are schematized in Fig. 2a. By reviewing the existing literature about phase transformations of Bioglass® upon heat treatment, consistent results have been found by different authors and they are summarized in Tab. 2. The glass transitions, crystallization and melting temperatures can be determined directly from DTA plots. DTA plot of Bioglass is shown in Fig. 2b [33]. Crystallization kinetics can be studied by DTA by using a non-isothermal method. The activation energy for crystallization (E_{cr}) was calculated by Kissinger equation [35]:

$$ln\left(\frac{\alpha}{T_p^2}\right) = -\frac{E_{cr}}{RT_p} + constant, \quad (1)$$

where α = heating rate (K/min); T_p = peak crystallization temperature; R = gas constant (8.32 J $K^{-1}mol^{-1}$). By plotting [-ln(α/T_p)] versus 1/T_p the activation energy can be calculated from the slope of the curve. A typical DTA plot for Bioglass® 45S5 is shown in Fig. 2b. When crystallization starts, sintering by viscous flow is inhibited and a fully or partially crystallized body is obtained. In the early 1940s, Avrami formulated an equation which describes the changes in volume of crystals as function of time at given temperature [36]:

$$f = 1 - exp(-kt^n), \tag{2}$$

where f is the crystalline volume fraction transformed isothermally after time t, k is the rate constant and n is the Avrami exponent. The mechanism of nucleation and growth of crystals can be defined by the Avrami parameter, n, which can be determined by the Augis-Bennet equation [37]:

$$n = \frac{2.5RT_p^2}{\Delta T \cdot E}. \tag{3}$$

Additionally, the sintering process of powder compacts can be monitored by hot–stage microscopy (HSM). By this technique it is possible to identify the sintering variables by measuring the variation of the sample dimensions during the heating process. The sample is monitored by a video camera and images of the specimen silhouette are acquired after given stretch time. Not only qualitative observations but also quantitative studies of sintering kinetics can be undertaken with this technique. The isotropic shrinkage pursuant to densification, S_I, can be calculated using the following equation:

$$S_I(\%) = \frac{A_0 - A_T}{A_0} 100, \tag{4}$$

where A_0 = the initial area of compact at room temperature; A_T = the area of compact at temperature T. Images are taken at fixed time intervals. Together with DTA, HSM can be a useful and complementary tool for studying the crystallization process of a glass.

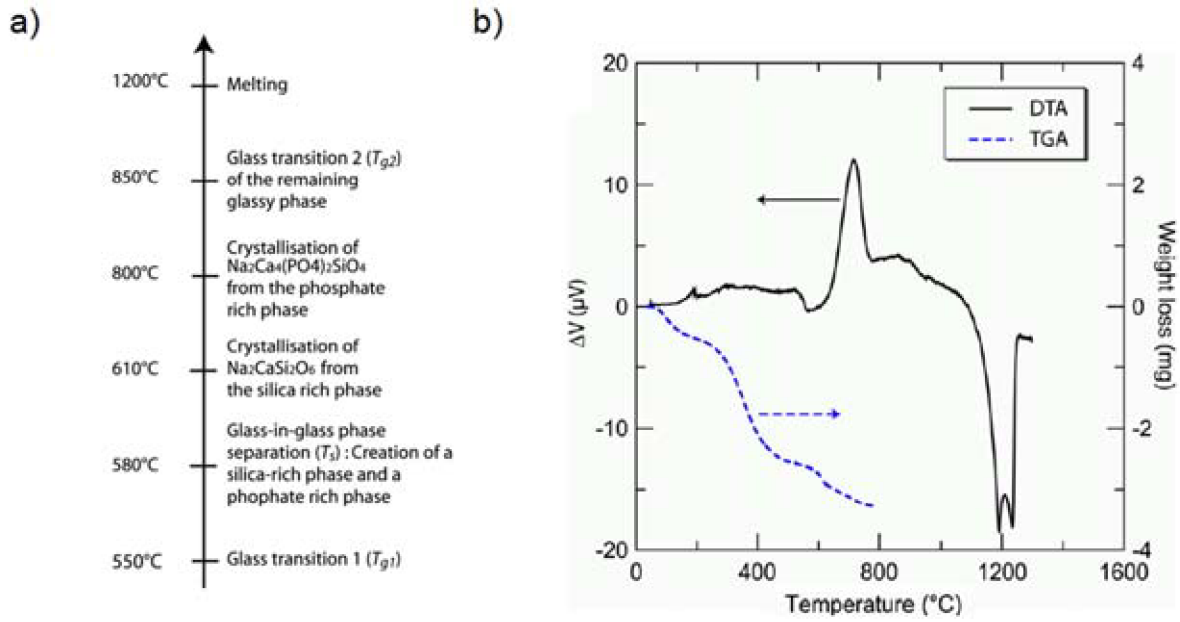

Fig. 2. TGA-DTA plot of 45S5 Bioglass®[33], summary of Bioglass® structural transformation identified by Lefebvre et at. [31].

Part. Size (μm)	H. r (C°/min)	T_{g1} (C°)	T_{c1} (C°)	T_{c2} (C°)	T_{g2} (C°)	T_m (C°)	Ref.
~1	5	550	610	800	850	1200	[1]
5	20	546	667	-	-	-	[2]
32	20	553	691	-	-	-	[2]
< 5	5-30	500-550	600-750	-	-	1180	[32]

Tab. 2. Literature overview on the influence of particle size and heating rate on the Bioglass® transformation temperatures.

Lefebvre et al. [33] reported a significant increase in the first step of shrinkage due to viscous flow with increasing heating rate. This can be properly seen in the inset of the Fig. 3a, which was obtained for a larger set of data [31]. Despite the high variability of the results, a tendency towards an increase in the first linear shrinkage is observed when the heating rate increases. This phenomenon was quantified in terms of shrinkage of a compact of powder and the variation of gap between T_{g1} and T_s with different heating rates (Fig. 3b).

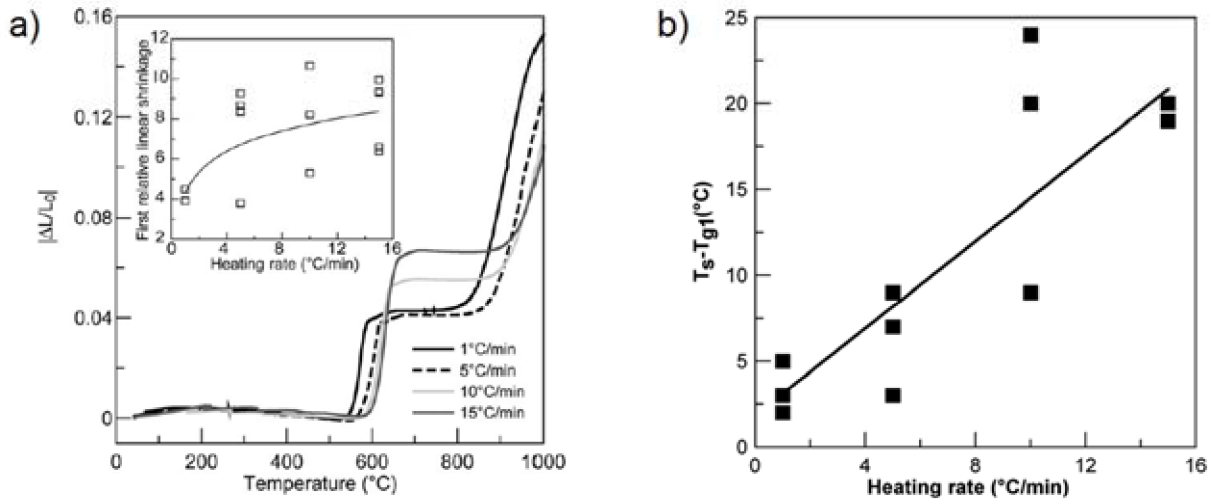

Fig. 3a) Influence of heating rate on the shrinkage of the powders compact and b) on the gap T_{g1} - T_s [31].

Thus, a faster heating rate leads to a larger temperature range where the viscous flow is not influenced by the structural transformation of Bioglass®.

Another parameter which affects the crystallization extent is the holding time at sintering temperature. Kashyap et al. [38] monitored the increase of crystalline phase of Bioglass® by DTA, differential scanning calorimetry (DSC) and by measuring the increase of crystalline area fraction from optical micrographs (Fig. 4a) of sample crystallized at 680°C for 15, 22.5, 30, 37.5, 45 and 60 min respectively [38]. The amount of crystalline phase vs. time was then plotted and a trend line based on Avrami equation, having parameters $k = 5 \cdot 10^{-5}$ and $n = 2.90$, accurately fitted the experimental data (Fig. 4b). The value of Avrami exponent n ~ 3 suggests bulk crystallization comprising three dimensional growth of crystals which were uniformly nucleated. Nevertheless, Bretcanu et al found Avrami values of 0.95 ± 0.10 which indicates the occurring of surface crystallization [32]. This discrepancy could be ascribed to the different type of sintered bodies (< 5 µm powder, vs cast rods). Bellucci et al. [39] reported that the calculated value for the Avrami constant is affected by the particle size of the powder. In fact, it is known that small particles may undergo surface crystallization also in systems with bulk crystallization [40].

Chatzistavrou et al. studied the influence of particle size of the starting powder on the transformation temperatures and crystallization mechanism [41]. The height of the first DSC peak (at low temperature) was decreased with increasing particle size, thus indicating that the mechanism of surface crystallization could be associ- ated with this peak. The height of the second DSC crystallization peak (at high temperature) remained un- changed with increasing particle size indicating a volume crystallization mechanism.

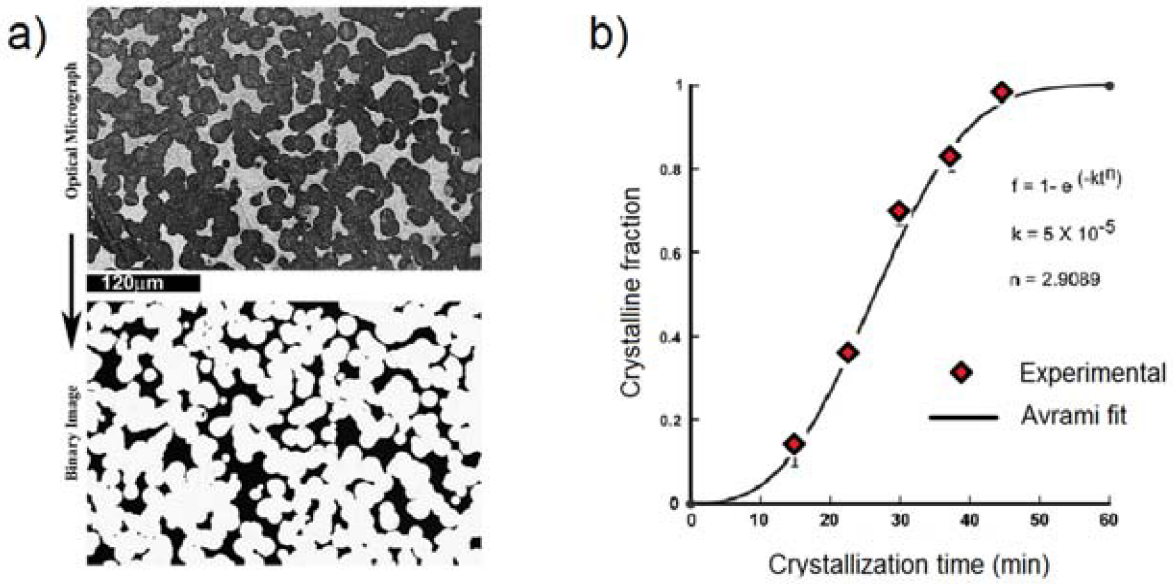

Fig. 4a) Optical micrograph (680°C at 30 min) binarized for crystalline area measurement; b) measured crystalline fractions at different times fitted by Avrami equation [38].

2.1.3. Fabrication of scaffolds by foam-replication process

Foam-replication is a simple technique which enables the production of open cell ceramic foam with controlled macroporosity [42]. The process consists of dipping an open–cell polymeric foam into a ceramic slurry. Slurries are colloidal suspensions of fine ceramic/glass powder in a liquid phase with small amounts of secondary materials such as dispersants, surfactants and binder. The solid content in the slurry typically lies in the range 30 - 70 wt% and should be tailored in order to obtain the desired viscosity [43]. After dipping, samples are squeezed in order to remove the excessive slurry and the resulting green body is subsequently dried. The burning of template and sintering can be carried out in a single step. The most used templates for this application are reticulated poly-urethane (PU) foams. This choice is due to several reasons. PU foams completely recover their shape after squeezing and above 400°C , they burn completely without leaving any residual combustion product. PU foams are commercially available and can be purchased at low price having different pores size (expressed in pores per linear inch, PPI). These foams are produced by direct foaming method. During this process a supersaturated gas is made to separate from a liquid. Gas bubbles nucleate and grow as spheres until they get into contact [44]. The heating rate and kept as slow as possible in order to prevent formation of residual stresses or cracking of the ceramic network due to volatilization of burning residual. The final result is a ceramic foam distinguished by a reticulated structure (>85% of total porosity) and hollow struts resulting from the burning out of the polymer foam substrate. High solid fraction leads to an excessive viscosity and difficulties to eliminate the slurry in excess might arise. Lower mechanical properties and large defect population are therefore a typical characteristic of this route. Dipping can be repeated several times in order to achieve the desired coating thickness, which will in turn determine the cross–sectional area of the struts in the sintered foam.

In 2006, Chen et al. [45] fabricated for the first time a three-dimensional, highly porous Bioglass®-based scaffold by foam replication process, using melt-derived 45S5 Bioglass® powder. The steps

involved in replica process and the thermal profile they used for sintering are summarized in Fig. 5. Nearly full densification of the struts occurred and fine crystals of $Na_2Ca_2Si_3O_9$ (Combeite) were detected. A primary disadvantage of bioactive glasses is their low fracture toughness, because of their amorphous structure.

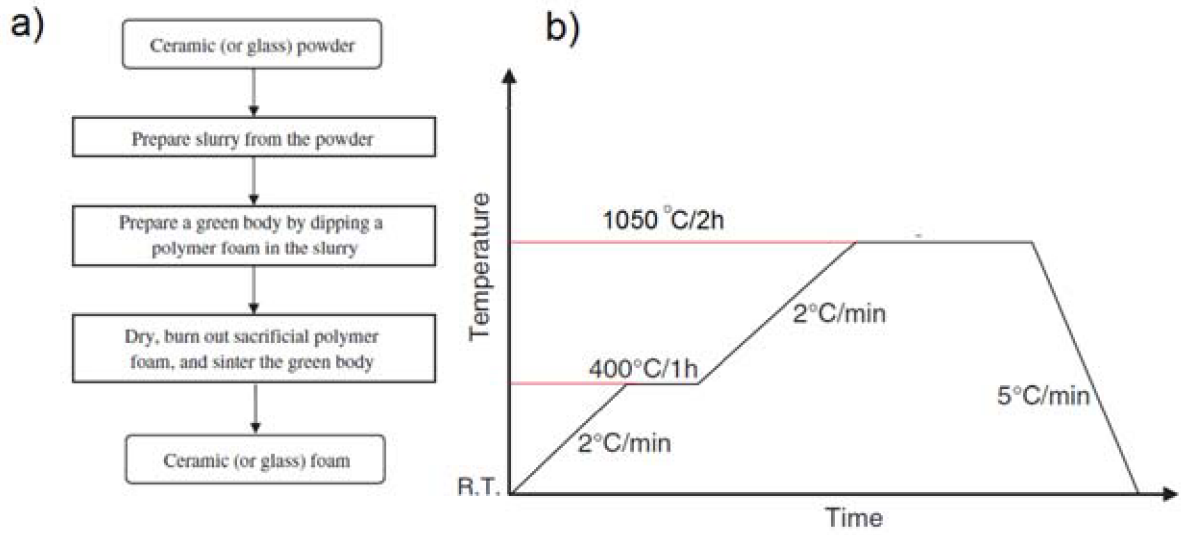

Fig. 5a) Flow chart of the foam replication process used to the production of Bioglass®-based scaffolds and b) conventional heat treatment program designed for the sintering of 45S5 Bioglass® scaffolds [45].

Bioglass® scaffolds can be also produced by using different methods such as starch consolidation [46], foaming method [47], and gel-casting [48, 49]. Techniques based on starch have gained a prominent position, because they are cheap, non-toxic, environmentally friendly and exhibit defect–free burnout between approximately 300 and 600°C [50]. Starch such as, food grade fine rice flour is mixed with gelling agents and ceramic powder into distilled water. The mixtures are then stirred, and cast. After coagulation, they are subsequently dried and sintered. The direct foaming method begins with ceramic slurry which is foamed, polymerized, removed from the mold (demolding) and finally dried and sintering. This technique allows the production highly porous green bodies that are comparatively strong and can easily withstand machining [51]. Gel-casting has been established for simplicity and ability to produce a high degree of homogeneity as well as green body strength, and therefore good machinability. The fabrication process begins with mixing of a colloidal ceramic suspension containing water soluble monomers and a foaming agent. After foam formation, the suspension rapidly gels by means of the polymerization of the monomers gaining stiffness and mechanical stability. Also in this case, the green body is then dried and sintered and the resulting ceramic foam exhibits nearly spherical pores and highly dense struts [52]. Concerning foam–replication process, the main disadvantage is associated with the hollow struts and large amount of flaws that results from burning out the polymer foam substrate [42].

2.2. Macrostructure and microstructure of porous ceramic scaffolds

In the case of Bioglass® scaffolds obtained by replica method, the template structure (i. e., struts connectivity and cell size) is critical in determining the properties of the final component. In order

to have insights about a glass-ceramic scaffold produced by replica process is useful to first consider the macrostructure of precursor polymeric template from which the scaffold is derived. It has been assessed that open-cell PU foams used in replication techniques can be modelled by a tetrakaidecahedrical cell unit, packed in a BCC structure [53]. This kind of structure satisfies the minimum surface energy–condition for mono-dispersed bubbles which occur during foaming process. Maxwell's stability criterion states that open- or closed-cell, might be either stretching- or bending-dominated according to the number of struts which constitute the cells and their connectivity [54]. Such criterion defines a value M for a 3D structure made up of b struts and j frictionless joints as:

$$M = b - 3j + 6 . \tag{5}$$

If M <0, the frame is a mechanism and has one or more degrees of freedom, along some directions displacements are allowed and stiffness and strength drop. If instead M = 0 the frame ceases to be a mechanism and the structure is both statically and kinematically determinate. As it is loaded, its members carry tension or compression (even when pin-jointed), and it becomes a stretch-dominated structure. As M > 0 the structure undergoes a state of so-called self-stress, which means that struts carry stress even though no external loads are applied on the structure.

Hence, Maxwell's criterion enlightens a key point behind the weakness of PU–derived Bioglass® foams: their structure is mainly bending-dominated. In fact no single space-filling polyhedral cell, including tetrakaidecahedron has M ≥ 0. The structural efficiency of stretch-dominated structures is higher than the one of bending-dominated structures (at the same relative density). In order to give an example: a low-connectivity lattice with a relative density of 0.1 is 10 times less stiff than a stretch-dominated triangulated lattice of the same relative density. Several models have been developed to correlate the mechanical properties of open cell ceramics foams (Young's modulus, Poisson's ratio, fracture toughness, tensile strength and compressive strength) of ceramic foams to their topology and micro-structural features [30, 55–58]. Generally, these models can be categorized into two types. The first type is based on repetitive unit cell models which provide the homogenized behaviour of foams, including two dimensional foam/honeycomb models and three-dimensional cubic, tetrahedral, and tetrakaidecahedral. Based on the developed unit cell models, the mechanical properties of foams (e.g., the Young's modulus, bulk modulus, multi-axial failure surface, etc.) are evaluated. Although unit cell models have been proven to be useful in understanding some important features of real foams, several drawbacks exist. It is found that they usually over-predict the bulk modulus and hydrostatic yield strength of real foams. The second type has been developed in order to give a better representation of the morphological structure of real foams, by taking into account defects and irregularities. As an example, Voronoi models [56, 59, 60, 62] or the X-rays and computed tomography in conjunction with the finite element method (FEM) have been reported [61–64].

Computed tomography (CT) is an imaging method which allows the three-dimensional reconstruction of an object from the stacking of a large series of two dimensional X-ray projections, taken while it is rotating around a single axis. X-ray images are obtained by an X-ray source which first goes through the object to be scanned and then is collected by a detector. The scanning of a material is based on variations of X-ray absorption. Hundreds of radiographs of a sample are taken at small angular increments over 180 degrees of the sample rotation. A computer algorithm inverts

this data to produce a 3D absorption map. Micro-computed tomography (μ-CT) has been already used as a standard technique for the visualization and quantification of the 3D structure of trabecular bone [61, 62]. μ-CT generated 3D images were used to determine foam's parameters such as porosity, cell sizes and polyhedra types, ligament length and connectivity, material distributions along the ligaments and prevalent geometric anisotropies. The basic configuration of a X-ray photography is shown in Fig. 6. This technology is particularly suitable for the morphological analysis of foams, because the large difference in density between the two phases comprising the volume of the component (i.e. the solid skeleton and the air) leads to high contrast and well-defined phase boundaries [62]. Beside the morphologic characterization, μ-CT allows to use the reconstructed structure as input for the finite element modelling (FEM) [63].

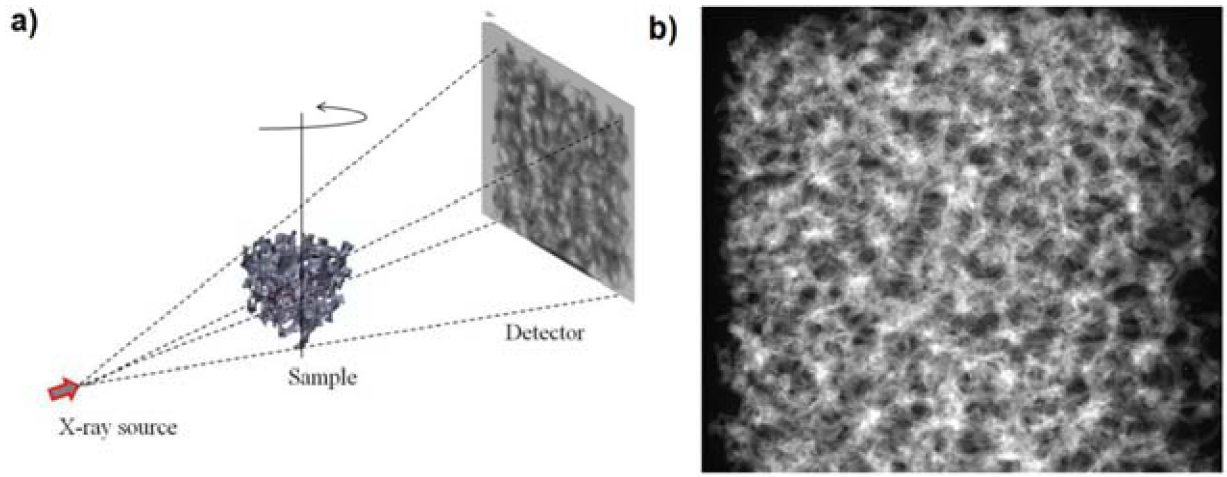

Fig. 6. Basic schematic displaying X-ray photography of foams.

PU templates which are used for the production of Bioglass® scaffolds are obtained by direct foaming technique and exhibit anisotropy since the volume expansion caused by gases cause the foam to rise in one direction. The derived ceramic foam therefore exhibits anisotropy as well. According to D'Angelo et al., [68] anyhow, the randomness of struts distribution in space limits the anisotropy due to the cell elongation. Replica foams can be thus considered orthotropic with a transversal isotropic behaviour. Recent works reported μ-CT results, showed that the foam possessed an average connectivity of 4 thus confirming that a tetrakaidecahedron structure can appropriately represent the foam cell [65].

2.3. Mechanical properties of Bioglass®

By reviewing the huge amount of papers dealing with Bioglass® scaffolds, it is possible to notice how mechanical properties are remarkably scattered, depending on the sintering route used. Properties of sintered Bioglass® can in be widely scattered, depending on the amount of crystalline phase in the amorphous matrix, which can be in turn controlled by tailoring the thermal treatment used for sintering. It is in fact well known that glasses can be strengthened by the formation of crystalline domains in the glass matrix upon heat treatment [67, 68]. Glass-ceramics with crystalline volume fraction between 34 and 60% exhibited improvement of three times in fracture strength and an increase of 40% in indentation fracture toughness compared with the parent glass.

In numerous papers dealing with dense and porous 45S5 Bioglass®, the effect of crystalline volume fraction (at constant crystal size) and crystal size (at constant crystallized volume fraction) was investigated [38, 44, 69–71]. These results demonstrated that it is possible to design bioactive glass-ceramics with improved microstructures by finely tuning the sintering process.
Young's modulus of 45S5 Bioglass® was reported ranging from 30 to 35 GPa [74], being much lower elastic modulus than A/W glass-ceramic and similar to that of cortical bone. The flexural strength was significantly higher than that of cortical bone and comparable to that of apatite–wollastonite (A/W) composites [75]. The bending strength of most bioactive glasses falls in the range of 40 – 100 MPa, which is not sufficient for load-bearing application. Since that, Bioglass® implants can be used in non-load-bearing applications, for buried implants loaded slightly or compressively.
Some values related to mechanical properties are reported in Tab. 3. According to Peitl et al. [76], the introduction of crystallinity in this bioactive glass significantly increased the fracture strength from 80 to 210 MPa and the indentation toughness from 0.60 to 0.95 MPa·m$^{1/2}$, while the Young modulus underwent only a small increase from 60 to 70 GPa. These overall improvements in mechanical properties were attributed to crack deflection mechanisms within the material. Another factor which influences the mechanical properties of sintered Bioglass® are residual stresses. Residual stress exists in the bulk of a material, and might arise pursuant to heterogeneous plastic deformation, thermal contraction or phase transformation.

Material property	*Trabecular bone*	*Cortical bone*	*Bioglass® (bulk)*
Compressive strength [MPa]	0.1 – 16 [77, 78]	130 – 200 [77, 79]	500 [79]
Tensile strength [MPa]	n. a.	50 – 151 [79]	42 [74]
Compressive modulus [GPa]	0.12 – 1.1 [80, 81]	11.5 – 17 [82]	n. a.
Young's modulus [GPa]	0.05 – 0.5 [74, 79]	7 – 30 [74, 79]	35 [74]
Fracture toughness [MPa·m$^{1/2}$]	n. a.	2 – 12 [73, 79]	0.7 – 1.1[36]

Tab. 3. Bioglass® mechanical properties summarized by Gerhardt et al. [29].

The linear elastic fracture mechanics (LEFM) which is used to describe the majority of fracture events in glass and glass–ceramics is based either on energy calculations or stress intensity calculations. The latter deals with the stresses and strains taking place at the crack tip and it is therefore suitable in engineering purposes, as the material deformation is described in terms of stresses and strains. The description of the stress intensity factor for dense, homogeneous, isotropic solids which exhibit linear elastic behaviour can readily be described by the well-known relationship [83]:

$$K_I = \sigma_A Y \sqrt{C}, \tag{6}$$

where K_I is the stress intensity factor for opening mode I, σ_a is the stress applied to the material at some distance remote from the crack tip, Y is a dimensionless parameter which depends upon the geometry of the loading and crack configuration and C is the characteristic dimension of the flaw. In loading a material, once K reaches a critical value denoted K_{IC}, unstable crack growth occurs. K_I is typically considered to be an intrinsic material property which may be used to characterize the material's mechanical integrity. Using the theory of elasticity, it is possible to calculate the stress field in the proximity of a crack in an arbitrary body with an arbitrary crack undergoing arbitrary loading. Using the coordinates system shown in Fig. 7, the stresses for mode I are:

$$\sigma_{ij} = \frac{K_I}{\sqrt{2\pi r}} f_{ij} + C_1 r^0 + C_2 r^{1/2} + \cdots \tag{7}$$

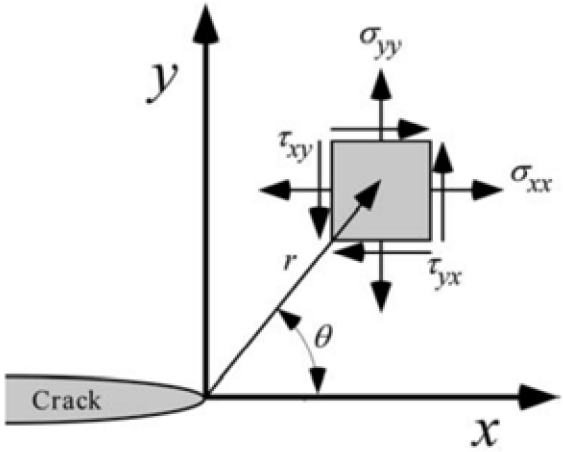

Fig. 7. Stresses near the crack tip in an elastic material [83].

If r→0 the first terms very large and other terms can be neglected, and for θ = 0, f(θ) = 1, so that:

$$\sigma_{yy} = \frac{K_I}{\sqrt{2\pi r}}, \tag{8}$$

where r is the distance from the crack tip along the x-axis. The fracture toughness, K_{IC}, is the critical value of the stress intensity factor at a crack tip needed to produce unstable catastrophic failure under general triaxial loading.

A phenomenon which has to be considered when testing the mechanical properties of glass materials is the subcritical crack growth [84]. It is generally accepted that water or other chemical agents attacks the region around the crack tips or surface flaws, weakening the structure in the vicinity of the crack tip. This allows cracks to grow at stress intensities below the critical value (K_{IC}). Stress corrosion cracking phenomenon is quite complex due to local chemical reactions that occur and to diffusion mechanisms. The fracture process itself may activate the surface for reactions with water vapor. In previous works, the hydration of the surface of a highly bioactive silicate glass was modeled using ab initio molecular dynamics (CPMD) simulations, focusing on the structural and chemical modifications taking place at the glass–water interface. The initial enrichment of the

surface region in Na^+ cations establishes dominant Na^+–water interactions at the surface, which allow water molecules to penetrate into the open glass network and start its partial dissolution [85].

2.3.1. Indentation fracture toughness

Brittle materials may form three different types of cracks when indented with a Vicker's indenter [86]: 1) Palmqvist cracks (cracks emanate from each of the corners of the indent but do not pass underneath the indent); 2) half penny cracks, which are radial median cracks: similar to Palmqvist cracks but emanating from under the center of the indent from one indent corner to another on the same diagonal — usually formed at higher loads than Palmqvist cracks; and (3) lateral cracks (cracks that form on the sides of the indent and intersect the surface between the corner cracks). Depending on the load, 45S5 Bioglass® was observed to display halfpenny and lateral cracks, although, from a plan view, it was very difficult to distinguish Palmqvist from halfpenny cracks. K_{IC} can be determined from the cracks propagating from the edges of a Vickers indentation under certain indentation loads [71]. The main principle behind this approach concerns the crack shape. Cracks are assumed to be radial-median cracks beneath the indent, with a center point force leading to crack opening [71]. Satisfying these conditions leads to a specific stable equilibrium relation between the applied load, P, and the crack size c. In Fig 8a it is possible to observe a Vickers indent on a polished Bioglass® surface with Palmqvist crack departing from indent corner [72]. In Fig. 8b is shown a typical P–δ curve indicating the areas associated with the elastic energy, E_E, and anelastic energy, E_A (consumed and stored energy in the material), with the total energy, E_T, being the sum of the two regions ($E_T = E_E + E_A$).

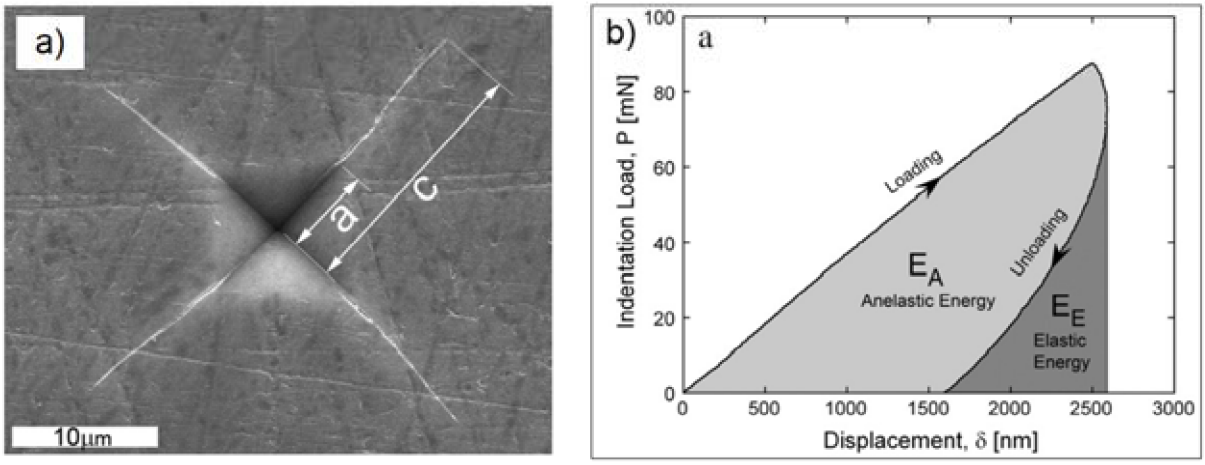

Fig. 8a) SEM image of a Vickers indent on polished Bioglass surface: a and c indicate the half indent diagonal and half crack length respectively [38]; b) Total (E_T), elastc (E_E) and anelastic (E_A) energy in a typical load-displacement plot [71].

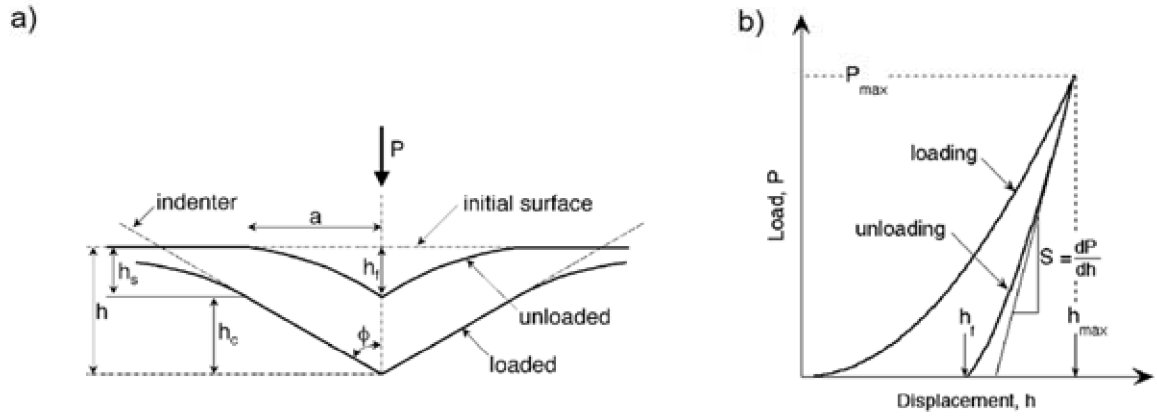

Fig. 9. Schematic illustration of the unloading process showing parameters characterizing the contact geometry; b) typical of indentation load–displacement curve with related parameters [87].

In Fig. 9a, the indent profile of a Vickers indent, with related load parameters are shown: the maximum indentation depth = h, the indenter displacement at peak load = h_c and the final depth of the contact after unloading = h_f. In Fig. 9b is shown a typical load-displacement curve obtained from indentation test. The elastic contact stiffness (S) can be obtained by fitting the unloading curve and taking the tangent at the peak load (P_{max}) as the slope of the upper portion of the unloading curve, S = dP/dh (Fig. 9b). Using Sneddon's solution and the result given by Oliver and Pharr [88], the contact depth h_c can be calculated as [89]:

$$h_c = h - \varepsilon \frac{P_{max}}{S}, \tag{9}$$

where ε is a function of the particular tip geometry (for a perfect Vickers indenter, ε = 0.75. In many brittle materials, the slope of the anelastic (plastic) energy is a constant over various indentation loads.

2.3.2. Measurement by of fracture toughness by Chevron-notched beams

The chevron notched (CN) specimen technique is a well-established standardized method used to determine the fracture toughness of different brittle materials, including monolithic glass, glass-ceramics and ceramic matrix composites [90]. In chevron notches, the crack front increases in width from zero to the full thickness of the specimen as the crack length increases in the notch plane. It is assumed that stable crack growth occurs from the apex of the chevron during loading. There is, therefore, no need to pre-crack the specimen, which is a time consuming and tedious task; this is a further advantage of the CN geometry. A scheme showing the specimen loading geometry and notch position in a Chevron–notched beam is shown in Fig 10a. SEM micrograph of a Chevron notch and fracture surface after testing is shown in Fig. 10b [90].

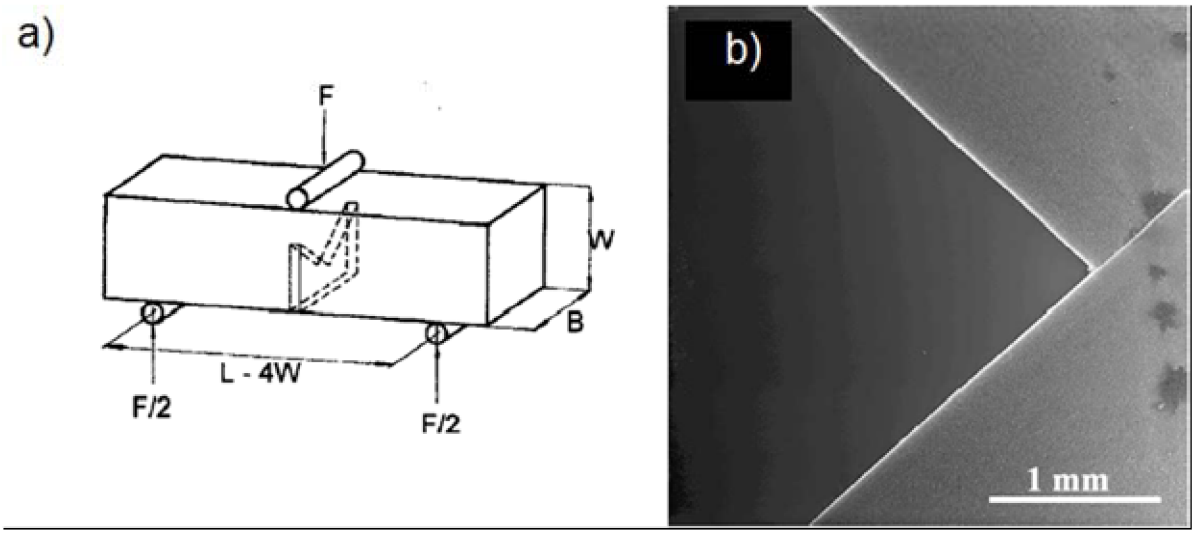

Fig. 10. Schematic diagram showing the specimen loading geometry and notch position in a Chevron–notched beam; b) SEM micrograph of a Chevron notch and fracture surface after testing [90].

2.3.3. Mechanical properties of Bioglass®–based scaffolds

A micromechanical model often used to predict properties such as elastic modulus and crushing strength of porous Bioglass® scaffolds is the Gibson-Ashby (GA) model [30]. This was the result of the research endeavors of Gibson [91] and Green [92] and it is based on the simplification of a given body structure to a more uniform and idealized one. GA model idealizes them as sequence of cubic cells, whose repetitive unit is shown in Fig. 11b. The struts are in this case idealized as rigid defect-free beams, having theoretical density. In the linear elastic regime, under uniaxial stress, open-cell foams deform primarily by bending of the cell edges. It has been assayed that the compressive response of Bioglass®-based foams is characterized by linear elasticity at low stresses followed by an extended collapse plateau and a period of densification in which the stiffness increases sharply. As a force F is acting on the cell as shown in Fig. 11b, the Young's modulus of the foam and its brittle collapse stress σ^*_{cr} is given by [93]:

$$E^* = E_s C_1 \left(\frac{\rho_f}{\rho_s}\right)^2, \tag{10}$$

$$\sigma^*_{cr} = \sigma_{fs} C_2 \left(\frac{\rho_f}{\rho_s}\right)^{3/2}, \tag{11}$$

where E_s is the Young's modulus of the solid and σ_{fs} is the modulus of rupture of the strut material. C_1 and C_2 are geometrical constants of proportionality. By fitting the experimental data, were found to be 0.3 and 0.65, respectively [90, 91]. Nevertheless, due to the reduced magnitude of displacements in the elastic region, acquired data are not always reliable.

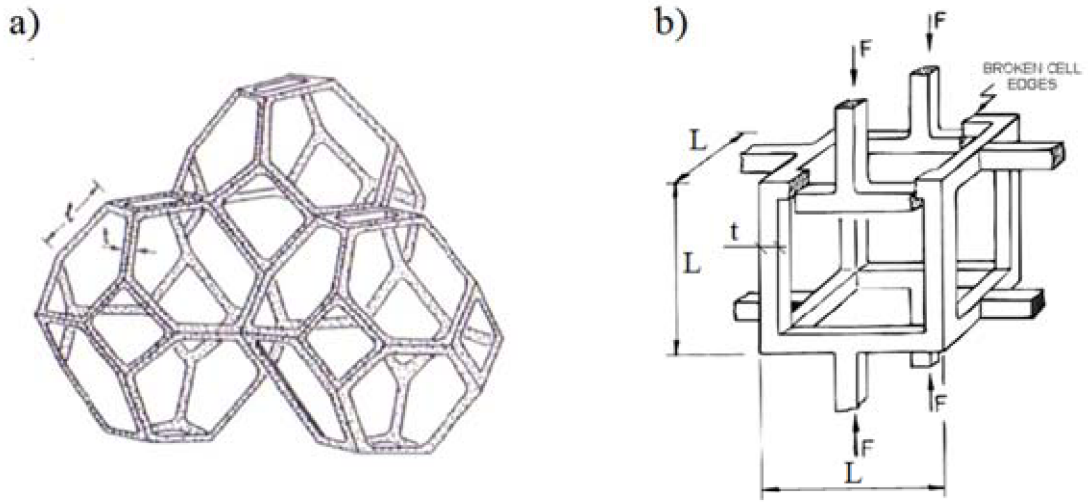

Fig. 11 a) Kelvin tetrakaidecahedrical unit cell [95]; b) and cubic Gibson-Ashby open–cell model [30].

For foams made by hollow struts, Eq. 11 can be rewritten as:

$$\frac{\sigma^*_{cr}}{\sigma_{fs}} = 0.2 \cdot \left(\frac{\rho_f}{\rho_s}\right)^{3/2} \frac{1+(t_v/t_s)^2}{\sqrt{1-(t_v/t_s)^2}}, \tag{12}$$

where t_v/t_s is the ratio of the void and strut sizes on a cross section of a strut. According to GA model the unit cell is represented as a cubic array of struts having square cross-section t and length L. Even though this represents an idealized structure far from the reality, it emphasize the bending of struts under axial loads. For a low density material ($\rho/\rho_s < 0.1$) it has been found to be $\rho/\rho_s \sim (t/L)^2$. Hence, a strut will fail when the bending moment acting on it exceeds the fracture moment.

Equations for several other mechanical properties such as fracture toughness (normalized), tensile (flexure) strength, and hardness all again involve proportionality constants (ca. 0.65 for each of these cases), depend linearly on strut strength, and all have a porosity dependence of $(\rho/\rho_s)^{3/2}$. The brittle-crushing strength has been found assuming that the modulus of rupture of the strut is constant. In practice, it varies for brittle materials, following a Weibull distribution [19]. Because of their low fracture toughness, ceramics and glass are very sensitive to the presence of small defects and flaws (~10 μm) and they can fail catastrophically when subjected to tensile or flexural stresses far lower than their compressive strength. The strength of brittle materials is therefore a stochastic variable [96].

2.4. Reinforcement of Bioglass® scaffolds by polymer-based coating

The idea of creating composite scaffolds by combining a stiff mineral phase with a softer and tougher phase such as a polymer was inspired by observing the structure of a real bone. Bone in fact is a composite material itself, composed of carbonated apatite (65 dry wt. %) which confers structural reinforcement and collagen (35 dry wt. %) which contributes to an increase of flexibility

and toughness. The deposition of a thin polymeric coating on bioactive ceramic/glass scaffolds in order to increase their strength and crack resistance is an effective method which has been already reported by several researcher [92, 93].

By observing the stress-strain curves of polymer-coated ceramic scaffolds obtained either from compressive or tensile tests, two different contributions to toughening and strengthening can be detected. The first one can be identified as a remarkable increase of the stress value at which the first fracture event occurs in comparison with non-coated samples. This behaviour has been ascribed to a lowering of stress concentration at the defect sites on the strut surface, which allows further increase of the remote load without any failure occurring with the consequent extension of the elastic domain [29]. As the stress peak is reached, cracks initiate and propagate across the struts under the influence of a local component of applied external load, the coating film undergoes progressive deformation forming thin fibrils which are capable to bridge the cracks edges, opposing the crack opening process and preventing the catastrophic fracture of the whole structure [93, 94]. Deformation and tearing of coating fibrils and debonding of film from the scaffold are responsible for energy dissipation, causing an increase of the overall fracture energy. This phenomenon corresponds to the plateau region which is usually observable on the load displacement curves from tensile and compressive strength tests [99]. The magnitude and appearance of the plateau basically depends on the mechanical response of the coating to the applied stress (Young's modulus, tensile strength, strain to fracture, damage mode).

By reviewing the literature on this topic, it can be found that different polymers, either natural or synthetic have been used for this purpose. Among the natural ones, collagen [100], alginate [101], silk [102], gelatin [103] and chitosan [104] can be mentioned. Concerning the synthetic ones, poly(lactic acid) [105], poly(hydroxybutyrate) [98], PHBV [106], poly(ε-caprolactone) [107] were reported as well. Besides sufficient mechanical capability, coatings for bone replacement scaffolds must also fulfill other requirements such as biocompatibility, biodegradability and tunable degradation rate. The possibility of functionalization of scaffolds for controlled drug release is also a desirable goal [96, 98, 103]. Unfortunately, polymers usually exhibit low elastic modulus (below a few GPa), therefore it is desirable to develop improved biodegradable coatings having higher elastic modulus and strength. From this standpoint, the adhesion between coating and substrate plays a fundamental role since the external loads must be transferred from the struts to the coating through this interface [109]. Previous studies on dip-coated plates have, for instance, shown that the thickness of deposited liquid film coatings depends on the coating solution properties such as density, surface tension, viscosity as well as withdrawal speed from the coating solution [105, 106]. Moreover, the wettability of the polymer solution determines the adhesion of the resulting film on the interface [112]. Beside a thermodynamic driving force, the viscosity of the polymeric solution plays also a role in the infiltration capability, which should be as low as possible in order to be able to infiltrate into the cracks and defect at greater extent [110–113].

When a liquid drop is placed on a solid surface, it may start to spread to larger or lesser extent, depending on the intermolecular forces interacting between the two phases. If solid – liquid interactions are stronger than those between the liquid molecules themselves, then the liquid spreads over the solid surface, even up to its monomolecular layer if the solid surface is sufficiently large.

A contact angle less than 90° indicates that wetting of the surface is favourable, and the fluid will spread over a large area on the surface; while contact angles greater than 90° means that wetting of the surface is unfavourable so the fluid will minimize its contact with the surface and form a compact liquid droplet. As first described by Young [113], the contact angle of a liquid drop on an ideal solid surface is defined by the mechanical equilibrium of the drop under the action of three interfacial tensions.

$$\gamma^{sv} = \gamma^{sl} + \gamma^{lv} cos\theta_Y, \tag{13}$$

where γ^{lv}, γ^{sv}, and γ^{sl} represent the liquid-vapour, solid-vapour, and solid-liquid interfacial tensions, respectively, and θ_Y is the contact angle. According to Snoejier et al., the contact angle is expected to be characteristic for a given solid-liquid system in a specific environment [114]. The final mechanical properties of polymer-coated porous ceramics are also affected by other parameters related to the coating process itself such as the removal technique of the excess polymer, the concentration of the polymer solution, the atmospheric pressure, humidity, eventual heat treatment, a number of dipping and so on [9, 10].

In the case of scaffolds such approach would be further complicated by the complex, irregular architectures and by the macro and micro features which distinguish their surfaces. It is therefore convenient to simplify the problem to an idealized case. Beside a thermodynamic driving force, the viscosity of the melt or polymeric solution plays also a role in the infiltration capability, which should be as low as possible in order to be able to infiltrate into the cracks and defect at greater extent [115]. The influence of polymeric coatings on the stiffness of 45S5 Bioglass®–based scaffolds was recently investigated by the non-destructive ultrasonic technique by Li et al. [116]. The results showed that the stiffness of uncoated scaffolds was increased by applying polymer coatings, and in particular that there is a direct dependence of the resulting stiffness of the coated scaffold on the stiffness of the polymer coating. On the other hand Peroglio et al. [99] found that the presence of coating considerably increases the post–yield energy as well as the apparent fracture energy of the scaffolds and strength. Conversely to the prediction of Ashby, the correlation between tensile strength and density was found as weak (Fig. 12a). The coating in this case has no effect on the Young's modulus of the scaffold (which is visible by considering the slope of linear domains in Fig. 12b). The addition of polymer completely changes the mechanical behaviour of the scaffold and the load–deflection curves can now be decomposed in three stages: a linear elastic one in which the maximum stress is reached, a drop of the load and a plateau during which the load remains roughly constant while the deflection can reach several microns depending on the infiltration method and polymer properties (Fig. 12b).

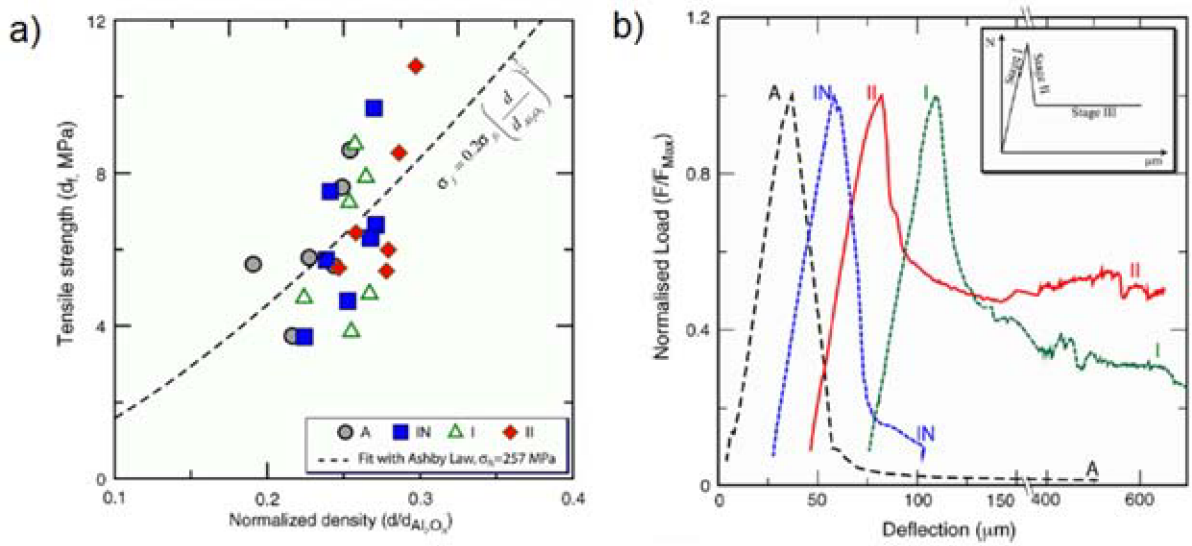

Fig. 12a) Ultimate strength (σ_f) vs. normalized density of un-coated and PDLLA-coated alumina scaffolds; b) Four-point bending load–deflection curves [99].

2.4.1. PVA

Polyvinyl alcohol (PVA) is a water-soluble biodegradable and non-toxic polymer which is gaining growing interest for biomedical applications both as a structural component, e.g. for artificial cartilage or tissue engineering scaffolds [117] or as a functional component e.g. for controlled drug delivery systems [118]. PVA is produced by the polymerization of vinyl acetate to poly(vinyl acetate) which is subsequently hydrolyzed to PVA. The biocompatibility of PVA implants was demonstrated by Tadavarthy et al. [119] in 1975 with the development of the Ivalon® embolic material. PVA gels with 80%–90% water content by weight were implanted subcutaneously or intramuscularly into rabbits, and no adverse effects were noticed in the surrounding tissue leading to a confirmation of the biocompatibility of the material [120]. PVA hydrogel cross-linked by gamma irradiation has also been shown to function as a vitreous substitute. PVA aqueous solutions can be cast and dried in order to obtain translucent film having good mechanical properties. As cast, these films are mostly amorphous, and crystallites initiate predominately in the final drying stages; crystallization proceeds thereafter slowly, aided by the ambient humidity. If the ambient humidity is too low or absent, the drying polymer becomes glassy, and crystal growth becomes arrested before extended crystallites can develop and impinge. Though PVA has a T_g above room temperature, water-cast films still form crystals at ambient temperatures due to the slow drying nature of the hydrophilic polymer. The degree of hydrolysis of PVA represents the extent to which the poly(vinyl-acetate) has been hydrolyzed to produce PVA. Commercial PVAs are basically available as fully hydrolyzed grades (degree of hydrolyzation ~ 98%) and partially hydrolyzed grades (degree of hydrolysis in range of 86 - 89%). The solubility of PVA in water depends on the degree of hydrolyzation and the degree of polymerization. Some PVA grades with higher degrees of hydrolyzation (98%) are only soluble in hot water (50–100° C) and form films that are insoluble in water at lower temperatures. In contrast, PVA grades with degrees of hydrolyzation in the range of 75–98% are easily soluble in water.

2.4.2. Microfibrillated cellulose

Cellulose is a linear, high–molecular-weight hydrophilic polysaccharide consisting of repeating poly-β(1,4)–D–glucopranose units. It naturally occurs in plant cell walls as a load-bearing component as well as in tunicate sea animals or synthesized by bacteria [121]. In the biomedical field, cellulose and its derivatives have been extensively used for decades. The biocompatibility of several cellulose–based materials is well established [122]. Ikada [123] has described cellulose as a polymer usually exhibiting relatively low protein adsorption and cell adhesion (particularly blood cells), low immune response (low phagocytosis by macrophages and low interleukin-1 release), and inducing comparatively higher activation of the complement system. Cellulose is poorly biodegradable in the body and is not digestible, but it can be made hydrolysable by changing its higher order structure [124]. For instance, Baquey et al. have pioneered and considerably contributed to this field of study by firstly proposing the use of regenerated cellulose hydrogels (RCH) for orthopedic applications. Cellulose regenerated by the viscose process (CRV®) was patented and thoroughly investigated in terms of physico–chemical, mechanical and biological properties. It was later chemically modified to enhance its bioactivity through modifications such as phosphorylation, grafting of adhesive peptides and oxidation.

Microfibrillated cellulose (MFC) consists of high aspect ratio cellulose nanofibrils obtained either by mechanical disintegration or by acid hydrolysis of the wood cell wall [125]. MFC was first prepared by Herrick et al. and Turbak et al. in 1983, by fibrillating wood pulp by means of a high-pressure homogenizer. Ankerfors et al. [126] established a new processing route, combining the mechanical treatment with chemical or enzyme-based pretreatment which lowers the strength of inter-fibrils interactions. In this way the energy consumption of the process could be decreased, opening up the possibility of large scale production and commercial exploitation. Properties such as non-toxicity, biodegradability, large surface area and remarkably high elastic modulus (~ 146 GPa[127]) make this material a suitable reinforcing agent for biocoatings. Because of the interfibrillar hydrogen bonds, MFC generally consists of elementary fibrils bundles of around 20 nm in width and several micrometers in length [128]. In spite of its hydrophilicity, different surface modification processes have been explored, enabling the combination of MFC also with hydrophobic polymers [129]. The extraction of nanofibrils from wood may offer the opportunity to exploit the full potential of cellulose as a reinforcing material. In principle cellulose fibres could be disintegrated into 3-5 nm thick elementary microfibrils but because of the complicated multilayered structure of plant fibres and the interfibrillar hydrogen bonds, MFC generally consists of elementary fibrils bundles of around 20 nm in width and several micrometers in length. Cellulosic fibre's hierarchical structure is summarized in Fig. 13 [128].

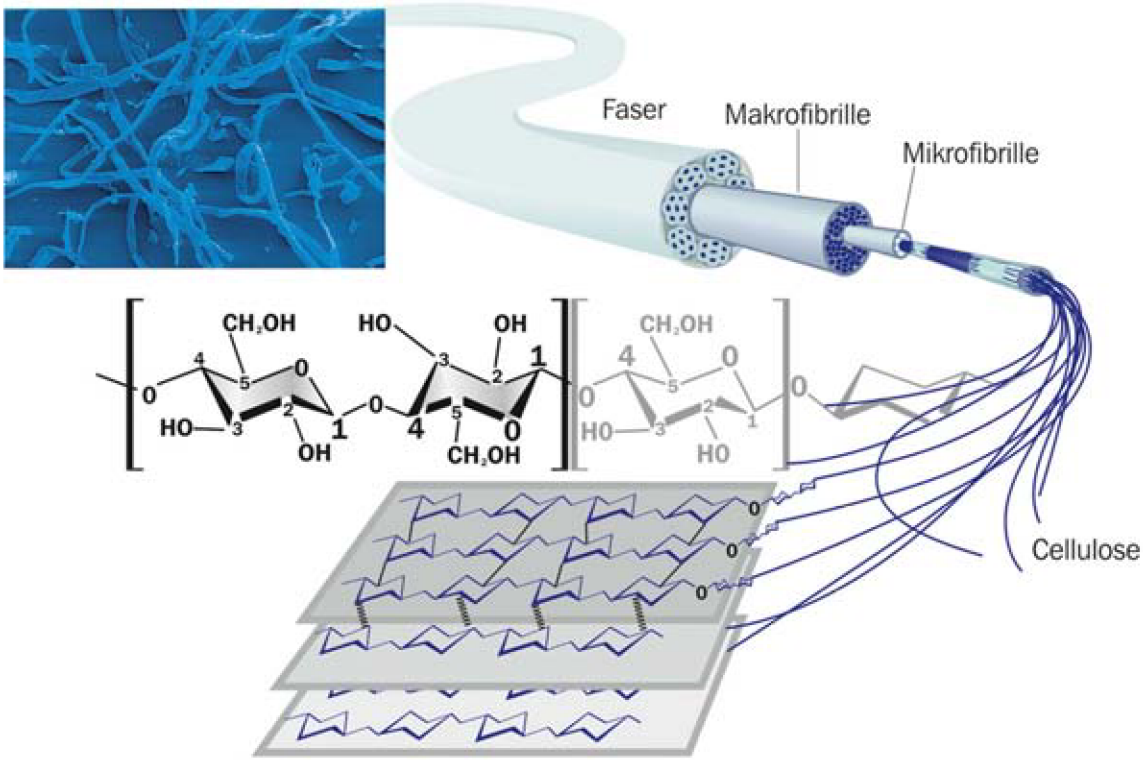

Fig. 13. Hierarchical structure of a wood cell wall [128].

2.4.3. PVA/MFC composites

The noticeable improvement of PVA films mechanical properties by addition of MFC has been extensively reported in several investigations [129 – 135] (Tab. 4). One of the most commonly reported technique for the production of MFC-reinforced PVA composite is film casting [127, 129, 130]. This is a relatively simple, straightforward and low-cost process which enables the production translucent films having excellent mechanical properties.

Matrix	*Type of fibre*	*Source*	*Fabrication technique*	*Reference*
PVA	MFC	Sulfite pulp	Casting/Evaporation	[132]
	MFC	Sugar beet pulp	Casting/Evaporation	[133]
	MFC	Soybean	Casting/Evaporation	[134]
	CNC	Cotton	Casting/Evaporation	[135]
	CNC	Cotton	Casting/Evaporation	[136]
	MFC	Daicel	Casting/Evaporation	[137]
	CNC	MCC	Casting/Evaporation	[138]
	MFC	Regenerated cellulose	Casting/Evaporation	[139]

Tab. 4. Literature overview on different PVA/MFC composites.

Since MFC and PVA are both hydrophilic, their mixing in a water-based suspension does not require any chemical modification. Despite the ease of such technique, each processing step involves several parameters (e.g. temperature, time/energy of mixing, moisture present in the environment, mass ratio PVA/water, mass ratio MFC/PVA) whose variation can deeply influence the microstructure of the resulting composite and therefore its mechanical properties. Beside this, intrinsic parameters related to the two raw materials may vary substantially depending on their production process (purity, molecular weight, degree of hydrolysis of PVA, content of hemicellulose and defibrillation degree of MFC). The sensitivity towards the processing parameters of PVA/MFC composites has been already reported by several works [130–133]. For this reason, the results obtained by different groups are often contradictory because of many factors controlling the process. Anyway, the good dispersion of MFC in the polymer matrix is reported by several authors as a key factor for the achievement of a good reinforcement [130, 137]. Zimmermann et al. [132] reported an improvement of the elastic modulus and tensile strength up to five times and three times respectively, in the case of dispersing 20 wt. % of MFC in PVA.

2.5. Micromechanical models for MFC-reinforced polymers.

Percolation theory, developed by Ouali and co-workers [141] is nowadays widely used in the modelling of the mechanical properties of composites. It assumes random interactions between fibrils as opposed to the unlike earlier models. Percolation theory dates back to the 1940s. An exact quantification of reinforcement effect due to the presence of MFC fibres is a demanding task. Tools available for investigating of the micromechanics of nanocellulose reinforced composites are limited due to the small size of the individual fibrils. It is not possible to handle nanocellulose fibrils mechanically, thus traditional methods used to study the stress transfer in fibre-reinforced composites are not applicable and the values reported in literature present a broad scatter. Raman spectroscopy has been employed to study the strength of single nanofibrils and the stress transfer within nanocomposites [127]. From percolation theory, the composite Young's modulus E_c can be expressed as follows:

$$E_c = \frac{(1 - 2\psi + X_r)E_m E_r + (1 - X_r)\psi E_r^2}{(1 - X_r)E_r + (X_r - \psi)E_m}, \tag{14}$$

where E_r is the reinforcement modulus; E_m is the matrix modulus, X_r is the fibres volume fraction and Ψ is a percolation volume fraction given by Eq. 15:

$$\psi = X_r \left(\frac{X_r - X_c}{1 - X_c}\right)^b, \tag{15}$$

where b is the critical percolation exponent, which is equal to 0.4 for a three-dimensional system and X_c is the percolation threshold, which varies depending on the studied material and their orientation distribution and can be chosen as 5% from Ref. [141].

2.6. Sintering of Bioglass® by spark plasma sintering (SPS)

The spark plasma sintering technique has been gaining importance as it allows the achievement of highly dense ceramic compacts with minor grain growth [142]. In the SPS process, a high energy electric spark is discharged and the powder particle surfaces are more easily purified and activated than in conventional sintering process. The presence of spark plasma significantly enhances rapid densification to densities close to the theoretical one [143]. The high heating rates (typically between 100 and 600° C/min) bring the sample rapidly to high temperatures assisting densification mechanisms over non–densification mechanisms [144]. The mechanical compression of the sample is another factor that accelerates the material densification in the SPS method [142]. These peculiarities allow to achieve densities closer to theoretical one at lower sintering temperatures as well as shorter sintering cycles, compared to conventional sintering and hot press techniques. Therefore, SPS offers a well-established technological and economical approach for fabricating net-shaped bioactive glass materials, including Bioglass® matrix composites. Research endeavors were already published on this topic and they are summarized in Tab. 5. On the other hand, sintering at high heating rates electrically insulating materials might result in non-homogeneous temperature distribution inside the sintering sample and a local increase of temperature. Therefore, this limitation must be taken into account for the sintering of Bioglass® powders as well.

SPS parameters	*Starting powder*	*Crystalline phase*	*References*
950°C , 90 MPa, 100°C	4–150µm 45S5 powder (US Bio-materials)	$Na_2Ca_2Si_3O_9$	Guo et al. [145]
850°C , 40 MPa, h. t. =10 min, h.r. = 100°C /min	45S5 by MO-SCI Corp. (USA)	Non - specified	Jia et al. [146]
950°C , 15 min, other parameters not given	Sol-gel derived bioglass	$Na_2Ca_2Si_3O_9$	Chen et al. [147]
550/600°C	2 µm 45S5 powder	Fully amorphous	Grasso et al. [148]

Tab. 5. Sintering conditions for Bioglass® by SPS, with related powder particle size and detected crystalline phases.

Chen et al. [147] reported a successful sintering of sol–gel derived Bioglass® powder by SPS. In particular, it was found that the sol–gel derived Bioglass®-ceramics sintered with the SPS technique at 950°C for 15 min had a high Young's modulus value of ~110 GPa, which was comparable to that of compact bone and significantly higher than the maximal value achieved by the conventional heat treatment. The obtained ceramic compacts exhibited better cytocompatibility at the early stage of cell culture testing, compared to the conventional Bioglass®. Grasso et al. reported as well the sintering of 45S5 Bioglass® powder by SPS [148]. Temperature and pressures ranging respectively from 350 to 550°C and 70 to 300 MPa were used. Fully dense and completely amorphous 45S5 Bioglass® samples at temperatures as low as 500–550°C were obtained. The fabrication of dense 45S5 Bioglass® compacts at temperatures below 600°C is an interesting result especially for the fabrication of tougher Bioglass® based composites where the Bioglass® matrix remains amorphous

or weakly crystalline. By increasing the sintering temperature up to 600°C the dense samples crystallized to $Na_2CaSi_2O_6$ phase rather than $Na_2Ca_2Si_3O_9$ which is usually achieved at higher temperature.

XRD analysis showed that no crystalline phase forms at the sintering temperature of 550°C. By observing the fracture surface, it was possible to detect the initial morphology of the amorphous starting particles, which have a diameter about 2μm. The SPS sample sintered at 600°C resulted in the formation of very fine $Na_2CaSi_2O_6$ crystallites with size of about 25 nm immersed in an amorphous matrix of Bioglass®.

The acellular in-vitro test revealed that SPS samples sintered at 600°C resulted in faster formation of hydroxyapatite compared to those sintered in absence of pressure (1050°C , 2h), which were highly crystallized. Graphene-filled Bioglass® composites have been also prepared by SPS [149]. Carbon nanotube reinforced Bioglass® composites have been successfully synthesized by Zhang et al. by SPS and conventional sintering [150]. The composites show improved mechanical properties, with SPS technique substantially better than conventional compact and sintering approach. Using SPS the maximum flexural strength and fracture toughness increased by 159% and 105%, respectively. Enhanced strength and toughness are attributed to the interfacial bonding and bridging effects between the carbon nanotubes and Bioglass® powders during crack propagations.

2.7. Exfoliation of h-BN for the production of atomically-thin BNNSs

In the last few years, carbon nanotubes (CNTs), graphene, boron nitride nanosheets (BNNSs) and nanotubes (BNNTs) have attracted attention as reinforcement for glass and ceramic matrices because of their outstanding mechanical and thermal properties. For instance, CNTs have been already reported to toughen brittle matrices [147, 149, 150] by different dominating toughening mechanisms in randomly oriented CNT-amorphous glass matrix composites (e.g. pull–out, bridging, debonding). However, several works reported in literature reveal that the improvement is usually less than the one predicted by theoretical models. Their high specific surface is in fact responsible for their agglomeration which impairs the mechanical properties of the resulting composite. Similarly to graphite, hexagonal boron nitride (*h*-BN) exhibits layered lattice structure with strongly anisotropic chemical bonds [153]. In the basal plane, boron and nitrogen atoms construct a two-dimensional (2D) honeycomb structure with strong covalent bonds (Fig. 14), while the basal planes interact weakly with each other via Van der Waals bonds (with slightly ionic bonds). An individual h–BN basal plane, or a monolayer BNNS, is a honeycomb structure made up of ring units of borazine ($B_3N_3H_6$), the isoelectric and isostructural analog of benzene. Unlike graphene, whose biocompatibility is still under debate, several studies already demonstrated the optimal compatibility of BN–derived nanofillers (BNNTs and BNNSs) [159–161]. Independent assays, both quantitative (DNA concentration assessment) and qualitative (viability/toxicity, early apoptosis, and ROS production detection) were carried out. No significant adverse effects were found up to 7 days since their administration, and no impairments in blood, liver and kidney functionality were highlighted. All the collected data are very promising, suggesting the optimal biocompatibility of other BN-based nanofillers, such as BNNS. Further studies confirmed that BNNSs is non-cytotoxic to osteoblasts, macrophages and human embryonic kidney cells

(HEK-293). Moreover, the possibility of conjugating BNNSs with biomolecules are obviously attractive since the BN-based compounds are usually considered non-toxic and thus biocompatible [157, 158].

Tatarko et al. [159] used cylindrical and bamboo-like boron nitride nanotubes (BNNTs) to reinforce brittle amorphous borosilicate glass matrix materials prepared by spark plasma sintering. The mechanical properties, such as hardness, Young's modulus, fracture toughness, and scratch resistance of the materials resulted as improved. The fracture toughness of the composites showed an improvement of ~30% compared to the pure amorphous glass. Toughening mechanisms such as BNNTs pull-out, crack bridging, stretching, and crack deflection were observed in the reinforced glass matrix composites.

Similarly to graphene, BNNSs exhibit excellent mechanical properties. In one study, the in-plane stiffness of a BN monolayer was calculated to be 247 Nm^{-1} [160]. Li et al. [161] found out that the bending modulus of BNNSs increase as their thickness (i.e. the number of layers) decreases. This was attributed to the defect-induced stacking faults between nanosheets layers resulting from the exfoliation process. So far, BN nanosheets have successfully been fabricated either *via* top down or bottom-up techniques which will be not reviewed here. The so-called top-down methods involve the exfoliation of micro-sized h-BN particles into BNNSs constituted by few atomic layers by mean of mechanical forces. Pulling forces (mechanical cleavage) or shear forces can break the weak Van der Waals interaction between layers and leave the strongly sp^2 bonded in-plane structure intact. Ball milling have been already used for thickness reduction of BNNSs as well as for other layered materials, for instance for graphene production [162].

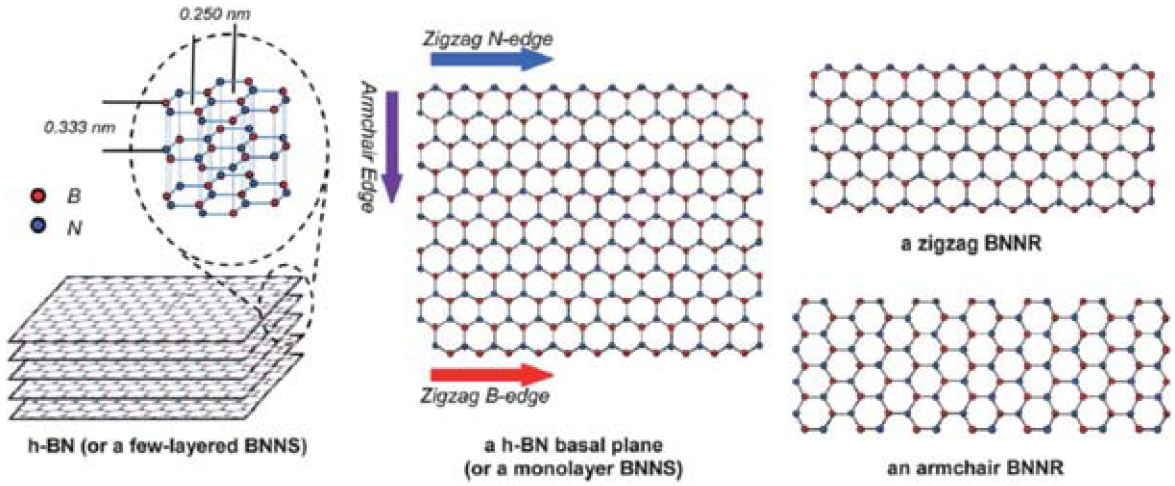

Fig. 14. Structural basics of 2D BN nanostructure [160].

The main advantage which distinguishes this process is the capability to treat tens of thousands of particles in one run, producing a large amount of BNNSs at one time. The exfoliation mechanism is schematized in Fig. 15a. Further studies also demonstrated that mechanically peeled 2D sheets have fewer defects than those produced by chemical methods [163]. Unfortunately it is difficult to chemically intercalate the partially ionic BN layers because of the weaker inter-layer exchange repulsion and stronger inter-layer attraction [160]. However, an excessive ball milling energy might

destroy or disorder the crystal structure and introduce a great number of defects [162]. The milling modes (shearing or vertical impact) as well as milling energy can be adjusted by varying ball sizes and rotating speed [164]. The solvent have to be chosen according to two parameters: surface tension and viscosity [162]. Higher viscosity is preferred because of the higher shear forces which can arise. The surface tension should be as close as possible to the material which has to be exfoliated. For BN it has been found by mean of contact angle measurements and it ranges from 50 to 60 mJ/m^2 [165]. For this reason organic solvents are preferred instead of water, whose surface tension at 25°C is nearly 70 mJ/m^2 [166].

Nevertheless, the exfoliation of BNNS in aqueous medium was also achieved by mean of high energy sonication (Fig. 15b) [167]. A "clean" aqueous dispersion of BNNSs was obtained without the use of surfactants or organic functionalization. Besides few-layered h-BNNSs, there was also evidence on the presence of monolayered nanosheet and nanoribbon species. Most nanosheets were of reduced lateral sizes and this was attributed to the cutting of parent h-BN sheets induced by the sonication-assisted hydrolysis (evidenced by the ammonia test and spectroscopy results).

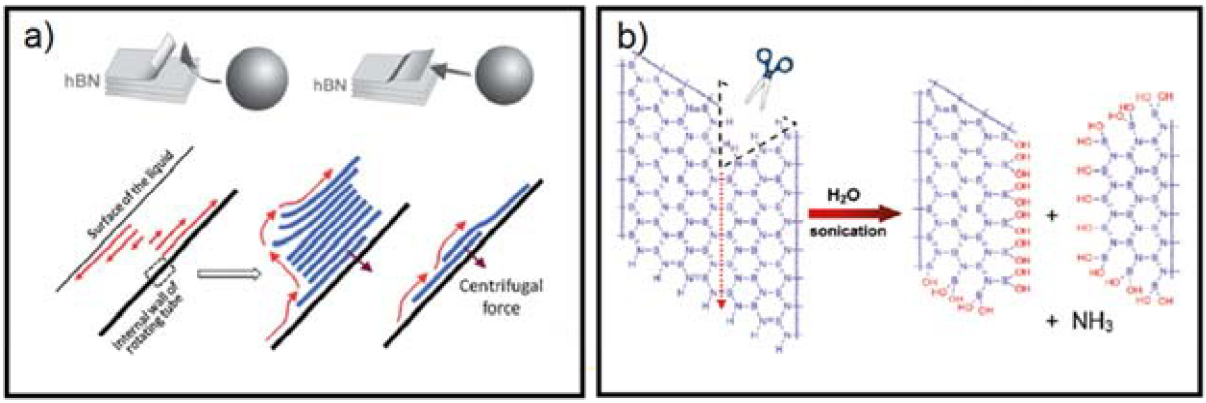

Fig. 15. Mechanism of exfoliation by ball-milling [168]; b) Exfoliation obtained by high energy sonication probe in water, stabilization trough hydrolysis of B-N at the edges and release of NH_3 [167].

In a recent work, akermanite (AKM) scaffolds reinforced with BNNSs were fabricated by selective laser sintering [169]. The influence of BNNSs on microstructure and mechanical properties was evaluated as beneficial. The improvement of the mechanical properties were ascribed to sheet pull-out, grain wrapping and mismatch of thermal expansion coefficient. Apatite formation was observed in SBF medium. The adhesion of MG63 cells provided a further proof of the excellent biocompatibility of these scaffolds.

3. Aims of the work

The main aim behind this work is the mechanical improvement of bulk Bioglass® and Bioglass®–based porous scaffolds. Such goal, which is crucial for satisfying the requirements of load-bearing applications, should be achieved by preserving the biocompatibility and without compromising the bioactivity of the material. A preliminary set of experiments coupled with finite element calculation were performed in order to individuate the morphological factors which mostly affect the mechanical response of a brittle foam undergoing uniaxial compressive and tensile load. According to these results, processing parameters (i.e. slurry's viscosity, type of solvent, amount of binder, number of dipping, removal of exceeding slurry, foam's cell size etc.) were modified consequently.

Concerning the reinforcement of porous scaffolds, it has been followed the approach already described in several works, which involves the addition of a polymeric coating on the scaffold's surface in order to increase strength and the work of fracture of the structure. The novelty which distinguishes the present work is the use of a composite coating, comprised of polyvinyl-alcohol (PVA) and microfibrillated cellulose (MFC), in order to obtain superior reinforcing effect in comparison with neat-polymer coatings commonly reported in literature. To best of authors' knowledge, MFC have never been used before for the reinforcement of Bioglass® scaffolds. This is a surprising fact, by considering the outstanding mechanical properties and functionalization possibility that MFC offers. Another aspect which will be investigated is to determine in which way the coating allows such remarkable extension of the elastic domain. More specifically, it will be determined through computational methods, which factor among the stiffness of the coating material and the extent of coating infiltration into surface cracks is the most effective in terms of reduction of the stress concentration at defect sights. Although several works dealing with the mechanical properties of polymer-coated mechanical properties were published up to know, there is still paucity of computational results which clarify this aspect. As an experimental counterpart, the rheological properties of the PVA and PVA/MFC aqueous solutions and their wettability towards Bioglass® surface will be investigated. Coated scaffolds with different ratio of PVA/MFC will be fabricated and tested under uniaxial compressive and tensile mode. Outputs from viscosimetry and wettability measurements will constitute a useful tool to better interpret and correlate the outputs from FEM and the experimental results from compressive and tensile test.

The second part of this work is focused on the production of bulk Bioglass® and Bioglass®/BNNSs composites samples by spark plasma sintering (SPS) technique. The author's interest is to experiment the advantages that such technique may offer in comparison with conventional sintering in oven. In particular, one of the primary aims will be to ascertain whether high heating rates (ranging from 100 to 300°C /min), the application of mechanical pressure and controlled atmosphere, could lead to the achievement of a finer glass/crystalline microstructure or non-equilibrium phases with peculiar properties.

Due to their remarkable mechanical properties and assessed biocompatibility in comparison with carbon nanotubes (CNTs), BNNSs will be considered as a reinforcement for the production of BNNSs–reinforced Bioglass®. BNNSs will be produced through a top-down approach from

a commercial BN powder. For this purpose ball milling and high energy sonication will be used. BNNS concentration in aqueous solution will be measured by UV-spectroscopy. BNNSs size and quality will be than assayed by SEM and TEM. The composite will be produced by sintering in oven and SPS.

To summarize, the main research activities covered will be:

- Production of scaffolds by using different kind of slurries;
- Coating of scaffolds by different polymers;
- Mechanical test of bulk Bioglass®;
- Mechanical test of coated scaffolds (uniaxial compression, tension);
- Microstructural characterization of scaffolds and fractographic analysis by SEM;
- Production of coating film;
- Mechanical test of coating material;
- FE modelling of foam's unit cell and coating effect;
- Production of and characterization of BNNSs by top-down approach;
- Sintering of bulk Bioglass® and Bioglass®/BNNSs by SPS.

4. Methods

4.1. Materials

Commercially available alumina-based foams (Vukopor®A, produced by Igor Láník – Techservis, Boskovice, Czech Republic) were used for the test methodology development and as well as for analysis of performance during mechanical loading and fractographic analysis. Material composition is: 85 vol. % Al_2O_3, 14 vol. % SiO_2, 1 vol. % MgO. Specimens were produced by foam replication technique using polyurethane foams as a sacrificial template. Typical for this kind of ceramic foam fabrication is a highly porous structure with open type of porosity and triangular holes within the struts. Two types of cell sizes were applied for investigations, namely 10 and 60 pores per linear inch (PPI). This corresponds to typical cell sizes of 2.2 (±1.2) mm and 0.8 (±0.3 mm), respectively.

For the production of Bioglass-based scaffolds, commercially available bioactive glass powder (45S5 Bioglass® composition: 45 wt.% SiO_2, 24.5 wt.% CaO, 24.5 wt.% Na_2O%, 6 wt.% P_2O_5, Schott AG, Germany) having average particle size of 4 μm (d_{50}: (4.0 ± 1.0) μm d_{95}: ≤20 μm) was used. A reticulated polyurethane foam (Eurofoam, Germany) having 45 and 60 pores per linear inch (PPI) was used as sacrificial template for the foam replication method. The foam was supplied in form of 16 mm thick panels and then cut into cubes having dimension of 13×13×13 mm^3 (designed for compressive samples) and 5×10×20 mm^3 (designed for tensile samples).

Fully hydrolyzed PVA, d=1.269 g/cm^3 (Sigma Aldrich Chemie GmbH, Germany),was either used as binder for slurry and for coating preparation. Poly(vinyl butyral-co-vinyl alcohol-co-vinyl acetate) (PVHB), having average M_w = 170.000–250.000, supplied by Sigma Aldrich Chemie GmbH (Germany) was used as binder for ethanol-based slurry.
MFC hydrogel having 2% content of fibres was supplied by Borregard (Sarpsborg, Norway).
Hexagonal BN powders were supplied by Saint-Gobain.

4.2. Samples preparation

4.2.1. Porous scaffolds

Scaffolds were prepared by foam replication technique. PU pieces were first cut into pieces having desired sizes by using a hot–wire cutting machine (Proxxon, USA). A water–based Bioglass® slurry was prepared by dissolving 1 g of PVA into 50 ml of deionized water and by adding Bioglass® powder until reaching a solid fraction of 30% wt. The slurry was stirred for at 500 rpm for 2 h at 90°C and then cooled down at room temperature. Templates were immersed in the slurry for 10 s and then retrieved. The exceeding slurry was manually squeezed out and resulting green bodies were dried in ventilated oven at 60°C for 1 h. The ethanol-based slurry was prepared by dissolving 0.7 g of PVB in to 50 ml of ethanol and stirred at 50°C and 500 rpm for 1 h. Also in this case, the powder was then added to the solution in order to obtain slurry having solid mass fraction of

30 wt. % (by assuming the density of ethanol as 0.79 g/cm^3). Drying of samples was accomplished in few minutes, due to the superior volatility of ethanol. For all scaffolds, sintering was carried out in oven by following the parameters shown in Fig. 5b.

For the preparation of coated scaffolds, and MFC gel, with 2 wt. % fibres content was used. The process was carried out in two steps. First, 1 g of PVA was dissolved into 50 ml of water at 90°C by vigorous stirring for 1 h. The MFC gel (corresponding to the desired amount of dry fibres) was then added to the PVA water-solution. Following this procedure, two different batches were produced, containing respectively 5 and 10 wt. % of MFC. The derived coating will be referred as PVA/5%MFC and PVA/10%MFC. All the mixtures PVA/MFC were stirred for 2 h, sonicated for 30 min and stirred again for 3 h at room temperature. Scaffolds were soaked into the mixture for 5 min and then manually retrieved and dried in a ventilated oven at 50°C for 24 h. Neat PVA-coated scaffolds were also produced for a matter of comparison. Soaking was repeated twice in order to ensure the formation of a continuous coating film all along the struts surface.

The stand-alone coating specimens were produced by casting the remained of the PVA and PVA/MFC batches in a custom-made Teflon mold. By following the same processing route used for coatings preparation, pure PVA, PVA/5%MFC and PVA/10%MFC films were obtained by casting the mixture in a custom-made Teflon® mould. After drying for 24 h in ventilated oven at 50 ºC, a continuous translucent film was formed and stripes having 50 mm length and 35 mm width were manually with a razorblade cut to be tested under uniaxial tension. In the particular case of the PVA/10%MFC film, samples were also produced from mixtures having the same composition but stirred for different time (24 and 48 h), in order to assess whether the mixing time may influence the homogeneous dispersion of the MFC fibres in the resulting composite films. Thickness and width of the stripes were measured by a Mitutoyo IP56 digital micrometer (± 0.0005 mm accuracy).

4.2.2. Bulk samples

Bulk Bioglass® samples were sintered in two different ways: in conventional furnace and by SPS technique. In the first case, the remainder of slurry used for fabrication of scaffolds was poured in a rubber mold having diameter ~ 40 mm and kept drying for 7 days at room temperature. After drying, the green body was sintered at 1050° C for 1h, using a heating rate of 2°C /min and a cooling rate of 5°C /min, similarly to the process reported in Ref. [45] (Fig. 5b). The furnace used was HtIndustry (HTH8, s. r. o., Czech Republic). Dense disk-shaped samples were thus obtained, having thickness and diameter equal to 5 and 30 mm, respectively.

SPS facility HPD 25/1, (FCT Systeme, Germany) was used for the production of pure Bioglass® and Bioglass®/BNNSs bulk samples. Different sintering routes were tested, i.e. by extensively varying parameters such as sintering temperature (T_s), heating rate (h_r), holding time (t_h), pressure (P) and atmosphere (i.e. argon for pressure–assisted, vacuum for pressureless sintering), in order to establish the optimal conditions for the achievement of a dense and homogeneous microstructure.

In the first set of sintered samples, the denomination “Pre” stands for “pressure assisted” while the denomination “PL” stands for pressureless. The numbers refer to the sintering program used and,

whose details are supplied in the appendix. For the second set, all samples were sintered in absence of pressure and parameters such as holding time and sintering temperature were varied. For those the denomination PB (pure Bioglass®) was used.

The density of each sample was measured by Archimede's method and was considered as a rapid indicator of the quality of samples and the efficiency of the sintering process. As the optimal combination of parameter was located, another set of samples was produced, by finely tuning the parameter. Bars were then cut for flexural strength and Chevron fracture toughness by using a diamond saw.

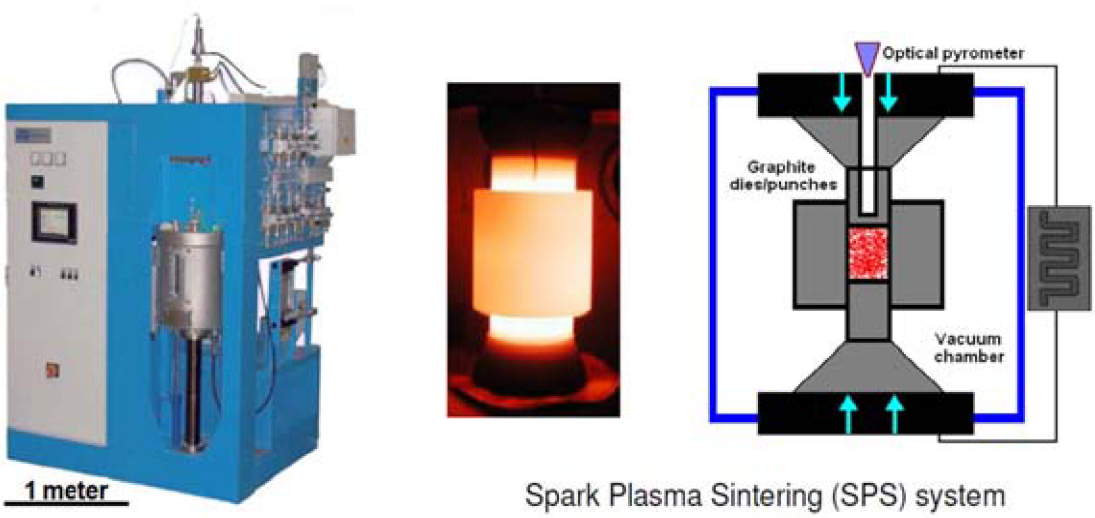

Fig. 16. SPS facility HPD 25/1, (FCT Systeme, Germany) and its functioning scheme.

4.3. Exfoliation of BNNSs

4.3.1. Ball milling

Hexagonal boron nitride (*h*-BN) particles were exfoliated into BNNSs by ball milling and by high energy sonication. Planetary mill (Pulverisette 6, Fritsch, Germany) was used for this purpose. 0.1 g of *h*-BN was put in a custom-made Teflon® jar, together with milling media. Zirconia balls having diameter of 10 mm were used (Tosoh Corp., Japan). Two different polymeric solutions were used as milling medium. The first one was obtained by dissolving 2g of PVA in 100 mL of deionized water. The second one was obtained by dissolving 1g PVHB in 50 ml of isopropyl-alcohol. The function of solubilized polymer is two-fold: the first is to increase the viscosity of the system in order to maximize the shearing forces acting on the particles and stabilize the BNNSs once they are exfoliated, intercalating them and preventing re-agglomeration. For each system, low (150 rpm) and high (350 rpm) energy ball milling were used for 12 h in order to determine the best milling regime. For each batch, half of the mixture was collected and stored for one week in order to let the heaviest particles to sediment. Then few drops of supernatant were harvested for TEM analysis. The rest was poured in a Petri dish and dried for 72 h at 60° C. The resulting film was carbon coated and observed by SEM.

4.3.2. Sonication

Two grams of h-BN powder were added to 500 ml of deionized water, manually mixed and the obtained suspension was sonicated for 10 h by a high energy sonicating probe (Q700, QSonica, U.S.). The solution was surrounded by an ice bath to keep its temperature down as much heat is created during prolonged sonication. Once finished the solution was kept resting for 24 h in order to allow the coarser particle to deposit on the bottom. The supernatant was then withdrawn by using an electronic pipet in order to limit the movement of the liquid and consequent remixing of deposited particles. The suspension was then centrifuged at three increasing speeds (3000, 4000 and 5000 rpm) for 30 min each. Again, the supernatant was collected by mean of a pipette, being careful to avoid the withdrawal of the solid part deposited during centrifugation. According to this, a precise amount of BNNSs suspension was added to the Bioglass® powder batch in order to obtain a BNNSs wt. % equal to 0.5. A drop of suspension was deposited on copper substrate and let dry for 24 h.

4.4. Characterization

4.4.1. Microstructure

Archimedes' method was used to measure the density of bulk Bioglass® and Bioglass®/BNNSs composite using distilled water as buoyant. All the weight measurements have been performed using a digital balance (Denver instruments, USA) having an accuracy of ± 0.0001 g. Density of sample was obtained employing the relation given below:

$$\rho = \frac{w_a}{w_a - w_b}\rho_b, \tag{16}$$

where w_a is the weight of sample in air, w_b is the weight of sample in buoyant and ρ_b is the density of buoyant. Density of Bioglass® was assumed equal to 2.7 g/cm^3 from literature values.The error on density measurement is assumed below 1%. Field emission gun-scanning electron microscopy FEG-SEM (Tescan Lyra 3 XMU, Czech Republic) was used to carry out the microstructural characterization of both dense Bioglass® and Bioglass®-based scaffolds. In the first case, bulk samples were polished by ceramographic techniques, in order to obtain desired surface finishing (~ 1 µm) and then coated by carbon.
Image analysis of SEM micrographs enabled to assess the amount and morphology of pores as well as the pore size distribution. Some of the samples were previously etched in HF solution in order to better distinguish the crystalline domains. Concerning the scaffolds, SEM analysis macro-structural features (cell size, struts thickness) as well as micro-features (struts defects, fractographic analysis of broken struts) and toughening mechanism enabled by the presence of coating. For observation of polymer-coated scaffolds, SEM Zeiss (Brno University of Technology) have been used. The porosity of each scaffold before coating was calculated by means of geometrical weight–volume measurements as:

$$P = \left(1 - \frac{\rho_s}{\rho_b}\right), \quad (17)$$

where ρ_b is the density of the bulk Bioglass® (assumed 2.7 g/cm^3 [170]) and ρ_s is the apparent density of the scaffold (weight/volume ratio). The porosity of coated samples was calculated by the modified relationship:

$$P = \left(1 - \frac{\rho_s}{\rho_b} - \frac{\rho_{cm}}{\rho_{ct}}\right), \quad (18)$$

where ρ_{cm} is the coating density calculated for each sample as:

$$\rho_{cm} = \frac{w_f - w_i}{V}, \quad (19)$$

where w_i and w_f are respectively the weight of the scaffold before and after coating and V is the scaffold's volume and was calculated by measuring the size of the specimens. ρ_{ct} is the theoretical coating density calculated by the mixture rule as:

$$\rho_{ct} = X_{MFC}\rho_{MFC}X_{PVA}\rho_{PVA}, \quad (20)$$

where X_{MFC} and X_{PVA} are respectively the mass fractions of MFC and PVA and ρ_{MFC} and ρ_{PVA} are their densities. ρ_{MFC} is assumed equal to 1.14 g/cm^3 [171]. A quantitative assessment of pores size and struts thickness distribution was carried out by image analysis (ImageJ software) on low magnification pictures obtained by optical microscopy (Stereomicroscope Olympus Z61). The cells and struts of interest were manually selected and their mean diameter and thickness were measured. An accurate measurement of the shrinkage occurring during sintering was performed by micro–computed tomography (μCT) at Arizona State University (ASU). The as-reconstructed data set obtained from the coated PU templated was defined as PRE while POST was the one obtained from the sintered body. POST was filtered with a non-local means filter in Avizo Fire filter after reconstruction. Further parameters set for the scans are listed in Appendix I.

XRD analysis was performed by X-Pert X-ray diffractometer with CuKα radiation source, Ni filter, operated at 40 kV and 20 mA. A θ-2θ configuration was used to collect data in the interval of 10° < 2θ< 65°, steps of 0.01°. The crystallite size of the detected phases, was estimated via Scherrer's equation [172] on the peaks of highest intensity:

$$\beta = \frac{k\lambda}{\varsigma \cos\theta}, \quad (21)$$

where β is the full width at half maximum of the peak corrected of the instrumental broadening, ς is the crystallite size in meters, λ is the wavelength of the Cu Kα line (1.5406 × 10^{-10}m) and k is the Scherrer constant, equal to 0.89. TEM (JEOL HRTEM) and FEG-SEM (Tescan Lyra 3 XMU, Czech Republic) were used for the characterization of BNNSs.

The concentration of suspended BNNSs was then measured using UV–Visible spectroscopy (Perkin Elmer-Lambda 950) by recording the absorbance at 300 nm and calculating the concentration using Beer–Lambert's law [173]:

$$A/l = \alpha C, \tag{22}$$

where A is the absorbance, l is the path length, α is the extinction coefficient with a value of 2367 ml/mg/m [174] and C is the concentration of the suspension.
Elemental composition analysis using energy dispersive X-ray spectroscopy (EDS) was performed by EBSD detector (Oxford Instruments) equipped with Aztec™ control system.

4.4.2. Thermal characterization

Differential thermal analysis was carried out by NETZSCH5, (temperature range: 25 – 1200°C; heating rate 5°C $\cdot min^{-1}$). Pure alumina powder (Sigma Aldrich) was used as a reference material and for the baseline determination. The characteristic temperatures of glasses were determined directly from DTA plots. The crystallization was studied by DTA using a non-isothermal method. The temperatures corresponding to the characteristic viscosity points (first shrinkage, maximum shrinkage, softening, half ball and flow) were obtained from the photomicrographs taken during the hot-stage microscopy experiment. For this purpose, a Leitz–Wetzlar heating stage optical microscope was used. Sintering was performed in air at a heating rate of 20°C /min. The samples were prepared by manually pressing the powders in a small cylindrical mold (base diameter ~ 1 mm, height ~ 3 mm). Sample shrinkage was assumed as isotropic and was estimated by Eq. 4. The characteristic temperatures of glasses such as, first glass transition temperature T_{g1}, onset crystallization temperature T_x, peak crystallization temperature T_c and second glass transition temperature T_{g2} were assessed directly from the DTA plots.

4.4.3. Mechanical characterization

4.4.3.1. Bulk specimens

Bulk Bioglass® specimens were cut into bars having cross-sections nominally 2.5 × 1.6 mm. Bars were polished by ceramographic technique with diamond paste up to 1 µm size and edges were champhered according to Ref. [175]. The span length used was 16 mm. All the tests were carried out at room temperature and the speed of the moving support was 0.5 mm/min. The peak force (P) was used to calculate the bending strength (σ) from Ref. [175]

$$\sigma = \frac{3PL}{2dw^2}, \tag{23}$$

Where d and w are the depth and width of the beam, respectively.

The Vickers hardness (HV) was determined by Vickers indentations on polished surfaces of the specimen microtester Zwick/Roell ZHU/Z2.5 (Germany). For statistical reasons, 13 indents were

applied on each sample. Speed point of contact, load application and load removal were set respectively set as: 0.05 mm/min, 0.125 N/s and 0.01 mm/min. The impressions were measured by SEM. The Vickers hardness value was calculated by the following equation [176]:

$$HV = 1.8544\frac{P}{d^2}, \tag{24}$$

where P is the applied load and d the diagonal length of the Vickers indentation mark (mm). The Martens hardness (HM) was determined as well from the indentation test, being defined as follows:

$$HM = \frac{P}{A_s(h)} = \frac{P}{26.43h_m^2}, \tag{25}$$

where $A_s(h)$ is factor for indenter (26.43 for Vickers) and h_m is the maximum depth after waiting time. The indentation fracture toughness (IF) was determined as well by the measurement of the crack lengths created by the Vickers indentations by using the equation proposed by Anstis [177].

$$K_{IC} = 0.016 \cdot \left(\frac{E}{H}\right)^{\frac{1}{2}} \cdot \frac{P}{c^{3/2}}, \tag{26}$$

where E is the Young's modulus of materials, H is the Vickers hardness of materials, P is the indentation load and c is the indentation cracks length. At least 10 indents were measured for each material composition in randomly well separated areas. Radial crack lengths were measured analysing SEM images taken in backscattered electron mode.

Chevron-notched beam were cut using a diamond wheel having thickness 0.17 mm. The specimens were loaded in three-point bending (span of 8 mm) at a constant cross-head speed of 0.1 mm/min at room temperature. The cross sections sizes 2.5 × 1.6 mm. Load-deflection traces were recorded and the fracture toughness was calculated from the maximum load (F_{max}) and the corresponding minimum value of geometrical compliance function (Y^*_{min}) using the equation [178]:

$$K_{IC} = \frac{F_{max}}{bd^{1/2}} Y^*_{min}, \tag{27}$$

where b and d are the width and thickness of the beam, respectively. The notch angle, and notch depth (a_0) were measured from optical micrographs of fracture surfaces by ImageJ.

The Young's modulus (E) was measured by impulse-resonance technique on rectangular samples using a commercial testing instrument (GrindoSonic: MK5 "Industria l", Belgium). Young modulus is related to the experimentally determined resonant frequency according to the following equation [179]:

$$E = 0.9465\left(\frac{mf_t^2}{b}\right)\cdot\left(\frac{L}{b}\right)^3\cdot T_1, \tag{28}$$

where m is the mass of the bar, b is the width of the bar, L is the length of the bar, t is the thickness of the bar, f_t is the fundamental frequency of the bar in flexure. T_1 is a correction factor for fundamental flexural mode to account for finite thickness of the bar, Poisson's ratio and other constants and it is calculated as:

$$T_1 = \left[1 + 6.585\left(\frac{b}{L}\right)\right], \tag{29}$$

Poisson's ration is defined as the absolute value of the ratio of transverse strain resulting from uniformly distributed axial stress below the proportional limit of the material. The mechanical performance of the Bioglass® scaffolds with and without coating was evaluated by uniaxial compressive and tensile tests.

The reliability (i.e. the probability of failure) of brittle materials was quantified by a three parameters Weibull function. Weibull distribution is given as a cumulative distribution by Eq. 30 [180]:

$$P_f(\sigma) = 1 - exp\left[-\frac{\sigma - \sigma_t}{\sigma_0}\right]^m, \tag{30}$$

where $P_f(\sigma)$ is the probability of failure at a stress σ, σ_0 is a scaling constant, σ_t is the threshold stress below which no failure occurs in the material, and m is the Weibull modulus. The Weibull modulus, m, determines the reliability of the materials, with larger values corresponding to more reliable materials. To evaluate P_f the median rank estimator, also known as Bernard estimator can be used [181]:

$$\mathrm{P_f} = \frac{\mathrm{i} - 0.3}{\mathrm{N} + 0.4}, \tag{31}$$

being N is the total number of specimens tested and n is the specimen rank in ascending order of failure stress. To get an unbiased estimate of the failure probability, the recommended number of specimens is between 20 and 30. The Weibull distribution was derived using the principle of the weakest chain link and its major advantage consists in the possibility to express its distribution function analytically.

4.4.3.2. Uncoated and coated Bioglass®-bases scaffolds

Compressive tests were carried out by using an Instron8862 (Instron®, U. S.) uniaxial machine with electromechanical actuator and integrated with BlueHill® software. The cross-head speed was set as 0.5 mm/min and 100 kN load cell was used.

Concerning tensile tests, Z050 uniaxial screw-driven load machine (Zwick GmbH, Germany) with 1kN load cell was used applying a cross-head speed of 0.1 mm/min. Compressive and tensile strength values were determined by dividing the maximum force in the loading diagram by the cross-sectional area of the specimen measured after the test. In order to ensure homogeneous transfer of load forces from tensile apparatus to specimens, the latter were fixed on two tusked aluminum pots by adhesive mean. The aluminum pots were subsequently clamped by respective holders. The upper holder was supplied with cardan shaft and claw which was mounted by pivot and lower claw was connected by a bulb to the shaft. In this way, difficulties connected with alignment of specimen and loading axis were overcome. The adhesive medium used for fixation of specimen in the pot was Duracryl Plus® (Spofa Dental, Czech Republic), an epoxy resin composed by powder medium and liquid activator. This particular grade of resin exhibited controllable viscosity of fixative liquid and thereby controllable wettability of specimens with different cell size. A further advantage is the hardening time which does not exceed 20 minutes. This method was already successfully used by Řehořek et al. [182].

The energy per unit volume E_V ($J \cdot mm^{-3}$) absorbed by the scaffold until the first fracture event was defined as the energy necessary to deform a specimen from the unloaded condition to the failure strain ε_f, and was calculated as the area under the stress-strain curve up to ε_f [183]:

$$E_V = \int_0^{\varepsilon_f} \sigma(\varepsilon) d\varepsilon, \tag{32}$$

The elastic modulus of scaffolds was determined by resonance method and by measuring the slope of the elastic region in the compressive stress–strain curves. For each kind, five curves were considered and average slope was calculated. The latter is an approach commonly used and accepted in the literature [180] although leading to underestimation of the elastic modulus [186]. On the other hand, the resonance technique could have been applied only for the polymer–coated specimens. The impact of the small hammer would in fact cause damage in the uncoated specimens due to their high brittleness.

For the tensile test of coating stripes, a micro-testing machine MTS Tytron250 (USA) with 200 N load cell was used. Pneumatic grips having rubber surface were used in order to ensure the necessary clamping strength during deformation of samples without damaging their surface. For each kind, five samples were tested and average values of tensile strength and elastic modulus were calculated. The strain was defined by the clamp displacement relatively to the initial distance, and the Young modulus was obtained as the slope in the initial linear part of the stress-strain curve. Tensile strength values were determined dividing the maximum load recorded by the cross-sectional area of the specimen measured before the test.

4.5. FEM modelling

4.5.1. The influence of cavity derived from replica process

As previously stated, ceramic foams obtained by replica process, closely mimic the structure of the polymeric template which they are derived from. The latter is in turn obtained by foaming of a liquid phase involving nucleation and expansion of bubbles. Starting from this assumption, it has been decided to model the structure of the ceramic foam as it was derived from a foaming process, following the approach already used by Sihn et al. [187]. According with the minimum surface energy principle, during foaming process surface energy of nucleation and expansion of bubbles are minimal when the centers of bubbles coincide with the four vertices of a tetrahedron. Therefore, the unit cell consists of four struts connected to a common node and oriented approximately 109° to one another in three-dimensional space.

For the model hereby described, the vertices of the tetrahedron are defined by first considering a cube. For defining the unit cell, the dimension of the cube is taken as $2a \times 2a \times 2a$ in x-, y- and z- directions and the origin of the Cartesian axes (point 0, 0, 0) is located at the center of the cube (Fig. 17). The vertices of the tetrahedron confined in the cube are the four corner points of the cube that are located diagonally to each other on the faces of the cube (i.e., points 2, 4, 5, 7 represented in Fig. 17. Connecting the four corner points then generates a tetrahedron, whose volume is $V_{tetra} = 8a^3/3$. This tetrahedron can be further divided into four equal tetrahedral sub-domains containing the origin of the tetrahedron. The vertices of the each sub-tetrahedron are shown in Fig. 17 as 0-2-7-4, 0-7-5-4, 0-4-5-2 and 0-2-7-5, respectively. One of these sub-domains can be arbitrarily chosen and four equal spheres growing from its four vertices (the four corner points) can be generated. The spheres represent bubbles that are produced during the foaming process.
The radii of the spheres (R) will determine the porosity of the unit cell of the foam. By subtracting the volume of the bubbles (spheres) from that of the sub-tetrahedron the unit cell of the foam can be created, as shown in Fig. 18. The porosity (φ) of the foam can be calculated by $= 1 - V_{unit} = V_{tetra}$, where V_{unit} is the volume of the unit cell. As the bubble grows, the unit cell results in different shapes. Basically, three steps of foaming expansion can be observed: the nucleation of bubbles and their initial growth, corresponding to a radius length ranging from 0 to $(2a)^{1/2}$. As the bubbles come into contact with each other the radius length reaches the value $(2a)^{1/2}$.

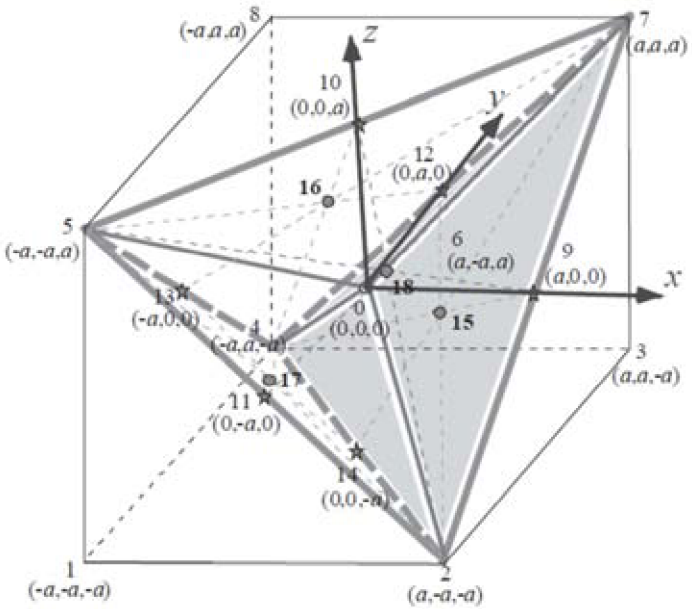

Fig. 17. Points and lines in a cube define the tetrahedron for generating a unit cell of open cell foam [187].

This corresponds to a foam having 78% of porosity. For further expansion, the bubbles coalesce with each other originating foams having high degree of interconnected porosity (>78%). The latter closely resemble the structure exhibited by open cell ceramic foams which are object of this study. The original tetrahedron and unit cells having different degree of porosity are shown in Fig. 19.

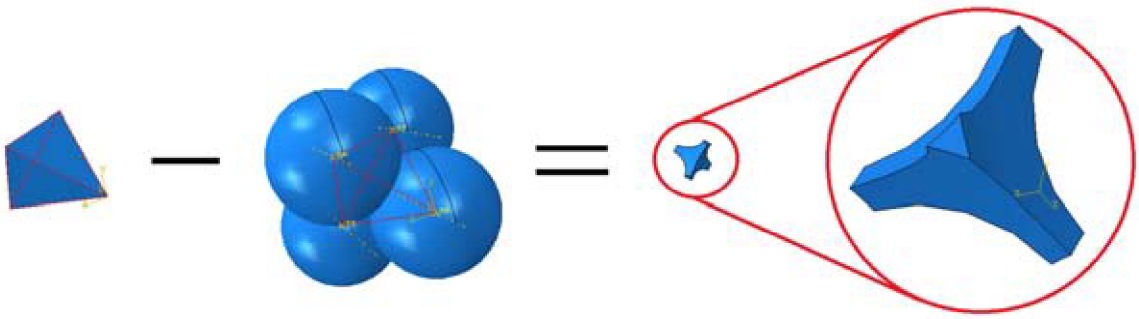

Fig. 18. Tetrahedron and spheres used to generate a unit cell of the foam.

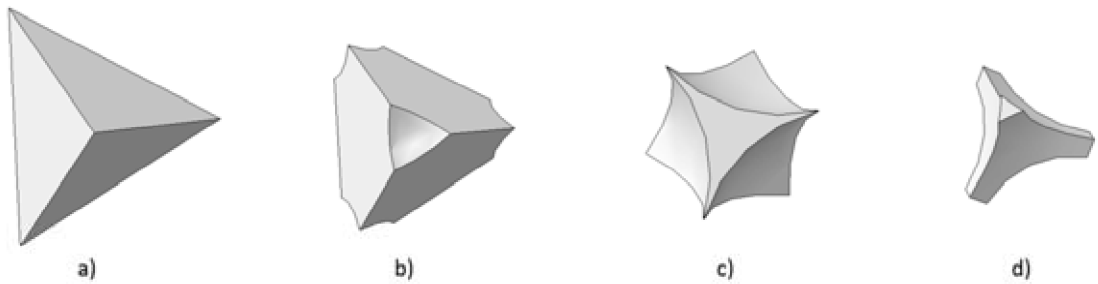

Fig. 19a) Tetrahedron from which unit cell generate. b) Unit cell with φ = 10% (0 < R < $\sqrt{2a}$); c) Unit cell with φ = 78% (R = $\sqrt{2a}$); d) Unit cell with φ = 90% ($\sqrt{2a}$ < R < $a\frac{2\sqrt{6}}{3}$).

As a final step, the cavity inside can be produced by creating a smaller unit cell and by subtracting it from the original one. The original structure will be named as "*O*" and the one to be subtracted as "*S*" .The operation is shown in Fig. 20. The process is repeated by using three S-units having increasing size and three hollows cell units having increasing size of cavity are thus produced. It is opportune to point out that *"O"* and *"S"* unit cells were created starting from a cube having same sizes. The sizes of the resulting unit cell exclusively depend on the radius of bubbles. In Tab. 6 the four unit cells here analysed are renamed and the sizes of the cube and spheres radii which has been used for creating both *O*-unit (R) and *S*-units (R') are summarized.

Unit cell	*Cube edge 2a (mm)*	*R (mm)*	*R'(mm)*
O	10	7,9	0
O-S1	10	7,9	8,15
O-S2	10	7,9	8,1
O-S3	10	7,9	8,0

Tab. 6. Renamed unit cells and sizes of generating parts are summarized.

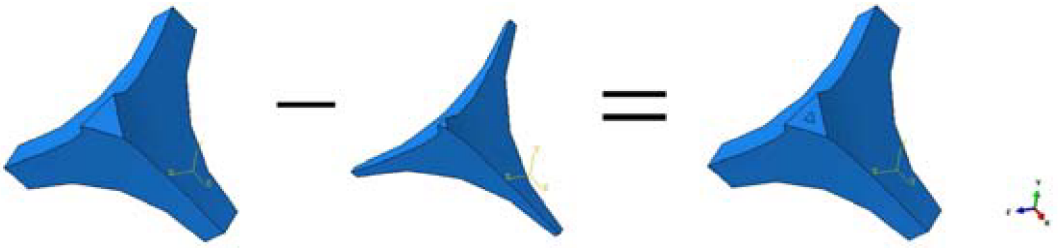

Fig. 20. Hollow structure is created by subtracting from the original unit cell one having smaller size.

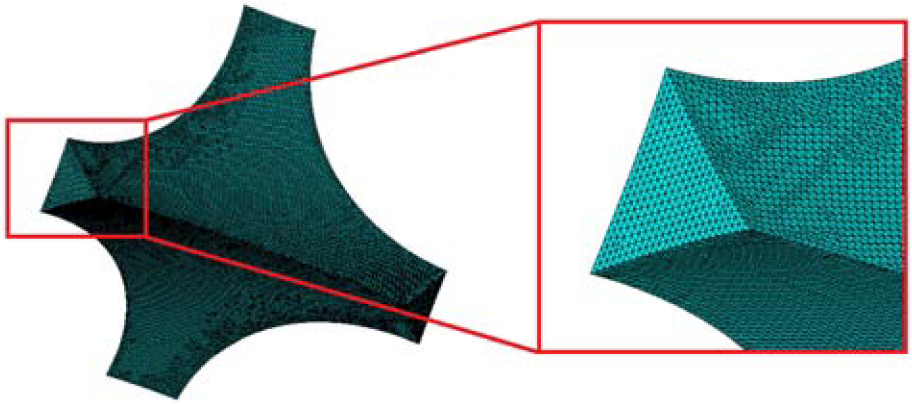

Fig. 21. Resulting mesh of a unit cell. On the right, detail at higher magnification.

For all the analysed cases, meshing is accomplished by using free meshing technique. Tetrahedral elements C3DR having one integration point and seeds spacing of 0.04 mm are used (Fig. 21). For all the symmetrical unit cells generated, the same following boundaries conditions are applied (Fig. 22). Three of the four struts are constrained so that all the displacement and rotations at the faces are suppressed (orange arrows). The remaining one undergoes uniaxial tensile stress equal to 2 MPa (pink arrows).

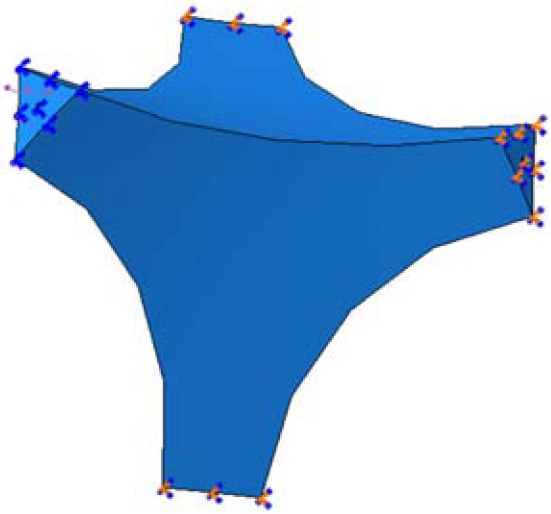

Fig. 22. Constraints and load applied to the designed unit cell.

4.5.2. Three-dimensional irregular strut

Perfectly symmetric struts cannot be observed in real foam structures. In order to determine the influence of cross-sectional irregularities, a strut having asymmetrical cross section and irregular shape has been created by sweeping technique. In particular, different parts constituting the struts were generated and assembled. Finally, random cuts were made on opposite sides of the part. The resulting strut shape with applied constraints and load are shown in Fig. 23a, b, respectively.

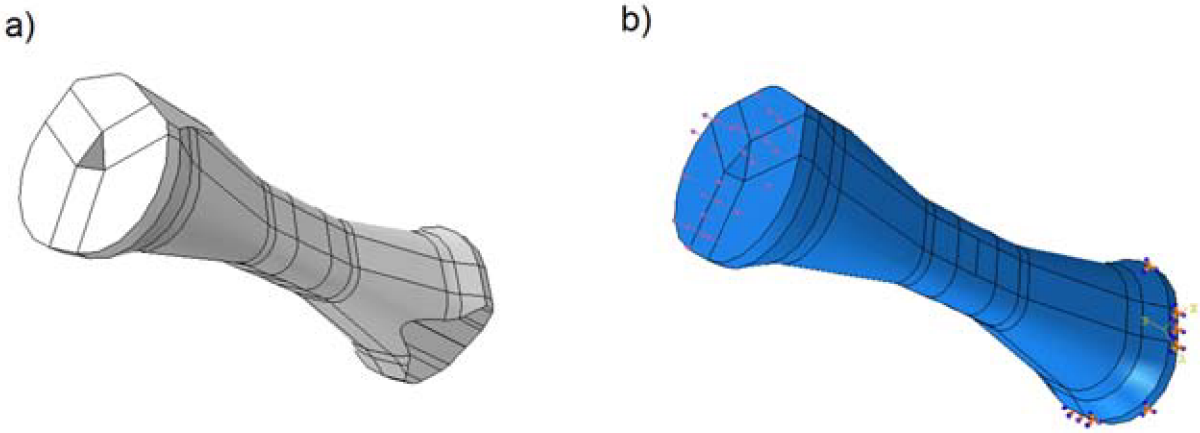

Fig. 23. Model of an irregular foam strut and boundary conditions used.

For the sake of simplicity and for the specificity of this study, the material constituting the foam struts has been assumed as isotropic and homogeneous and the presence of micro-defects within the struts was neglected. Struts are thus considered perfectly dense and having perfectly straight longitudinal axis. In Tab. 7 are shown values for Young modulus and Poisson ratio which has been used as inputs for the model [75] as well as the material behaviour and section type.

Material	*Section type*	*Mech. behaviour*	*Young modulus (GPa)*	*Poisson ratio (-)*
Bioglass	Solid, homogeneous	Isotropic, elastic	38	0.26

Tab. 7. Parameters used for FEM of node and irregular strut.

Concerning the single strut (right) a similar configuration is set, being one face constrained and the other one undergoing the same tensile stress. All the models here described were run in small deformation regime.

4.5.3. Two-dimensional cracked strut

Two different studies, evaluating the extent of coating infiltration and coating stiffness on K_I and σ_{22} were performed. The model of a simplified two-dimensional cracked strut having rectangular shape and loaded in plane stress conditions has been created. The strut width (W = 1 mm), strut height (h = 2 mm), crack length (a = 0.5 mm) and crack tip radius (ρ = 0.003 mm) were used. The width of the ligaments was defined as b = W-a. For all models, the displacement was driven in small deformation and elastic regime. The modelled strut part was loaded by displacement, being constrained at the lower side and undergoing a displacement Δy = +0.00017 mm along Y direction on the top side. For studying the influence of coating infiltration on K_I and σ_{yy}, five models were created: a non-coated strut; a strut with coating just on the surface, and struts with coating infiltrated until 1/3 the length of the crack, 2/3 the length of the crack and until the crack tip. For simplicity, the models were named as 1, 2, 3, 4 and 5 and they are represented in Fig. 24a. The stress intensity factor K_I was determined via Contour integral with the option no degeneracy of elements at the crack tip (crack tip elements were all hexagonal shape, Fig. 24b) and using the criterion of maximum tangential stress. The Young modulus (E_{PVA}) and the Poisson's ratio of PVA (υ_{PVA}) were set as 4.1 GPa [188] and 0.46 [189], respectively.

Then, the influence of E_{PVA} on K_I was also evaluated. For this purpose, a strut having same configuration as model 5 (PVA which penetrate until the crack tip) was considered and four simulations with increasing values of E_{PVA} (3, 5, 6 and 7 GPa) were run. These models were named as 6, 7, 8 and 9 respectively. Such values of E_{PVA} were chosen according to author's previous investigation [190], and they were meant to be representative of PVA and PVA/MFC composite films having increasing stiffness.

In order to experimentally validate the computed results, the parameters which determine the infiltration of a polymeric solution on a specific glass surface (i.e. wettability and viscosity) were

measured and correlated to the results obtained from mechanical testing of the corresponding polymer-scaffold system.

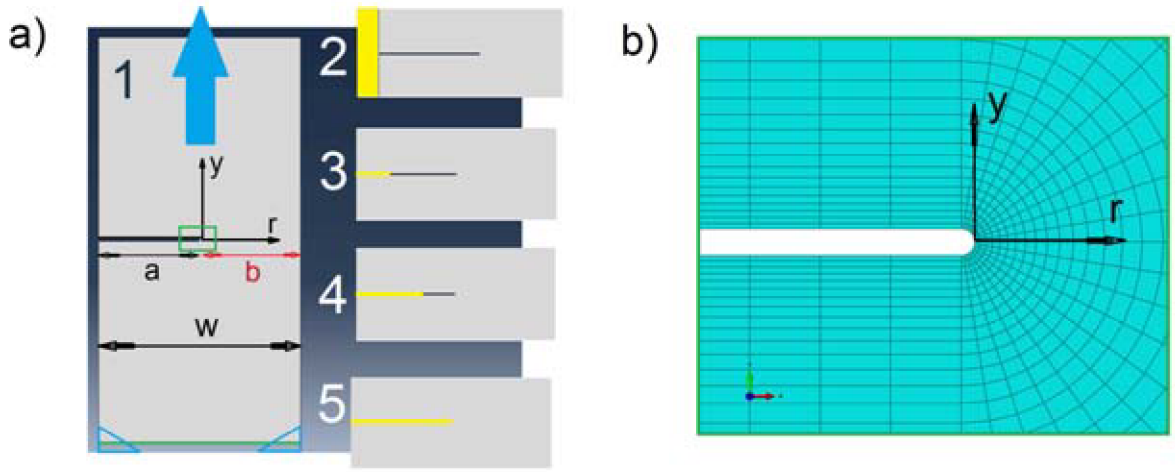

Fig. 24a) Definition of the FEM model used; b) and detail of the mesh at the crack tip.

The element type CPS4R, featuring a 4-node bilinear plane stress quadrilateral with reduced integration and hourglass control was chosen. The number of elements and nodes for each model ranged from 5020 to 5817 and from 5185 to 5999, respectively. The coating was assumed to be perfectly adhering on the strut and no debonding was considered. For each model, the computed σ_{yy} values near the crack tip were compared to the stress singularity function (Eq. 8). The resulting mesh in the proximity of the crack tip is shown in Fig. 23b. The whole computational work, from the definition of the parts to the outputs calculation has been accomplished by using the software Abaqus, v. 6-10.

5. Results

5.1. Scaffold structure

The structures of scaffolds obtained by ethanol-based slurry and water-based slurry are shown in Fig. 25a, b, respectively. In both case, the porosity of template (45 PPI), the number of dipping, and the slurry solid fraction were the same. The distribution of cell sizes and struts diameters was optimally described by a normal function. Mean cells size and struts thickness measured by image analysis of low magnification SEM micrographs resulted respectively as 500 µm and 50 µm. (Fig. 26a, b).

The increase of weight after coating was slightly higher for PVA-coated samples and decreased for PVA/MFC coated samples. In Tab. 8 are reported the average porosity values calculated for all the samples by Eq. 17 and 18. It is possible to observe that the decrease of porosity after the coating procedure is almost negligible. This indicates a homogenous distribution of coating along the struts surface.

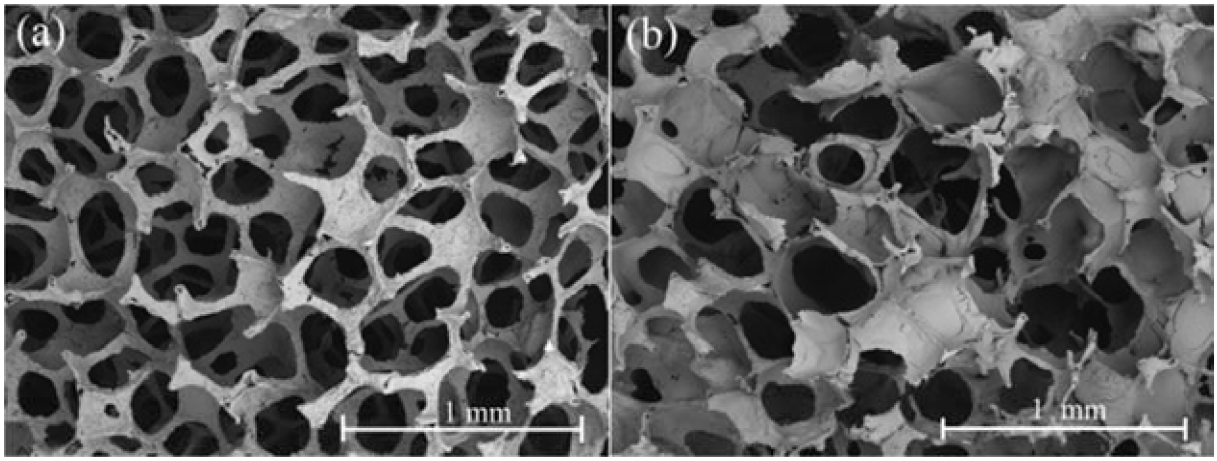

Fig. 25a) Comparison between scaffold microstructures obtained from an ethanol-based; b) and a water-based slurry having the same solid mass fraction.

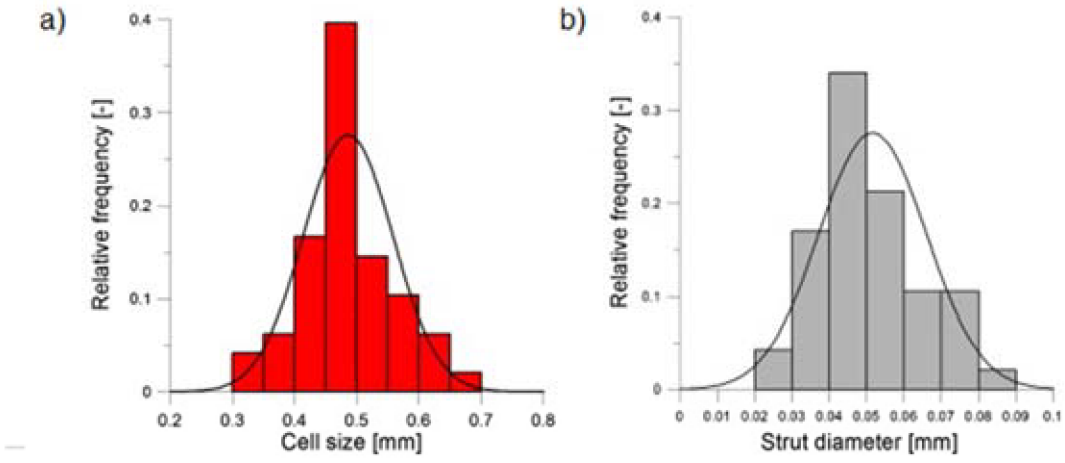

Fig. 26a) Pores size distribution and b) strut diameter distribution resulting from image analysis of tested specimens are shown.

No coating (%)	*PVA-coating (%)*	*PVA/5%MFC (%)*	*PVA/10%MFC (%)*
92.51 ± 0.50	90.22 ± 0.56	90.38 ± 1.49	91.39 ± 1.59

Tab. 8. Average porosity values for non-coated and coated scaffolds.

In Fig. 27 are shown three dimensional images reconstructed by µ-CT corresponding to PRE (a) and POST (b), respectively. The volumetric shrinkage occurring after sintering has been computed from the slices and resulted as nearly isotropic and equal to 26.6%.

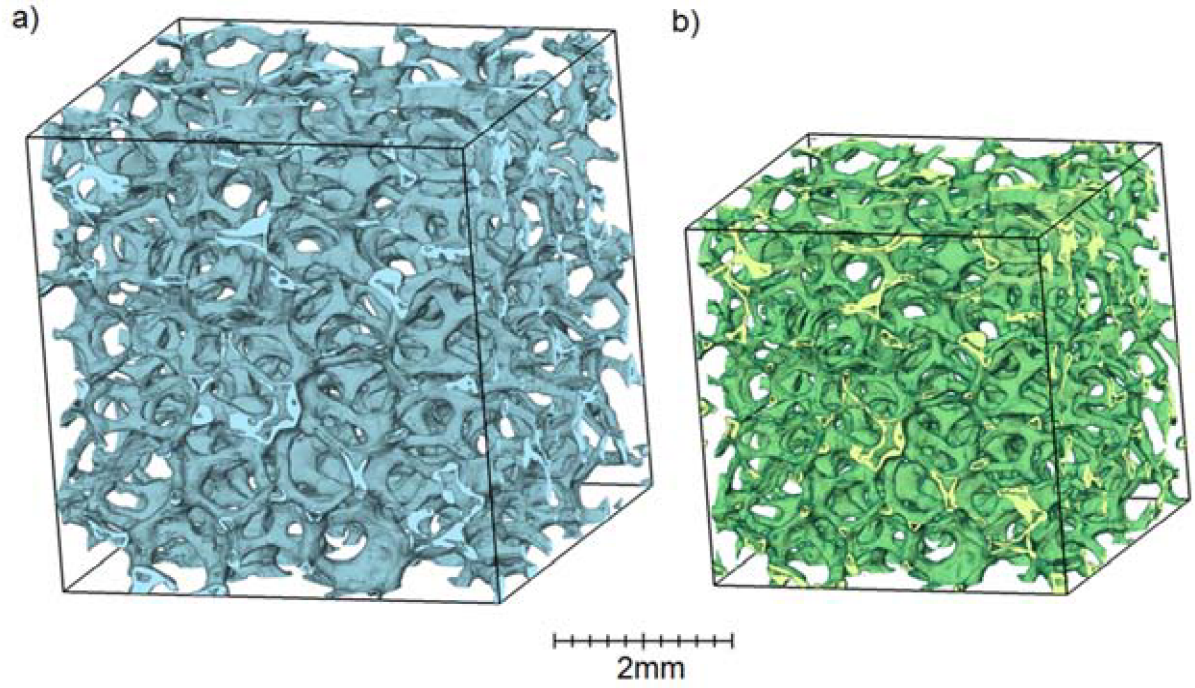

Fig. 27a) µ-CT scan of PU template coated by slurry (PRE); b) and the sintered scaffold (POST).

5.2. Microstructure and mechanical properties of Bulk Bioglass®

5.2.1. Sintering in conventional furnace

The morphology of a bulk Bioglass® samples sintered in conventional furnace can be observed in SEM micrographs shown in Fig. 28a. At least five different micrographs, taken in different regions were analysed by ImageJ and pores contour were analysed (Fig. 28b). The pore size distribution is accurately fitted by a lognormal function shown in Fig. 28c (Location Parameter = 2.55, Scale Parameter = 0.44, Goodness of fit = -0.87). The density measured by Archimedes' method was 2.53 ± 1.53 g/cm^3, which corresponds to 95.53 % of Bioglass® theoretical density. Density values measured by image analysis of SEM micrographs resulted equal to 94.35 %, being in good agreement with those obtained from Archimedes' method.

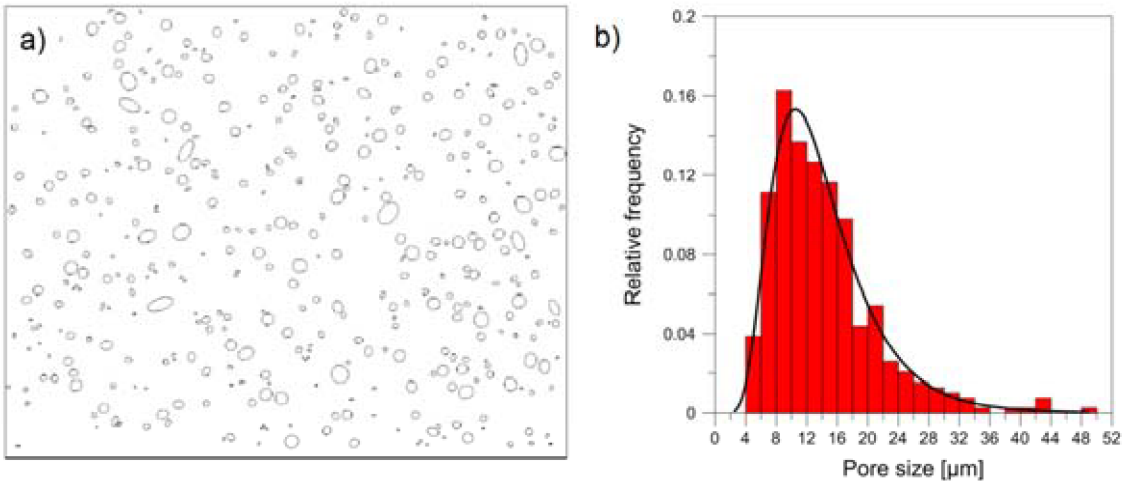

Fig. 28a) Pore analysis of pores of a SEM image by ImageJ; b) resulting pore size distribution.

The bending strength values of bulk Bioglass bars were ranging from 90.92 to 121.48 MPa. The distribution of strength values is shown in Fig. 29 and as it is visible, it is accurately fit by a three-parameter Weibull function (shape = 2,1088, scale=18.18, threshold=87,73 MPa).

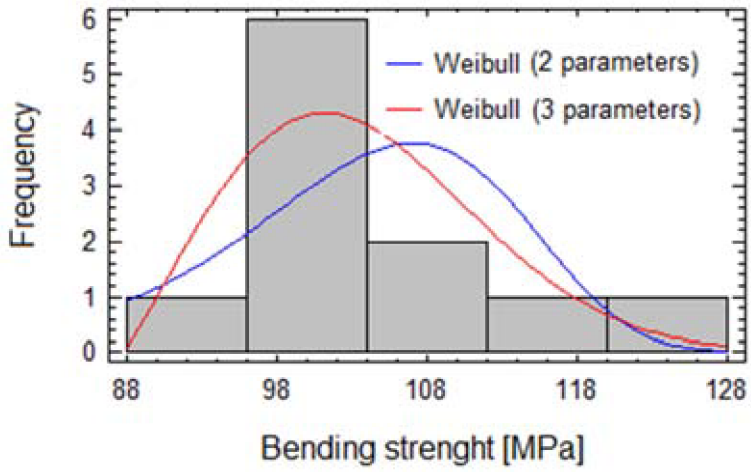

Fig. 29. Three-parameters Weibull distribution of bulk Bioglass® flexural strength.

The elastic modulus of bulk Bioglass® measured by resonance methods was equal to 89 GPa, which is consistent with Young's modulus of partially crystallized Bioglass reported by Peitl et al. [191].

Indentation fracture toughness and Vickers hardness were found equal to 0.27 ± 0.02 MPa·$m^{1/2}$ and 5.22 ± 0.25 GPa.

Fig. 30 shows the XRD diffraction pattern obtained. The main crystallization phase detected was combeite high ($Na_2CaSi_2O_6$, PDF-2: Ref. code 98-002-1475). The secondary phase detected is rhenanite ($NaCaPO_4$, PDF-2: Ref. code 01-076-1456).
Crystalline size of combeite was calculated by Scherrer equation resulted as 72.5 nm while rhenanite crystals were 57.83 nm.

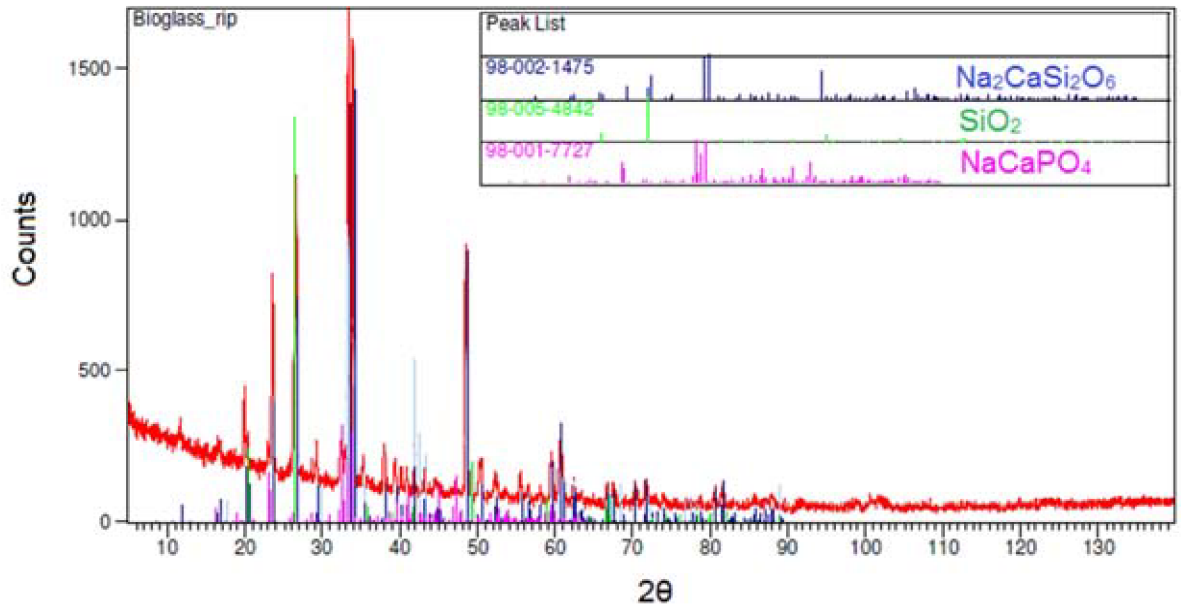

Fig. 30. XRD pattern of Bioglass® powder compact sintered at 1050°C for 1h.

5.2.2. Sintering of Bioglass® by SPS

For the first set of sample the processing parameters are summarized in Tab. 9. Density and Vickers hardness measurements revealed how the sintering performed in absence of pressure at 1050°C led to samples with superior density (close to the theoretical) and Vickers hardness in comparison with those pressure-assisted. For samples Pre1-2 density and indentation K_{IC} values were slightly higher than the values measured for Bioglass® sintered in furnace. On the contrary, sample Pre9 which was sintered at 550°C , exhibited remarkably lower density and K_{IC}.

Sample ID	*T (°C)*	*t (min)*	*P (MPa)*	*H. r. (C/min)*	d_{rel} *(%)*	*HV 0.2 (–)*	K_{IC} *(MPa m$^{-1/2}$)*
Pre1	600	5	60	100	97.41	406.29 ± 18.18	0.47
Pre2	600	5	70	100	97.78	471.29 ± 20.75	0.49
Pre9	550	5	70	100	96.67	361.34 ± 21.42	0.25
PL6	1050	30	0	100	100.00	548.84 ± 38.51	-
PL8	1050	60	0	100	99.26	553.43 ± 32.95	-

Tab. 9. First set of SPS samples with related processing parameters and H_V, K_{IC} measured values.

The indentation depths of PL6 and PL8 resulted 11% lower than Pre1-2-9. For these samples the measurement of indentation K_{IC} was not possible because in most cases no cracks could be observed in most of the indents. The total deformation energy (E_t) resulted lower for PL6 and PL8 samples, which exhibited as well higher indentation elastic modulus (E_{IT}) values. Characteristic force vs. indentation depth curves obtained for a Pre1 and PL6 samples are shown in Fig. 31a. For

those, elastic and plastic work of deformations calculated for each indent, are summarized in Fig. 31b.

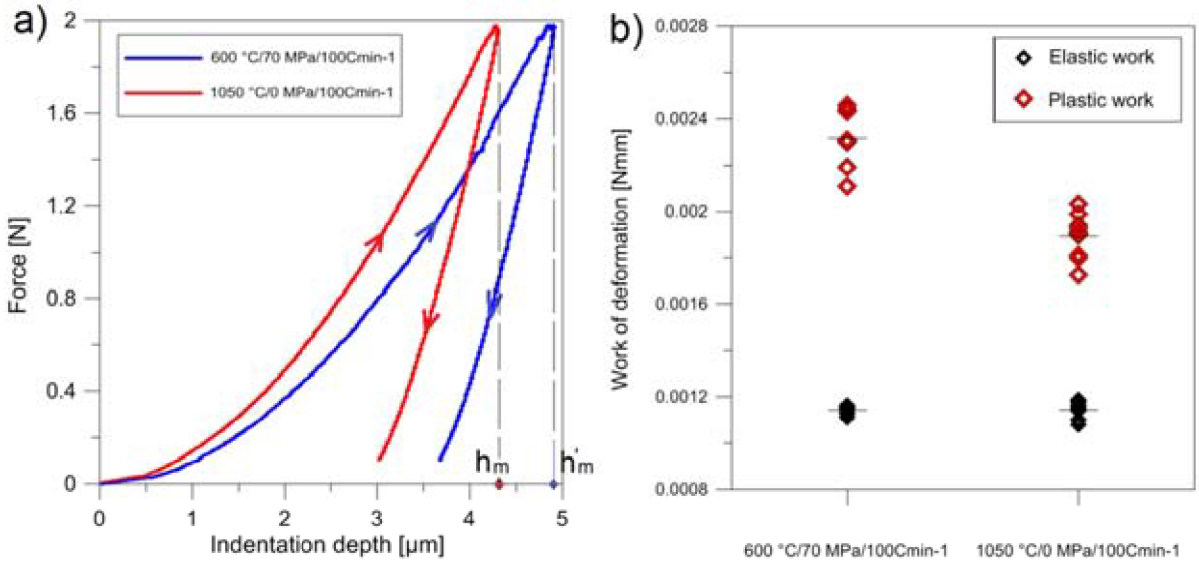

Fig. 31a) Force-displacement curves for Pre1 and PL6 samples. b) Elastic and plastic work of deformation measured for each set of samples.

In Tab. 10, average values h_m, E_e, E_a, and E_{IT} values for Pre2 and PL8 are summarized.

Sample ID	h_m *(µm)*	E_e *(Nmm)*	E_a *(Nmm)*	E_t *(Nmm)*	β *(-)*	E_{IT} *(GPa)*
Pre2	4.85±0.06	0.0011	0.0023	0.0034	0.33	81.60 ± 2.39
PL8	4.32±0.09	0.0011	0.0018	0.0030	0.37	97.41± 3.57

Tab. 10. Indentation depths, elastic, plastic works of deformation and indentation elastic modulus for preliminary samples for samples Pre2 and PL8.

XRD analysis of Pre1-2-9 samples revealed the crystallization of $Na_2CaSi_2O_6$, in agreement with Grasso et al. (Fig. 32).

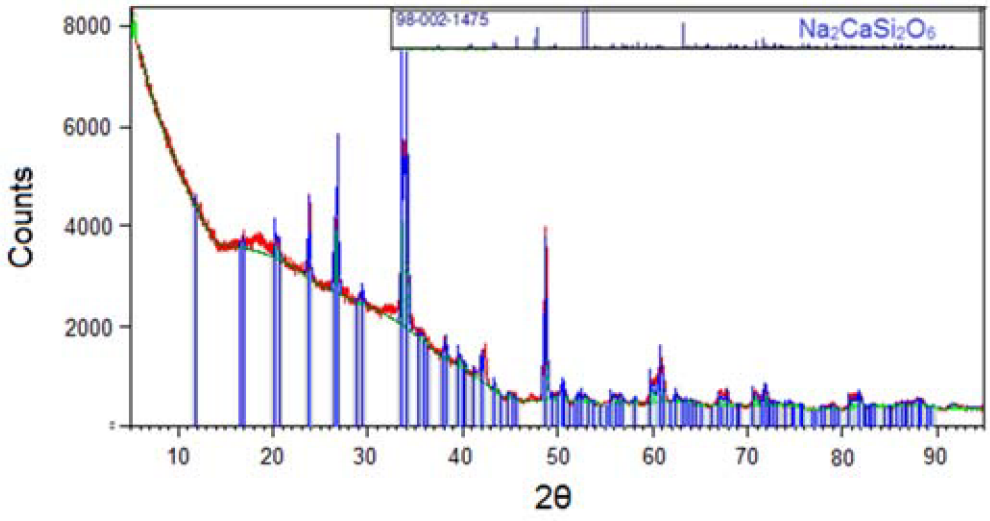

Fig. 32. XRD plot of a Pre2 sample.

The elastic modulus measured of Pre1-2-9 samples was measured by resonance method and resulted as ranging from 82 to 84 GPa, being consistent with the indentation elastic modulus E_{IT}.
In Tab. 11 are summarized the Young's modulus for Bioglass® sintered in oven, Pre2 and PL8 measured by resonance technique.

Sintering conditions	Oven	Pre2	PL8
Young's modulus (GPa)	89	82	109

Tab. 11. Young's modulus values measured by Grindosonic.

Based on these results, the second set of samples was sintered without the assistance of mechanical pressure. Three samples were produced by using heating rate, holding time and peak temperature equal to 100°C /min, 30 min and 1050°C , respectively (distinguished purple row, Tab. 12). Two samples were then produced by using a considerably higher heating rate of 300°C /min (red row in Tab. 12). The repetition of sintering with the same processing conditions was made in order to verify the reproducibility of the process. Sintering at 1000°C (yellow row in Tab) resulted in samples exhibiting lower density and lower K_{IC}, indicating that such holding temperature is not sufficient for the achievement of a dense microstructure. For this reason this conditions have not been further investigated. For, one sample, the holding time was set as 60 min. As it is visible in Tab. 12, all the samples sintered at 1050° C exhibited K_{IC} values ranging from 1.0 to 1.4 $MPa \cdot m^{-1/2}$, three to four times higher than K_{IC} values measured for Bioglass® sintered in oven. Those samples whose densities were close to the theoretical were thus considered for XRD analysis. XRD diffraction patterns obtained for PB01 PB02, PB08 and Bioglass® sintered by conventional method are shown in Fig. 33.

Sample ID	*Hr (°C/min)*	*Ts (°C)*	*t (min)*	*P (MPa)*	*d (g/cm^3)*	*d_{rel} (%)*	*K_{IC} (Chevron) ($MPa \cdot m^{-1/2}$)*
PB01	100	1050	30	vacuum	2.7	100.00	1.05 ± 0.05
PB02	300	1050	30	vacuum	2.68	99.25	1.23 ± 0.21
PB03	100	1000	20	vacuum	2.64	97.77	0.89 ± 0.03
PB05	300	1000	30	vacuum	2.65	98.14	0.84 ± 0.16
PB06	100	1050	30	vacuum	2.68	99.25	1.01 ± 0.17
PB07	100	1050	30	vacuum	2.70	100.00	1.4 ± 0.11
PB08	100	1050	60	vacuum	2.67	99.01	1.5 ± 0.10

Tab. 12. Second set of SPS samples with related processing parameters and, K_{IC} values.

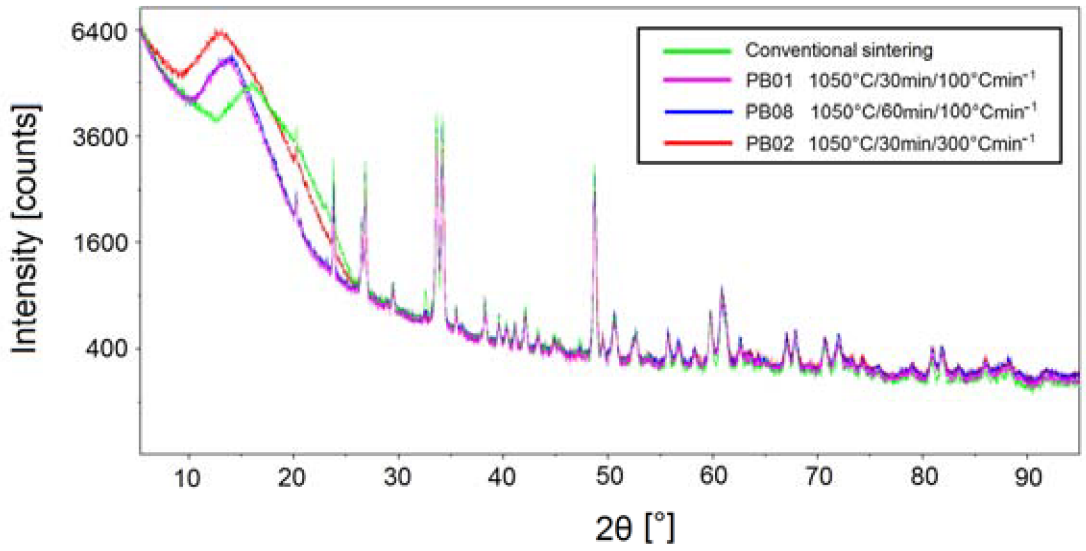

Fig. 33. XRD diffraction patterns of Bioglass® sintered in furnace (green), at 1050°C /30min/100°C ·min^{-1} (purple), 1050°C /60min/100°C ·min^{-1} (blue) and 1050°C /30min/300°C ·min^{-1} (red).

The detected crystalline phases with related weight percentage and crystalline size are summarized in Tab. 13.

Sample	*$Na_2CaSi_2O_6$ (% wt.)*	*Crystall. size (Å)*	*$NaCa(PO_4)$ (% wt.)*	*Crystall. size (Å)*
Conventional sintering	89.9	725.7	10.1	578.3
600°C /30min/100°C min^{-1}	100	263.4	-	-
1050°C /30min/100°C min^{-1}	98.4	458.5	1.6	356.2
1050°C /60min/100°C min^{-1}	97.7	544.6	2.3	525.2
1050°C /30min/300°C min^{-1}	99.6	554.7	0.4	164.8

Tab. 13. Summary of crystalline phases detected in preliminary samples with related weight fractions.

5.3. Bioglass® scaffolds coated with PVA/MFC composite coating

5.3.1. Foams produced from 60 PPI template

Initial tensile test were carried out on 60 PPI foams for comparison with data from Ref. [182]. A characteristic tensile load curve for uncoated specimens is shown in Fig. 34a. The coated samples exhibit a remarkably different mechanical behaviour in comparison to non-coated ones. In Fig. 34b, three tensile load curves respectively representing non-coated (red curve), PDLLA-coated (dashed curve, Ref. [182]), and PVA/MFC-coated Bioglass® scaffolds (black curve) are shown. Non-coated samples turn out to be extremely brittle and weak. For coated samples, pop-in peaks are not observed during the first stage of load increase. First fracture events take place only at a remarkably higher load in comparison with non-coated samples and they are followed by a less drastic drop of

load. After this point, a plateau stage can be observed, corresponding to toughening mechanisms enabled by deformation of the polymer coating.

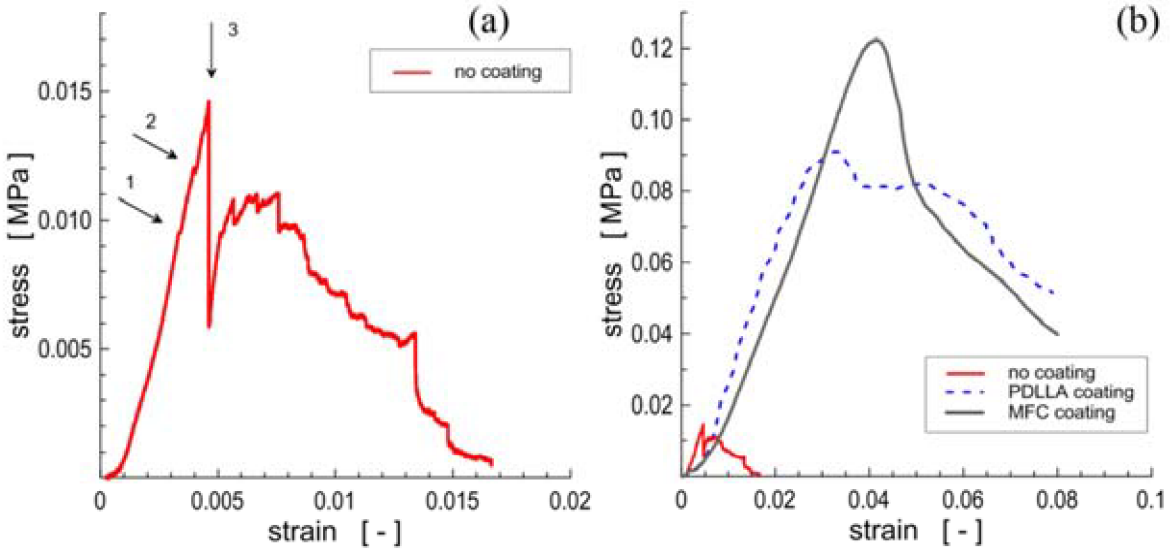

Fig. 34a) Stress vs. strain curves from tensile strength test for uncoated samples b) comparison with PDLLA-coated and PVA/MFC-coated samples (b).

The average tensile strength value for uncoated scaffolds is 0.011 ± 0.004 MPa. Samples coated by PVA/MFC coating exhibit more than 10 fold increase of tensile strength compared to non-coated samples, reaching an average tensile strength of 0.10 ± 0.02 MPa (from 4 samples measured). Moreover, about 40% increase of tensile strength compared to PDLLA-coated samples is achieved (the average tensile strength of PDLLA-coated samples is 0.07 ± 0.02 MPa [182]). Tensile strength values are summarized in Fig. 35.

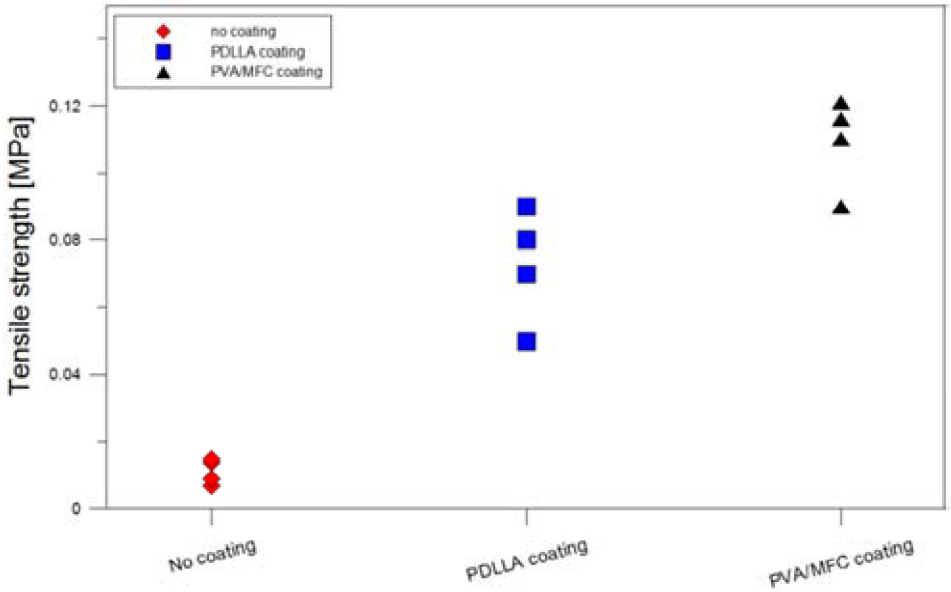

Fig. 35. Tensile strength comparison between uncoated, PDLLA-coated [182] and PVA/MFC-coated Bioglass® foam (60 PPI template).

Fig. 36 shows a fractured strut coated by PVA/MFC. The coating appears to be homogeneously distributed along the strut surface, forming a continuous thin film (thickness can be estimated in the order of few microns) without reducing the porosity degree of the whole structure).

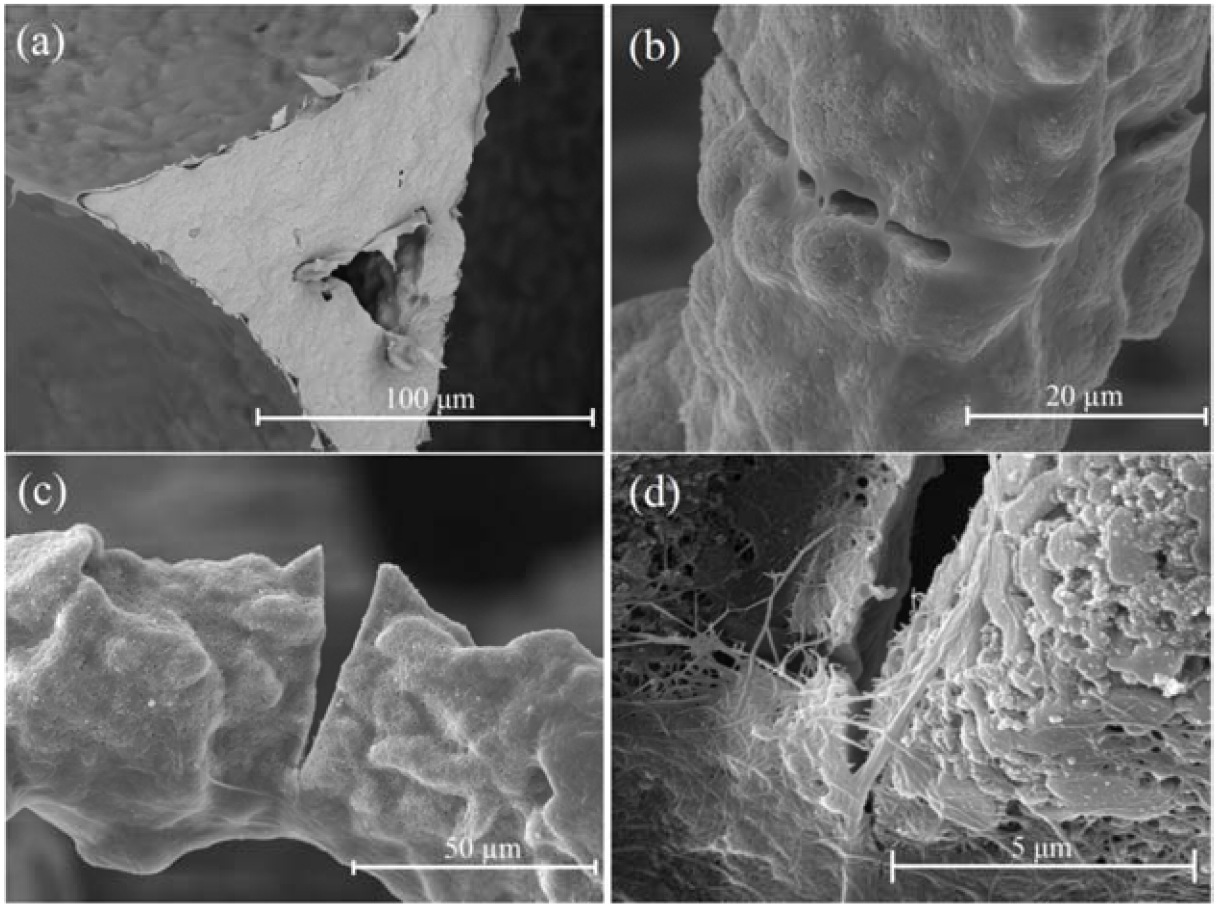

Fig. 36. Fracture morphology of broken struts of PVA/MFC-coated samples of a 60 PPI foam.

5.3.2. Foams produced from 45 PPI template

5.3.2.1. Compressive tests

A more comprehensive set of experiments was conducted on 45 PPI foam. Four characteristic compressive stress-strain curves for non-coated, PVA-coated, PVA/5%MFC-coated and PVA/10%MFC-coated scaffolds, respectively, are shown in Fig. 37a. First fracture events (most probably struts fracture) are recorded as the applied stress reaches approximately 0.05 MPa. Beyond this point, the deformation proceeds without further increase of load and progressive crushing of all the struts occurs up to the densification stage. The compressive strength for uncoated scaffolds was 0.053 ± 0.010 MPa whereas PVA-coated samples reach an average value of 0.26 ± 0.04 MPa. The addition of 5 wt. % of MFC fibres to the coating lead to a further increase of the compressive strength up to 0.69 ± 0.10 MPa. As the concentration of MFC fibres was doubled to 10 wt.%, the compressive strength of scaffolds decreased to 0.37 ± 0.07 MPa. Results are summarized in Fig. 37b. Therefore, further addition of fibres above 5 wt. % seems to have a detrimental effect on the strengthening action of the coating. This behaviour could be ascribed to a less homogenous

distribution of the MFC fibres, as their concentration increase. Also the filling of internal and surface struts defects could be worse for 10 wt. % MFC fibrils in PVA matrix comparing to 5 wt. % concentration because the viscosity increase due to the presence of fibres.

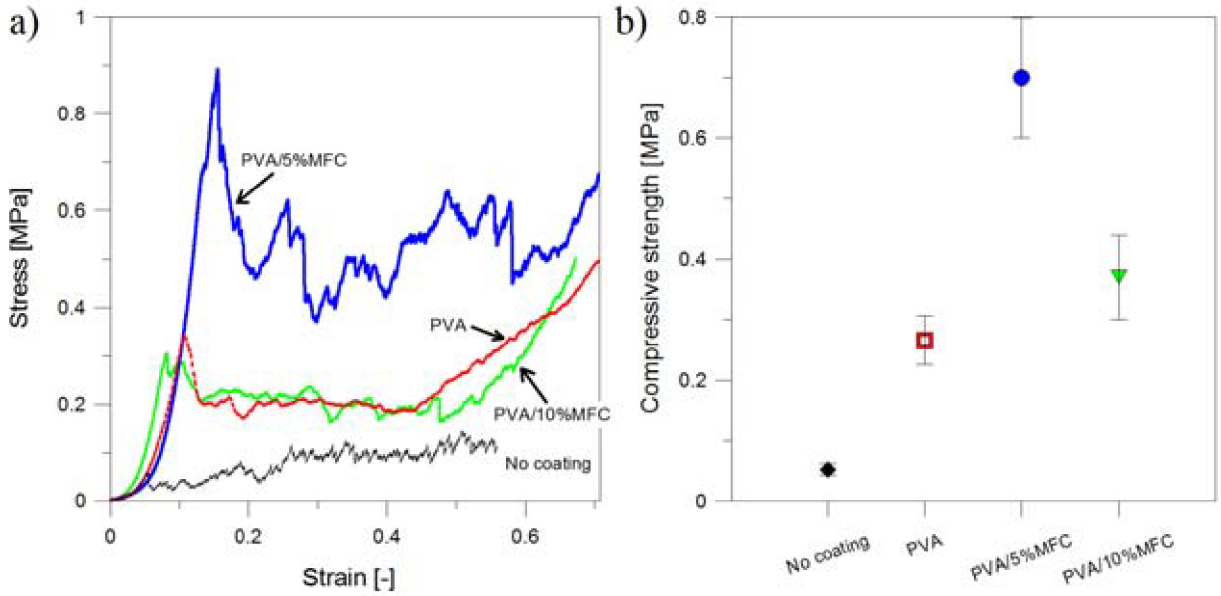

Fig. 37a) Characteristic stress-strain curves from compressive test for non-coated, PVA-coated, PVA/5%MFC-coated and PVA/10%MFC coated scaffolds; b) Average compressive strength values of each set of samples with related scatters are summarized.

5.3.2.2. Tensile tests

Characteristic tensile stress–strain curves for non-coated, PVA-coated, PVA/5%MFC-coated and PVA/10%MFC-coated scaffolds are shown in Fig. 38a. In the case of non-coated samples, the increase of load causes fracture of the first suitably oriented struts. However at this stage the load might be further increased until critical damage accumulation, i.e. when the critical loss of the bearing resistance of the struts is reached. This stage corresponds to simultaneous fracture of several struts/cells and sudden unstable drop of load. At this point, some few undamaged struts still exist and the load can be again increased until the onset of generalized fracture of the remaining cross-section occurs. Unlike uncoated scaffolds, the coated ones do not exhibit any pop-in peaks at the initial stage of load increase and the first fracture events take place only at remarkably higher load in comparison with the non-coated samples.

For each set, seven samples were tested and average values with related scatters are reported in Fig. 38b. The average tensile strength value for uncoated scaffolds has been found to be 0.014 ± 0.0031 MPa. Samples coated by PVA exhibited more than 10 fold increase of tensile strength compared to non-coated samples, reaching an average value of 0.196 ± 0.009 MPa. The addition of 5 wt. % of MFC fibres into the coating led to a further increase up to 0.271 ± 0.012 MPa. However, the highest values were recorded for PVA/10%MFC-coated samples, whose average tensile strength reached 0.335 ± 0.066 MPa. On the other hand, these samples exhibited larger scatter of results.

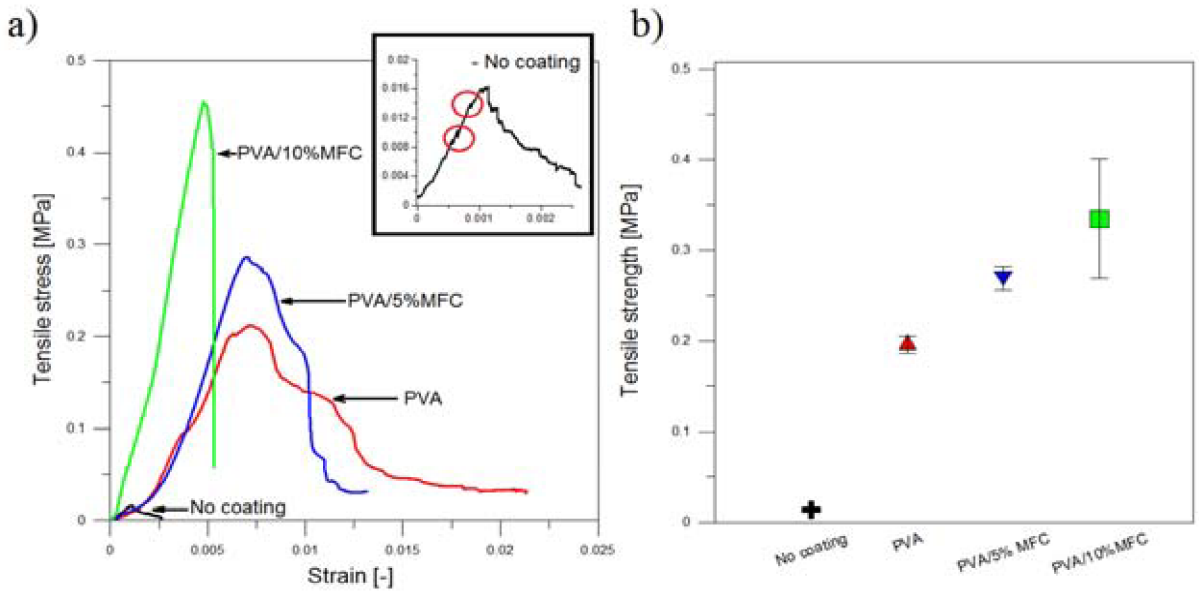

Fig. 38a) Characteristic stress–strain curves from tensile test for non-coated, PVA-coated, PVA/5%MFC-coated and PVA/10%MFC coated scaffolds, b) average tensile strength values of each set of samples with related scatters are summarized.

SEM images indicate that fibres are effective as load-bearing elements (Fig. 39). It is worth to point out that all the micrographs refer to specimens which have been deformed beyond their highest stress peak, in order to observe toughening mechanisms occurring in the plateau region. The evaluation of coating adhesion strength will be required to determine how the debonding of the coating might contribute to the overall toughening.

The occurrence of the crack bridging mechanism is evident in Fig. 39b–e and f, involving both the MFC and PVA. The fibrils spatial distribution along the crack front appears as optimal for the reinforcement purpose either considering the energy dissipation, arising from the fracture of single fibrils and the crack opening limitation effect. There is a larger pack of MFC fibrils in the PVA matrix bridging the crack in the strut shown in Fig. 39e, which can be taken as an evidence of non-homogeneously distributed MFC fibrils in the coating. Despite that, fibrils can still supply effective reinforcing effect mainly in the final stage of specimen elongation. Fig. 39f shows a crack bridging carried out by MFC fibrils only, without extensive assistance of the PVA matrix.

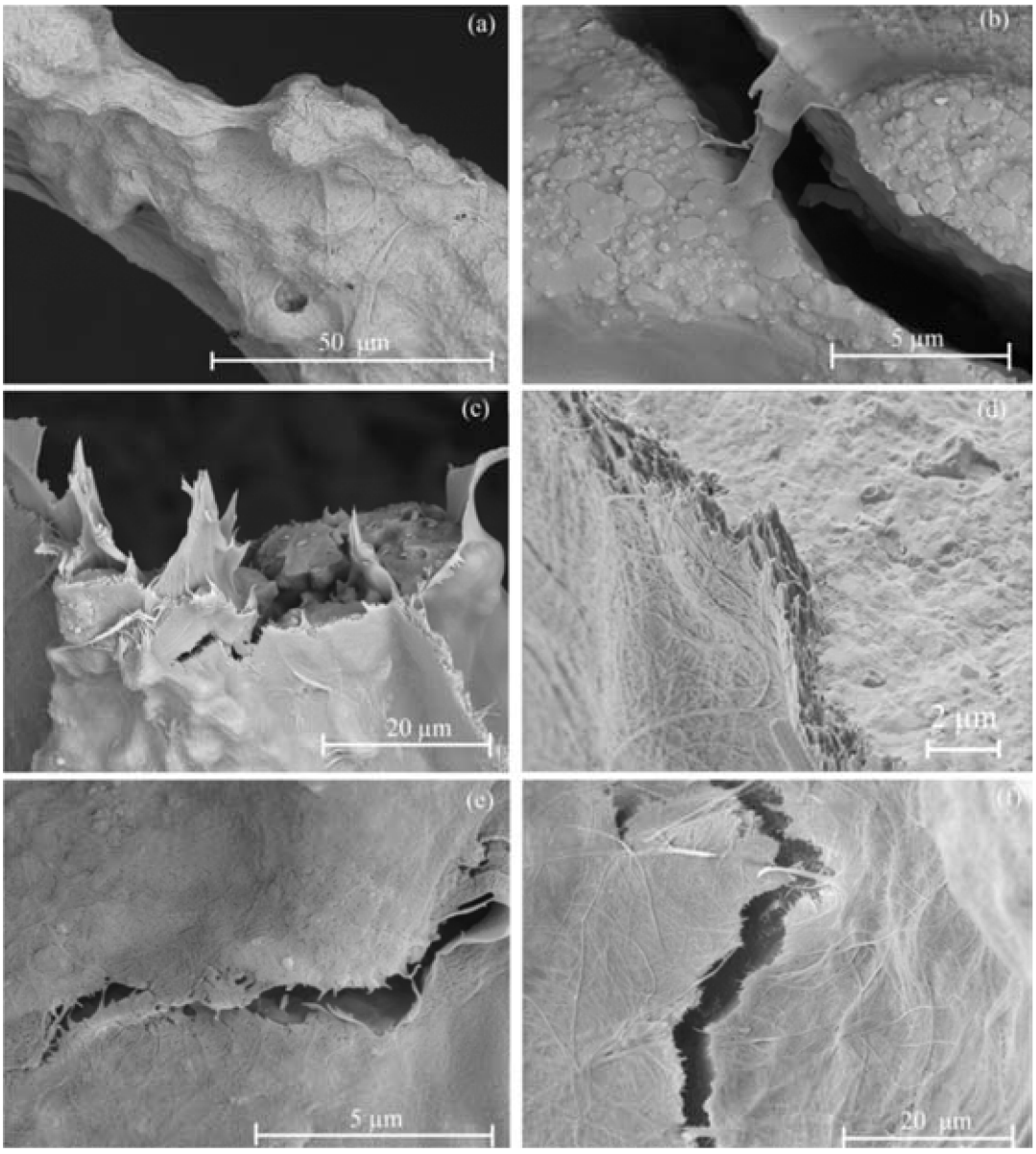

Fig. 39a) Fracture morphology of broken struts of coated samples: PVA/5%MFC coated strut; b) detail of the PVA/MFC bridging in a PVA/5%MFC-coated specimen; c) struts fracture of a PVA/10%MFC-coated specimen; d) detail of the coating at higher magnification; e) bridging by the PVA/MFC pack in PVA/5%MFC-coated specimen and f) bridging by MFC fibrils only PVA/10%MFC-coated specimen.

Similarly to scaffolds derived from 60 PPI templates, the coatings appeared as homogeneously distributed along the strut surface, forming a continuous thin film without reducing the porosity degree of the whole structure. This would indicate that the PVA/MFC mixture has suitable viscosity and wettability for coating this type of Bioglass®-derived scaffolds. MFC fibres form an intricate network, intimately bonded to the strut surface by the PVA. The PVA component seems to provide sufficient adhesion to the strut surface which is necessary to ensure load transfer from the struts to the MFC fibres. This effect should be responsible for the further increase of the mechanical strength recorded of PVA/MFC-coated scaffolds. It is also worth noticing how the polymeric solution was able to infiltrate into the strut inner cavity, probably through a number of pre-existing cracks.

5.3.3. Elastic modulus of foams

In Tab. 6, the values of elastic modulus measured by different techniques for uncoated, PVA–coated, PVA/5%MFC and PVA/10%MFC scaffolds are reported for the sake of comparison. For uncoated samples, the elastic modulus was estimated by using GA model (Eq. 10) and by calculating the slope of the elastic part of stress-strain curves. However, in the latter case, the values appear to be highly scattered (1 order of magnitude) and cannot be considered as reliable. On the other hand, coated specimens exhibited comparable values from both techniques. As expected, those calculated from the slope resulted as slightly lower, in agreement with the fact that the slope–approach generally underestimates the real stiffness [180]. For the prediction of elastic modulus by GA model, E_s has been set equal to 89 GPa (section 5.2.1). Nevertheless it is possible to see that the presence of coating does not influence the stiffness of the structure, in agreement with Peroglio et al. [99].

Method	*No coating*	*PVA*	*PVA/5%MFC*	*PVA/10%MFC*
Slope of linear part	0.03 – 0.41	0.24	0.23	0.26
Resonance	-	0.25	0.30	0.29
GA model (Eq.10)	0.21	-	-	-

Tab. 14. Elastic modulus values (GPa) of uncoated and coated scaffolds, measured by different methods.

5.3.4. Mechanical properties of PVA/MFC composite films

The results obtained from tensile tests on PVA/MFC stripes provide a better understanding of the mechanical behaviour of coated scaffolds. The tensile strength and modulus of pure PVA stripes resulted as 66.26 ± 5.91 MPa and 4.15 ± 0.33 GPa, respectively. The addition of 5% wt. and 10% wt. of MFC fibres cause depletion of elastic modulus and strength as the precursor mixtures are stirred for 24 h. By increasing the mixing time of PVA/MFC mixture up to 48 h, the MFC fibres seems to become effective as a reinforcing element and noticeable enhancement of strength and modulus is achieved. In fact for PVA/10%MFC specimens stirred for 48h, the strength and elastic modulus reach respectively 109.27 ± 8.11 MPa and 6.42 ± 0.27 GPa. The strength and elastic modulus of PVA/10%MFC specimens stirred for 48 h reach 109.27 ± 8.11 MPa and 6.42 ± 0.27 GPa, respectively. Results are summarized in Fig. 40.

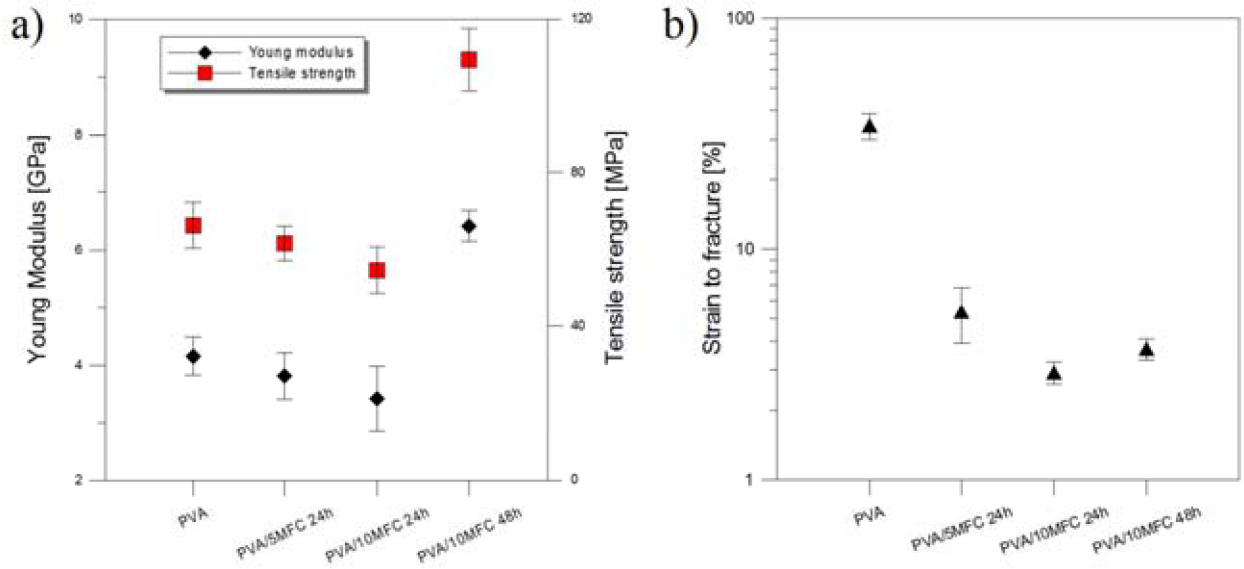

Fig. 40. Average Young's modulus, tensile strength (a) and strain to elongation (c) of PVA, PVA/5%MFC, PVA/10%MFC (stirred for 24 h) and PVA/10%MFC (stirred for 48 h) films, with related scatters are summarized.

For all the composite stripes, the strain to fracture turned out to be remarkably lower than the neat PVA stripes and progressively decrease as concentration of MFC increase (Fig. 40b). This trend is consistent with the reduction of the plateau regions recorded during tensile tests of PVA/10%MFC coated scaffolds and it is in agreement with the percolation theory of MFC-reinforced composites reported by Zimmermann et al. [132].

5.4. FEM modelling

5.4.1. The influence of cavity derived from replica process

Distribution of von Mises stresses in the studied models of unit cell and on constrained end of the struts is shown in Fig. 41 and 43, respectively. As the dimensions of the cavity increases, the stress is re-distributed closely to the external surface of the strut. It can be noted that the cavity does not cause significant concentration of the stress in strut. The stress distributions for full strut (O) and for strut with the smallest cavity (O-S1) are nearly the same. In case of O-S1 and O-S3 there is higher gradient of the stress along the wall of the strut, but the values of the stresses do not exceed the level of stress achieved in two previous cases.

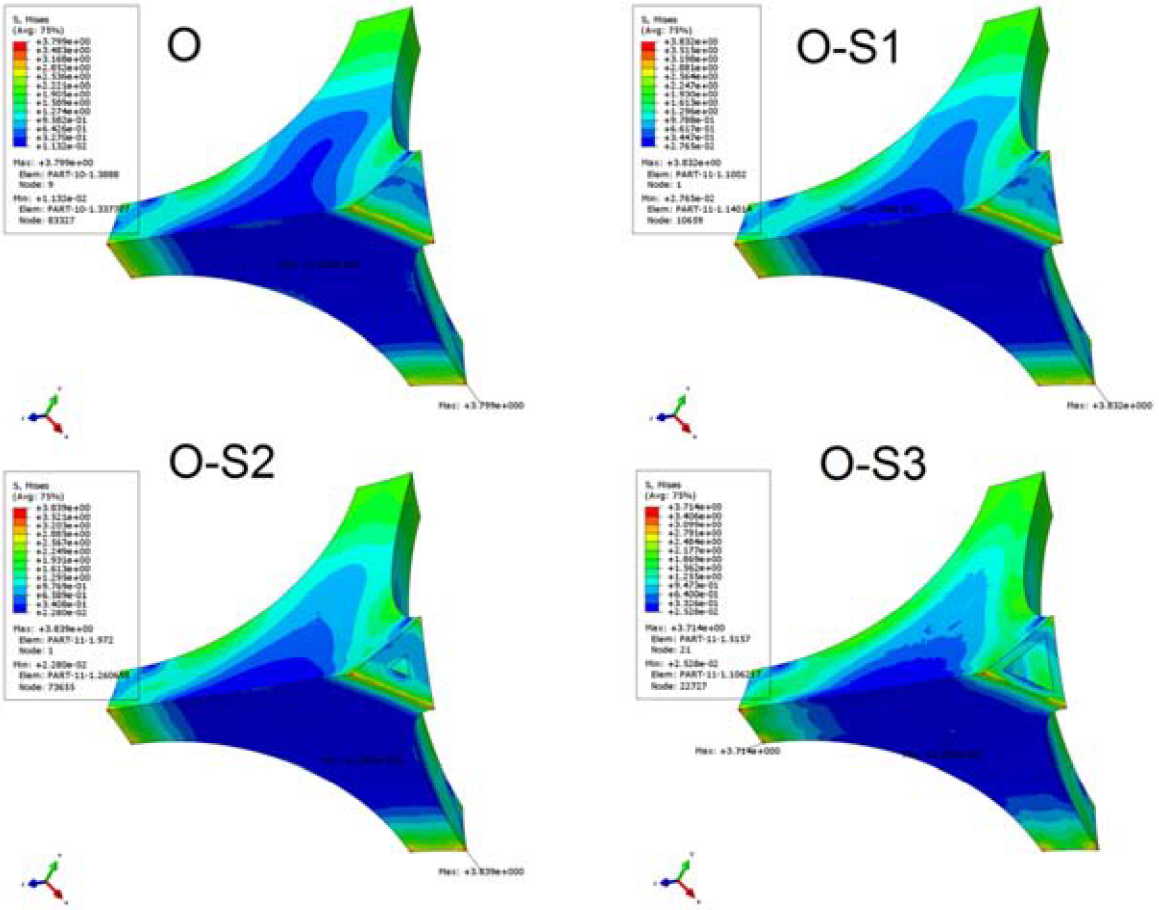

Fig. 41. Von Mises stress distributions in the four unit cells.

The effect of re-distribution of the stress can be also visible on the graph in Fig. 42, which shows the values of von Mises stress along path 1 (red line) and 2 (yellow line).

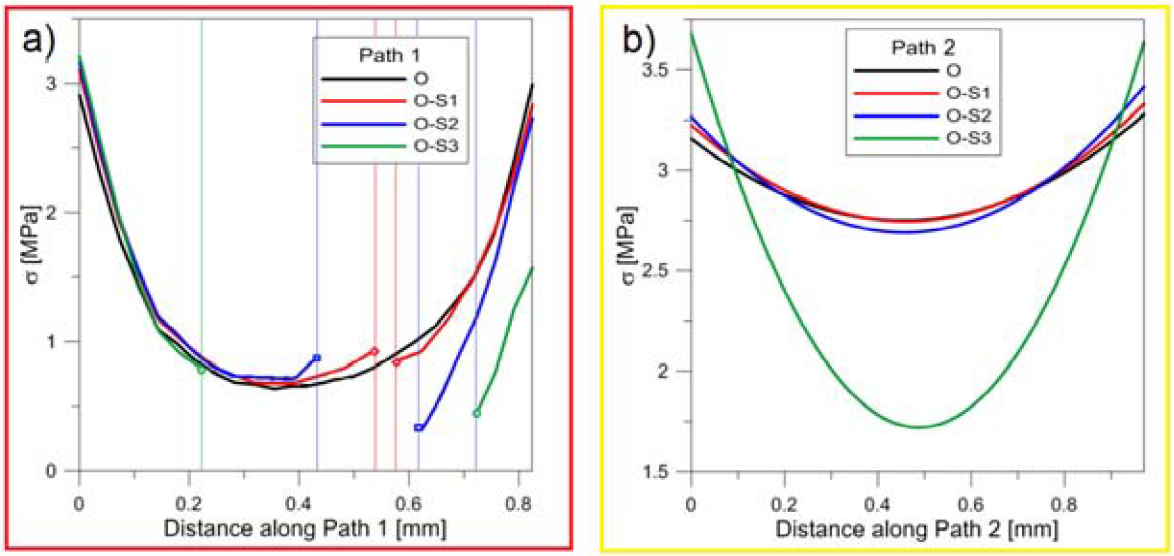

Fig. 42. Von-Mises stresses plotted along path 1 (a) and 2 (b).

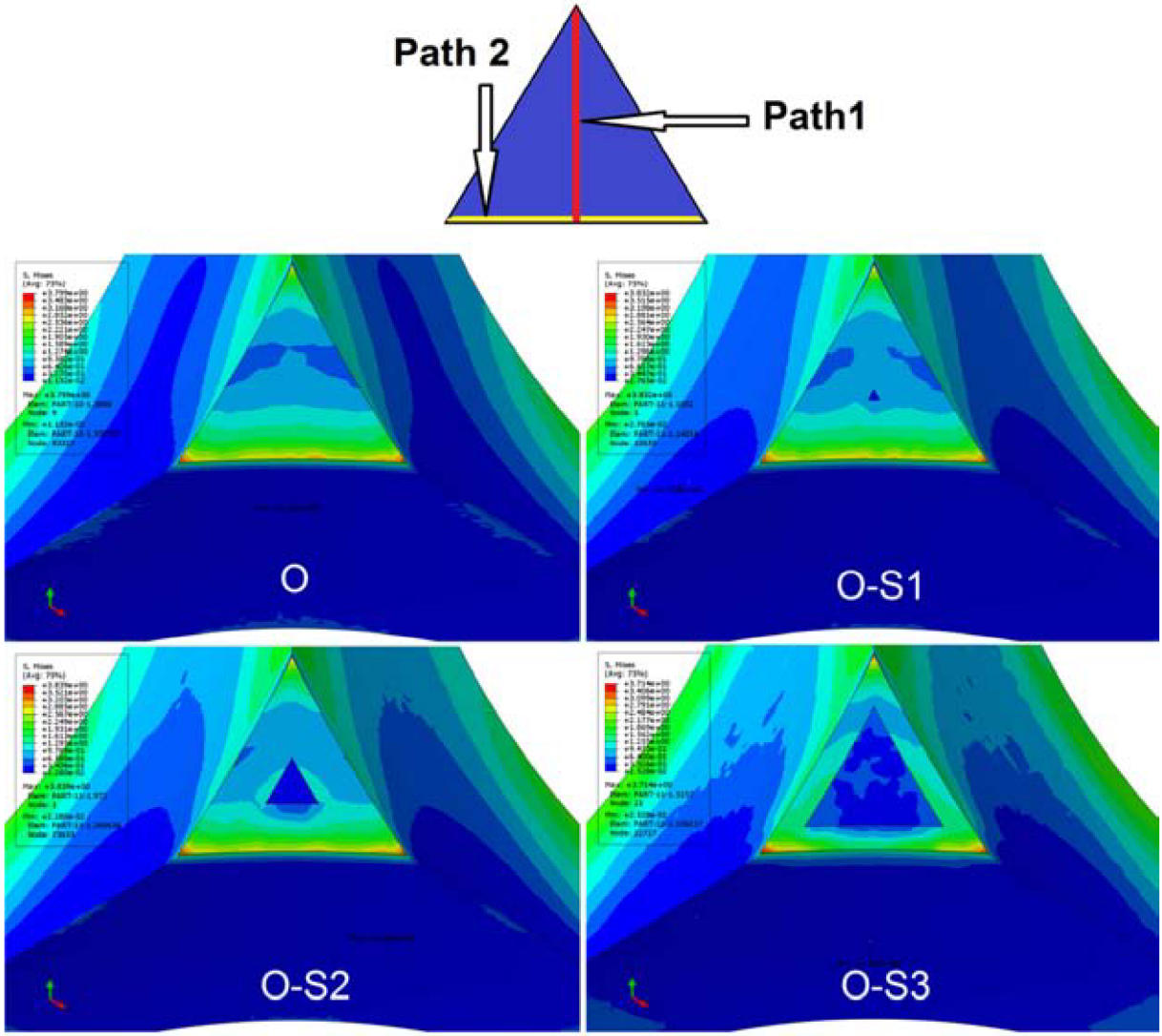

Fig. 43. Von Mises stress distribution on constrained unit cell.

5.4.2. Three-dimensional irregular strut

Because of asymmetric shape, the strut undergoes bending deformation in tensile loading (Fig. 44). Deviation from symmetry results in change of strut's stiffness along the longitudinal axis. Since pressure loading condition and no constrained displacement was set, the deformation occurs earlier in the least stiff part, causing the strut bending. Maximum strains take place on the surface of the strut at its mid-length because of the arising of higher bending forces and maximum cross section reduction. As a consequence, the highest Von Mises stresses originate as well in the same area. Even when the applied loading has the same level as in the previous simulation (pressure 2 MPa), von Mises stresses reach nearly 14 MPa.

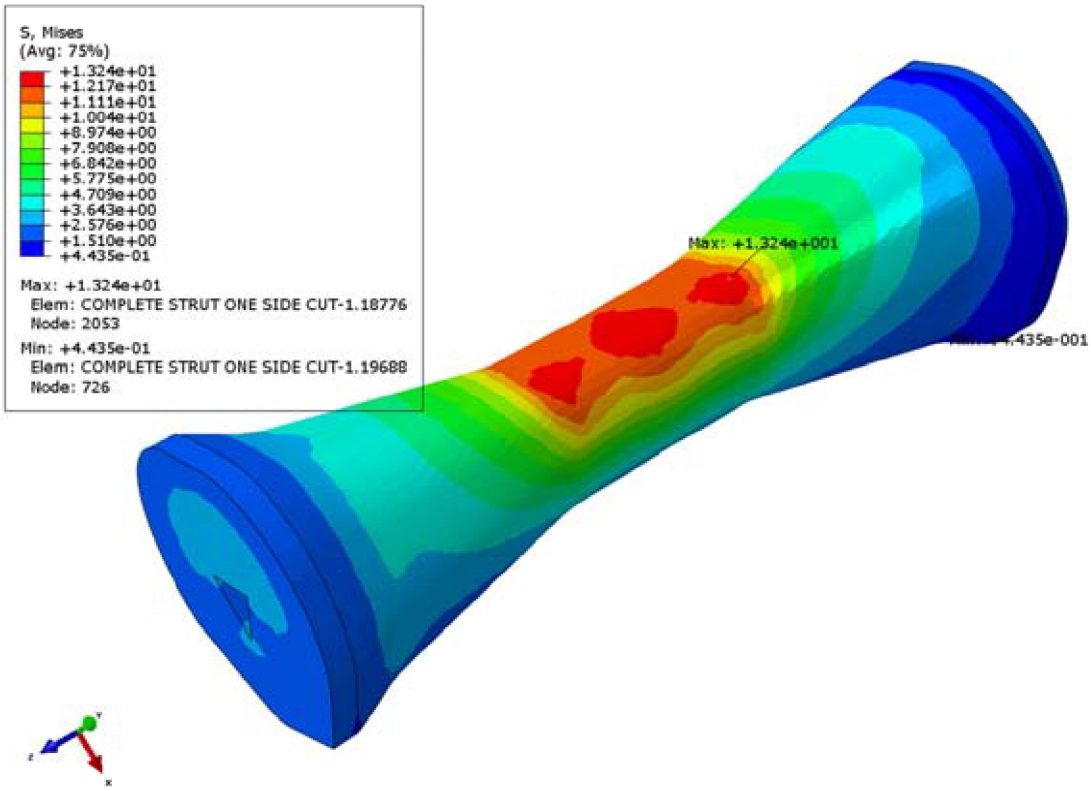

Fig. 44. Von-Mises stress distribution after deformation.

5.4.3. Two-dimensional cracked strut infiltrated by coating

The results obtained from FEM are summarized in Tab. 15. The distance from the crack tip, at which the singularity function fits the computed σ_{yy} distribution, has been defined as r_v and it decreases as the depth of PVA infiltration increases. For model 1, assumed as the reference solution, K_I resulted as equal to 3.71 MPa·m$^{1/2}$ and the computed σ_{yy} values were accurately fitted by Eq. 8 along the whole ligament width (r_v = b). For Models 2-9, in which the crack geometry is modified by the presence of PVA, the stress fields at the crack tip are significantly influenced. It is interesting to point out that for model 2, where no wetting of crack surfaces occurs, the reduction of K_I is almost negligible (5%) and r_v ~ b. As the PVA progressively penetrates into the crack, K_I and r_v decrease until reaching their minimum values for model 5 (K_I ~ 1.0 MPa·m$^{1/2}$ and r_v ~ 0.02·b). In this case the reduction of K_I in comparison with the reference model is 73%. The magnitude of σ_{yy} distribution near the crack tip decreases as well with the increasing infiltration depth and it is shown in Fig. 43. As it is possible to notice from values reported in Tab.15, σ_{yy} values at r = 0.05 mm ($\sigma_{yy}|_{0.05}$) are compared for all the studied models. The variation of E_{PVA} (models 6-9) has only minor effect on σ_{yy} at the crack tip and thus on K_I.

Model	Description	E_{PVA} (GPa)	$\sigma_{yy}\|_{0.05}$ (MPa)	$\sigma_{yy}\downarrow$ %)	K_I (MPa·m$^{1/2}$)	$K_I\downarrow$ (%)	r_v (mm)	r_v/b (-)
1	Reference	4.1	19.62	-	3.71	-	0.500	1.00
2	PVA just on surface	4.1	18.14	7.5	3.54	4.6	0.500	1.00
3	1/3 filled crack	4.1	14.11	28.1	2.82	24.0	0.053	0.10
4	2/3 filled crack	4.1	10.38	47.1	2.13	42.6	0.035	0.07
5	3/3 filled crack	4.1	4.40	77.6	1.00	73.0	0.013	0.03
6	3/3 filled crack	3	4.74	75.8	1.07	71.2	0.014	0.03
7	3/3 filled crack	5	4.20	78.6	0.97	73.9	0.013	0.03
8	3/3 filled crack	6	4.04	79.4	0.94	74.7	0.012	0.03
9	3/3 filled crack	7	3.92	80.0	0.91	75.5	0.012	0.02

Tab. 15. Description of different finite element models with related stress field distribution σ_{22} and K_I.

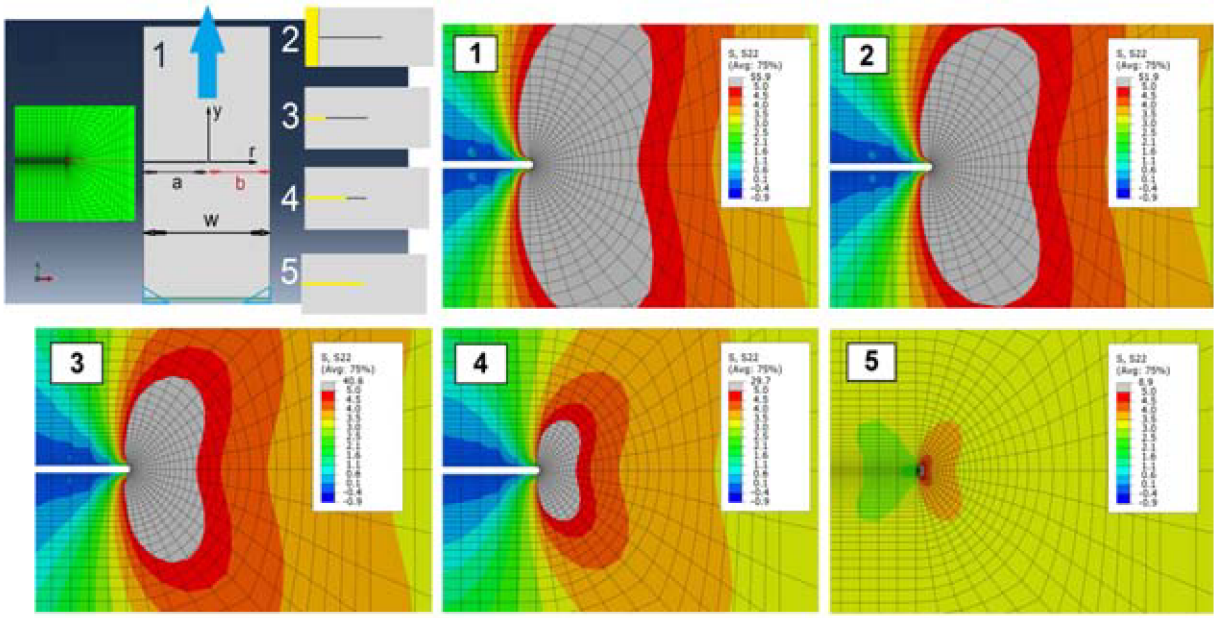

Fig. 45. Two dimensional part, mesh and models used for FEM simulations with related σ_{22} distribution.

5.4.4. Contact angle measurements

The addition of MFC to an aqueous PVA solution wetting a Bioglass surface, caused a decrease of the contact angle. In previous studies, the influence of PVA concentration on surface tension has been discussed [192]. Because of the presence of -OH groups, PVA has the capability of H-bonding with its solvents and decreases their surface tension as other surface active agents. In PVA aqueous solutions, both species, PVA (solute) and water molecules, are free to migrate and exert attractive forces of attraction on their immediate neighbours. Because of the difference in their structure and relative interaction with the neighbouring molecules in the solution, the fields of attractive forces exerted by the PVA molecules is different from those exerted by water molecules. In the bulk solution, PVA molecules remain at a higher free-energy state because of the large association tendency of water molecules among themselves through H-bond. Hence, PVA always has a tendency to migrate from bulk to the surface. The statistical accumulation in the surface of

molecules with weaker fields results in a lowering of surface-free energy. In Fig. 46 the silhouettes of PVA, PVA/5%MFC and PVA/10%MFC of droplets on Bioglass® substrates are shown and measured α values are summarized in Tab. 16.

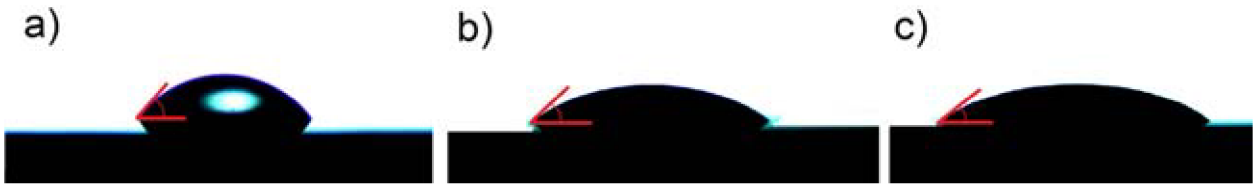

Fig. 46. Drop profiles PVA a), PVA/5%MFC b) and PVA/10%MFC c) on Bioglass® substrates.

Solution	*PVA*	*PVA/5%MFC*	*PVA/10%MFC*
Contact angle (°)	45.14 ± 0.66	34.02 ± 0.74	32.83 ± 1.67

Tab. 16. Contact angles measured for PVA and PVA/MFC solutions on Bioglass® substrate.

5.4.5. Viscosimetry

The PVA solution analysed in this work (0.02 g/mL) showed basically Newtonian behaviour in a shear rate range from 0 to 400 1/s (Fig. 47a). Experimental data are in fact well fitted by a linear function (m = 0.0043, R^2 = 0.999). The PVA/5%MFC solution showed shear thinning behaviour from 0 up to 80 1/s. Data in this range are well fitted by the Herschel-Bulkely model (τ_0 = 0.0139, K = 0.0416, n = 0.7082) and from 80 1/s onwards by a linear function having m = 0.29 (Fig. 47b). PVA/10 MFC solution exhibited analogous behaviour, being fitted by Herschel-Bulkely model from 0 to 110 1/s (τ_0 = 0.0759, K = 0.0670, n = 0.6844) and from 110 1/s onwards by a linear function having m = 0.650 (Fig. 47c). The addition of MFC therefore resulted in an increase of viscosity as expected. For all the solutions, shear-rate vs. viscosity plots are shown in Fig. 47d.

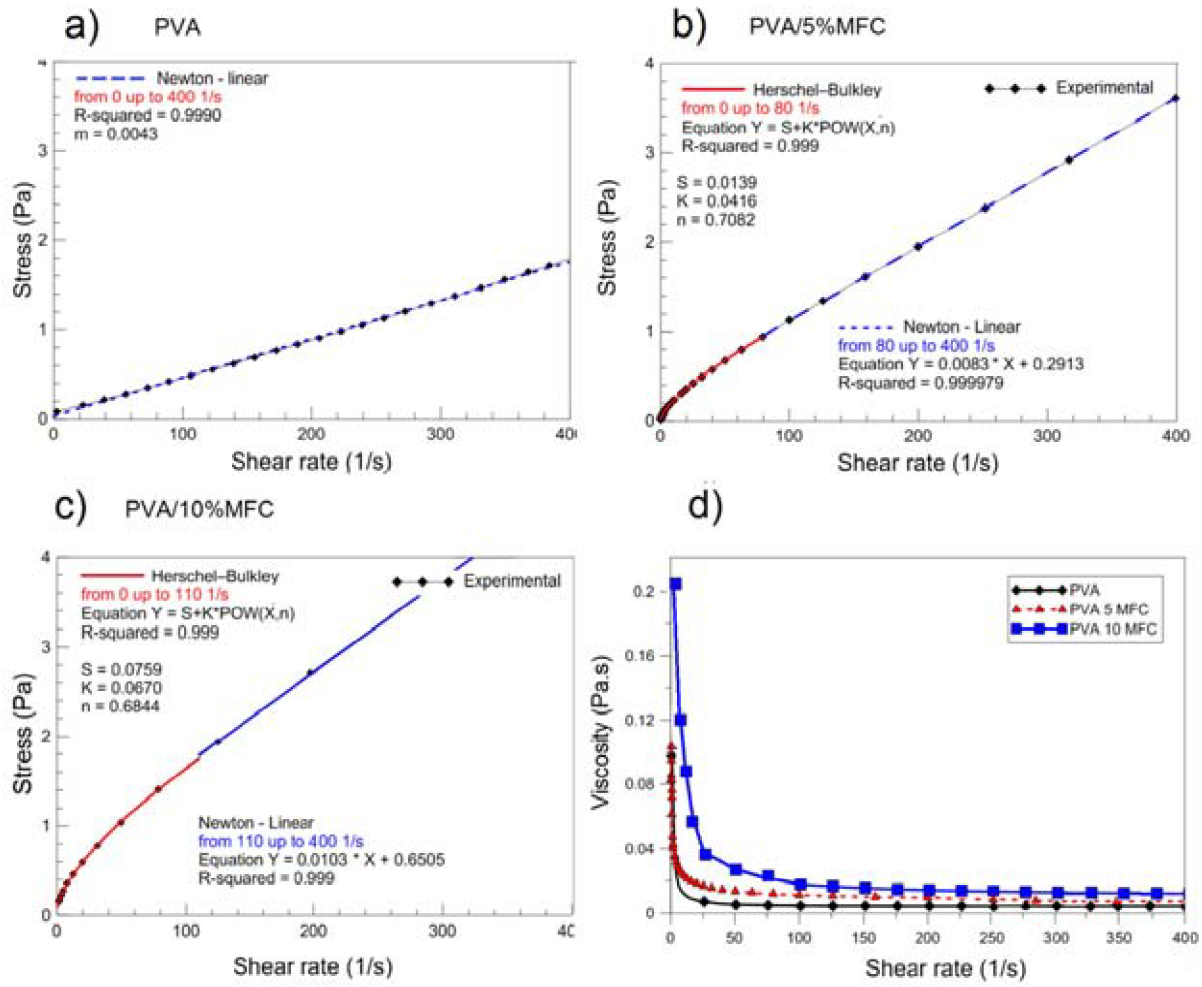

Fig. 47a, b, c) Stress vs. shear rate plots for PVA, PVA/5%MFC and PVA/10%MFC at 25° C and d) viscosity vs. shear rates plots for the three solutions.

5.5. Bioglass/BNNSs composites

5.5.1. Exfoliation of BNNSs by Ball-milling

In Fig. 48 are shown SEM micrographs of h-BN powder milled at 350 rpm in water/PVA (a) and at 350 rpm in isopropyl-alcohol/PVHB at 150 rpm (b). In the first case it is possible to observe how higher energies rather destroy the layered structure instead of exfoliating it. Fig. 48b shows a very interesting phenomenon: some layers seemed to cleave and fold, forming a "forest" of nanotubes still attached to originating particle. Fig. 48c shows a successfully exfoliated BNNS obtained after milling in isopropyl alcohol/PVHB at 150 rpm. The plan surface is lower than $1\mu m^2$ and apparently comprised of 3 atomic layers.

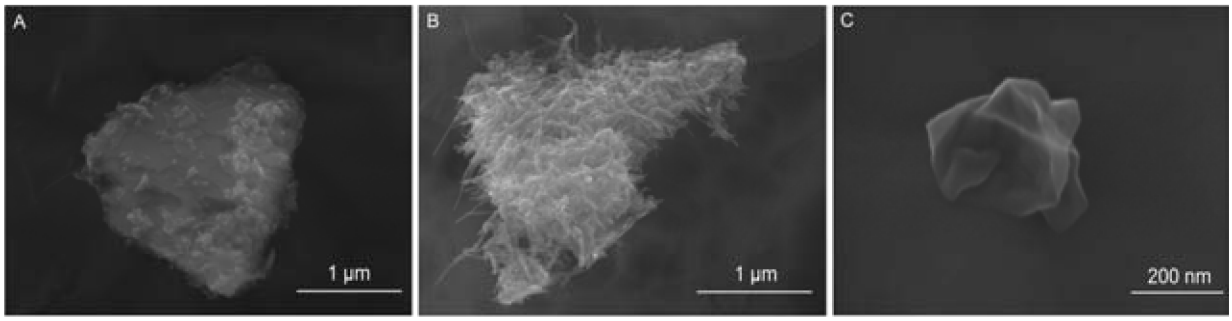

Fig. 48a, b) Excessive ball milling energy lead to destruction of BN particles or formation of nanotubes on the surface (crushing mode). c) Low energy ball milling results in exfoliated BNNSs comprised of few atomic layers (shearing mode).

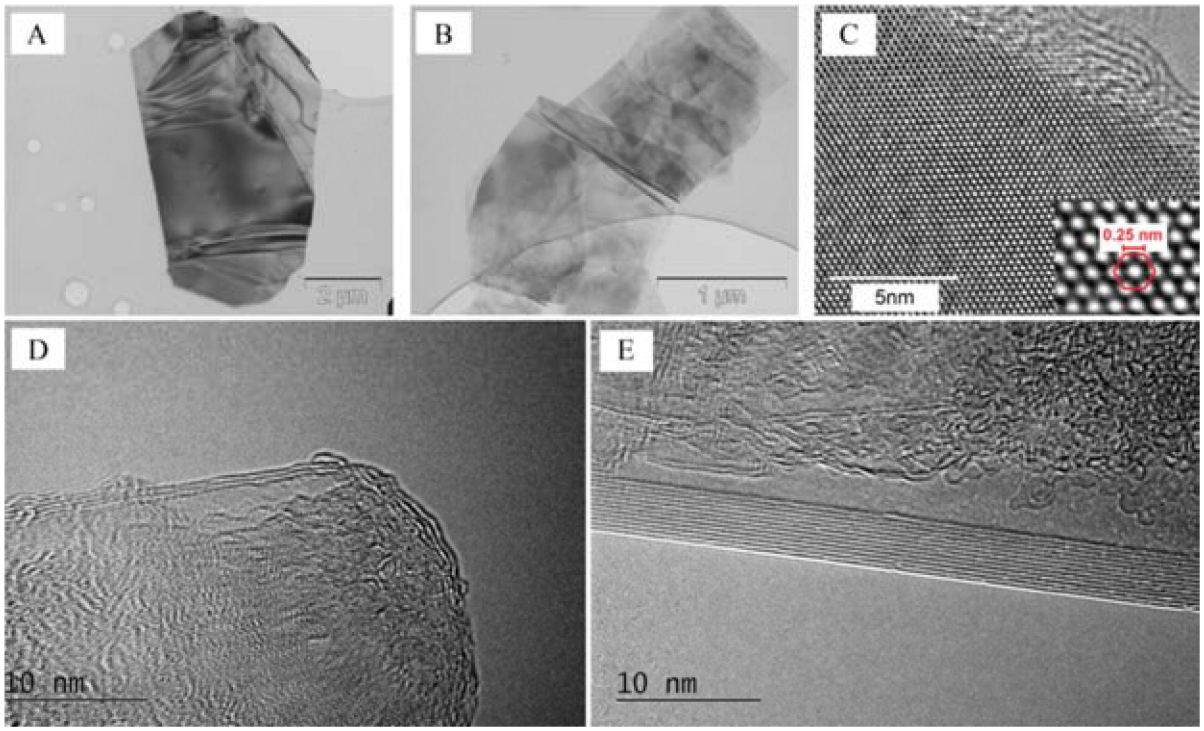

Fig. 49. TEM images of exfoliated BNNSs at low and high magnification. Successful exfoliation of h-BN particles into BNNSs having thickness ranging from 10 to 3 atomic layers was achieved by ball milling under tailored conditions.

In Fig. 49 are shown low magnification (a, b) and high magnification (c, d, e) TEM images of BNNSs suspended in supernatant.

5.5.2. Exfoliation of BNNSs by high energy sonication

The exfoliation by sonication resulted as successful since the sonicated aqueous suspension containing BNNSs appeared stable and no deposited particles were detected after 48 h. The suspension appeared as “milky” (Fig. 50a) and the concentration of BNNSs measured by UV absorption resulted as 0.065 g/dL (Fig. 50b).

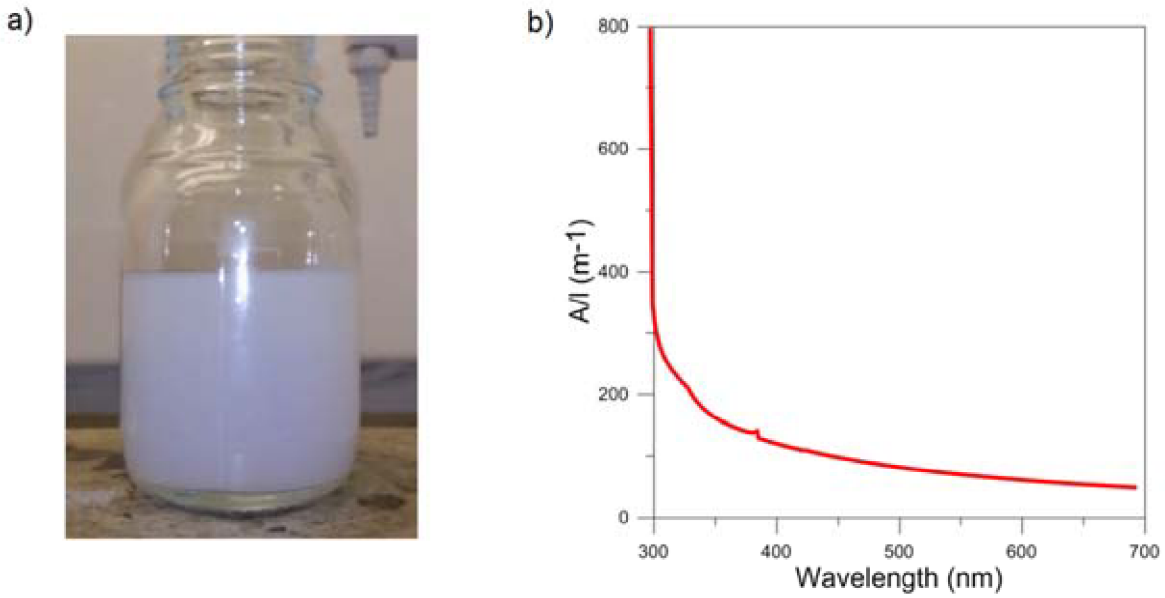

Fig. 50. Aqueous BNNSs suspension used for the preparation of composites and its related UV-adsorption plot b).

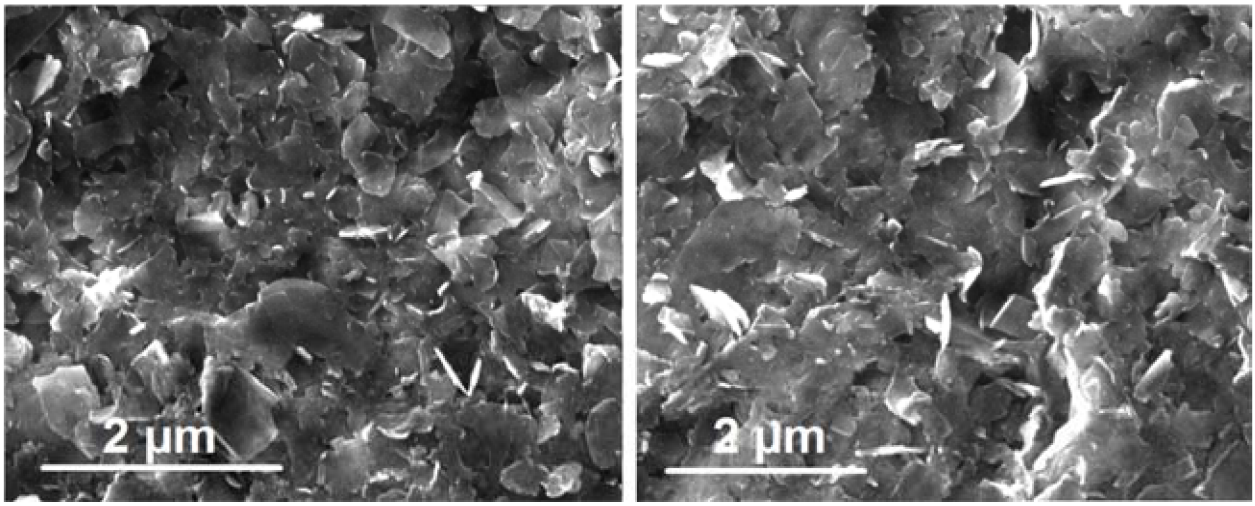

Fig. 51. SEM image of BNNSs obtained by sonication.

5.6. Sintering of Bioglass® and Bioglass® /BNNSs composites

The silhouettes obtained from HSM analysis of Bioglass® and Bioglass®/BNNSs are shown in Fig. 52 for the sake of comparison. In both cases, the glass becomes softer and viscosity significantly decreases as the first shrinkage is reached. At this temperature, (T_1 ~ 532°C) densification starts and proceeds until T_2 ~ 613°C and beyond this temperature a plateau stage is observed. The second densification step starts at 950°C (T_3). The shrinkage associated to the first step is around 12%. Therefore, two distinct sintering steps can be distinguished: a first stage (step 1) and a longer and more marked stage (step 2). The second shrinkage (ΔS_2) has been estimated as ~ 12%.

Concerning the Bioglass®/1%BNNSs mixture, A relevant expansion of Bioglass®/1%BNNSs starts at T_4 ~ 928 and reaches its peak at ~ might be related to either crystallization or the formation of N_2 gas due to oxidation phenomena. All temperatures are summarized in Tab. 17.

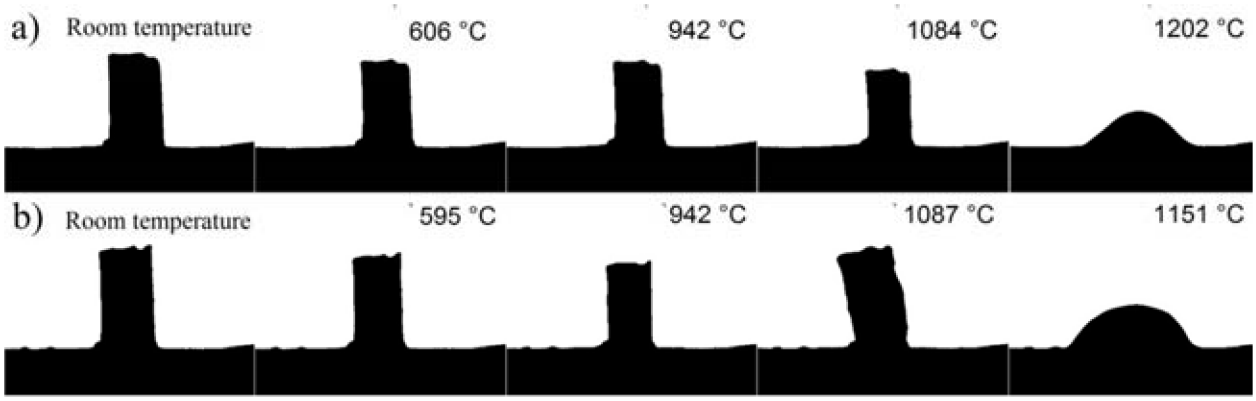

Fig. 52. Silouhettes of Bioglass® and Bioglass®/BNNSs powder compacts at characteristic temperatures.

By observing the DTA plot of Bioglass® in Fig. 51, it can be detected an endothermic effect at T_{g1} = 525°C corresponding to the first glass transition. An exothermic peak corresponding to the first crystallization begins at T_x= 595°C and reaches its maximum at T_{c1} = 655°C . T_x is therefore located between T_1 and T_2, meaning that the crystallization starts during the densification process and it is therefore responsible for suppressing diffusion phenomena by an increase of viscosity and an inhibition of viscous flows. The shrinkage occurring between T_1 and T_2 (ΔS_1) has been estimated as 11%. The temperature range between T_{g1} and T_c is defined as the sintering window. A second small endothermic effect is observed at T_{g2} = 832°C , which corresponds to a second glass transition. Again, it is possible observe on the corresponding HSM plot, that as the temperature is increased beyond T_{g2}, further shrinkage starts at T_3 ~ 931°C and proceeds up to T_4 ~ 1095°C . T_4 can be considered as the end of the second stage of Bioglass® densification or alternatively the onset temperature of melting. That is the reason why a full densification of struts in Bioglass®-based scaffolds can be achieved by the sintering of is carried out above T_{g2}. Finally, melting takes place in the 1100 – 1200°C range.

Glass	T_{g1} (°C)	T_1 (°C)	T_x (°C)	T_2 (°C)	T_c (°C)	Tg_2 (°C)	T_3 (°C)	T_4 (°C)	T_m (°C)
Pure BG	525	532	595	613	655	832	931	1085	1161
BG1%BNNSs	529	531	598	612	647	790	825	928	1200

Tab. 17. Summary of DTA and HSM transition temperature for Bioglass 45S5 and Bioglass 45S5/1%BNNSs mixture, h. r. = 5°C min^{-1}.

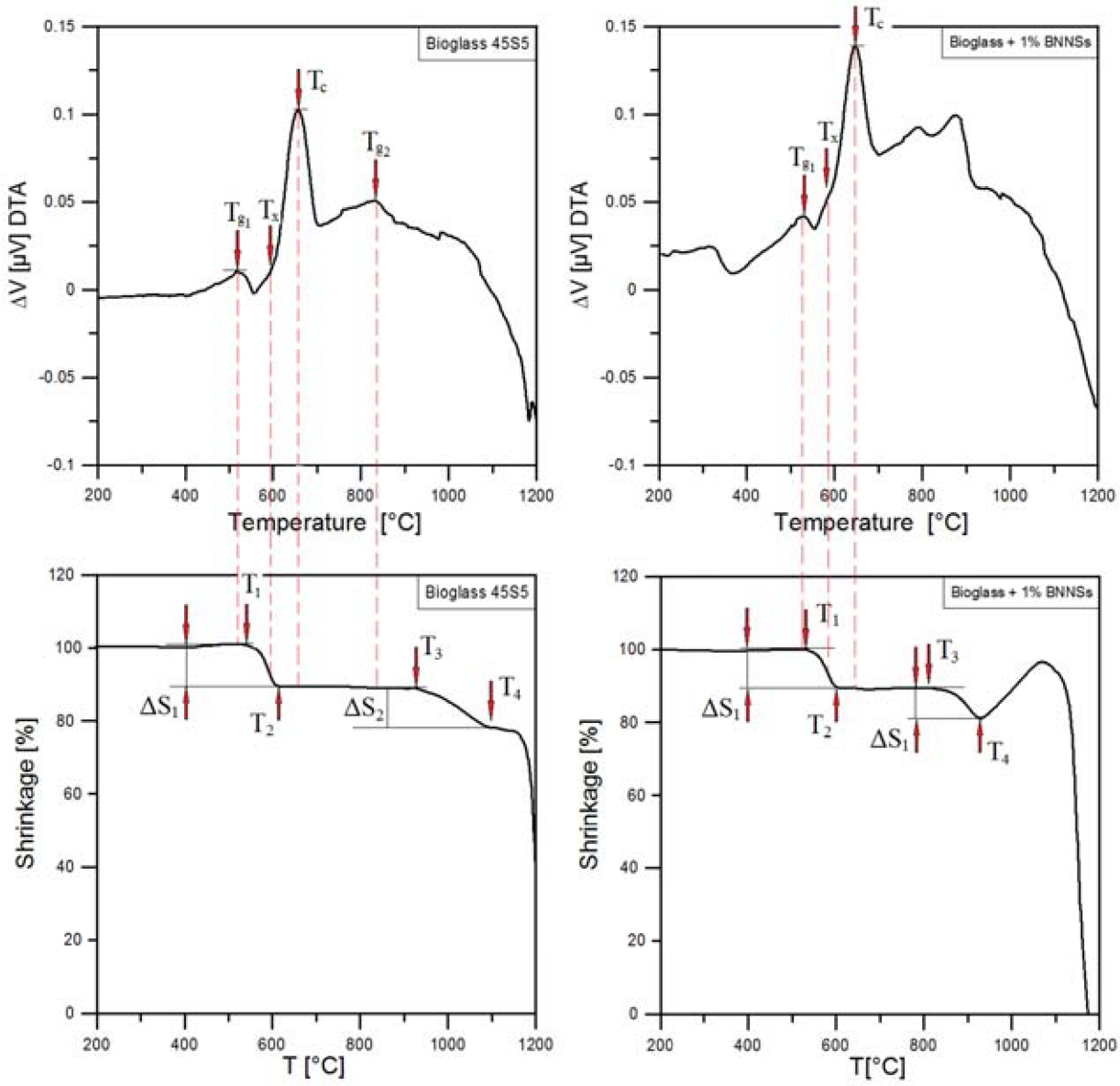

Fig. 53. DTA and HSM plot for pure Bioglass and Bioglass/1% BNNSs composite.

6. Discussion

6.1. Microstructure and mechanical properties of bulk Bioglass®

6.1.1. Conventional sintering

In agreement with literature results [29, 31, 32, 36], two sintering steps were detected by DTA, corresponding to the first and second glass transitions. The heating up to the second glass transition (T_{g2}) turned out as a necessary step in order to achieve a satisfactory degree of densification but anyhow, the two crystallization onsets occurring respectively at 595 and 800°C hinder the viscous flow of glassy phase and prevent the achievement of a theoretically dense material. T_{g1} and T_{g2} values measured in this study, are consistent with those already reported in literature by Baino et al. [193] and Lefebvre et al. [33] who performed DTA on 45S5 Bioglass® powders having comparable particles size. One of the two endothermic peaks commonly attributed to the melting of two different crystalline phases, is visible at T_{m1} = 1161°C , since analysis was run up to 1200°C only. The predominant crystalline phase is identified by XRD as $Na_2CaSi_2O_6$ (combeite high) which is in agreement with results previously reported by Lin [194] and Lefebvre [32]. Despite the fact that several works claim that thermal treatments above 600°C result in the formation of $Na_2Ca_2Si_3O_9$ [15], Lefebvre reported two arguments supporting the presence of $Na_2CaSi_2O_6$ instead of $Na_2Ca_2Si_3O_9$. First, the composition of Bioglass® is closer to $Na_2CaSi_2O_6$. The second consideration comes from the fact that $Na_2Ca_2Si_3O_6$ is isostructural to the high temperature form of $Na_2CaSi_2O_6$ (2 Na^+ replace 1 Ca^{2+} ion). This could be the reason behind the mismatch in the identification of phases. In a recent work, Bellucci et al. [39] hypothesized the coexistence between the two phases but there are no further evidences which confirm this fact. The $Na_2CaSi_6O_{16}$ phase mentioned in other studies was not observed in this case. The crystallization mechanism of the major phase is therefore in agreement with the results of Koga et al. [195], who studied the mechanism of crystallization in the $Na_2O–CaO–2SiO_2$ system leading to $Na_2CaSi_2O_6$.

The secondary crystalline phase detected was α-rhenanite, $NaCa(PO_4)$, which is in contrast with results from Lefebvre [33] and Bretcanu, [196], who observed the crystallization of silicorhenanite ($Na_2Ca_4(PO_4)_2SiO_4$) instead of $NaCa(PO_4)$ in a range between 800–950°C . According to Amara et al. [197] α-rhenanite is characterized by an orthorhombic crystal lattice having indexes a=20.38 Å, b=5.41 Å, c=9.16 Å. These lattice values closely match with those reported for $NaCaPO_4$ (See Appendix I, PDF-2, Ref: 01-076-1456). Previously, Ando and Matsuno [198] established the α→b transformation of the pure rhenanite crystals at above 690°C . Nevertheless, by high temperature XRD using a heating rate of 2°C /min, the transition from α→b was observed already at 580°C. The crystal structure of β-Rhenanite was also investigated by Jalota et al. [199] who calculated the lattice parameters a=5.3653 and c=7.158. α-Rhenanite was as well detected by Höland et al. [200] upon cooling and relaxation of glass having composition (54.6 SiO_2, 14.2 Al_2O_3, 5 CaO, 8.4 Na_2O, 10.7 K_2O, 4.0 P_2O_5, 0.7 F). Their hypothesis was that the nucleation occurs during the rapid cooling of glass and it is controlled by an amorphous glass-in-glass phase separation. The occurrence of a solid solution (s.s) of rhenanite crystals with calcium orthophosphate, $Ca_3(PO_4)_2$ was also

observed, in which the concentration of $Ca_3(PO_4)_2$ can be higher than the one expected in equilibrium conditions. Since XRD peaks of β-rhenanite are very similar to those of silicophosphate phase, it was assumed in previous publications that these crystals were actually a silicophosphate phase but this conclusion might be not correct. From this standpoint, it is interesting to report a study from Rivenet et al. [201] which concluded that it is not possible to obtain final products with compositions of $Na_2Ca_4(PO_4)_2SiO_4$. By using DSC and X-ray thermodiffractometry, they evidenced that both the phosphate and silicophosphate decompose, at low temperature. The phosphate decomposition leads to $NaCaPO_4$ and $Ca_3(PO4)_2$, whereas, the silicophosphate partially decomposes into a $NaCaPO_4$ phase type. According to the synthesis results, XRD, EDS analyses and density measurements, they presumed that $Na_2Ca_4(PO_4)_2SiO_4$ was formulated without taking into account the volatilization of Na_2O at high temperature nor the low reactivity of silicon. They assumed that the phosphate referred as and the silicophosphate $Na_2Ca_4(PO_4)_2SiO_4$ does not exist and it is, actually and $NaCa_6(PO_4)$.

The positive aspect behind this finding is that glass–ceramics containing rhenanite as crystalline phase are reported to be bioactive [202]. Resorbable granular bone grafts based on rhenanite have been in fact successfully commercialized and marketed for the orthopaedic surgeons [199]. Rhenanite or rhenanite in combination with other known crystal phases, particularly hydroxyl apatite, has likewise already been described as bone restorative material. The bioactive properties of pure rhenanite, were described in works by Driessens et al. [203] and Suchanek et al. [204]. According to these, rhenanite displays osteoconductivity in SBF, i.e. a high level efficiency and quality as bone restorative material. β–rhenanite has been found to act as weak interphase for HA-based ceramics [199]. Its debonding abilities of have been demonstrated as well in the HA/bioactive glass laminates

In Fig. 54a SEM image of a Vickers indent with related Palmqvist cracks departing from the corner is shown. At higher magnification (Fig. 54b) it possible to observe that nucleated crystals exert a crack deflection action but their distribution and size are such that an effective toughening cannot be achieved. Peitl et al. [76] analysed the fracture mechanisms occurring in crystallized Bioglass® by mean of different theoretical models and demonstrated that the increase in indentation fracture toughness it is due mainly to crack deflection [191]. Cracks in fact pass through paths of least obstruction or through points where the least amount of energy is released. They therefore propagate along preferably in the amorphous matrix or along preferred crystallographic orientation in the crystallites. The cracks had to twist themselves from the original plane of propagation to the preferred crystallographic plane whenever they encountered a different orientation along the path. For this reason, straight crack propagation in crystalline regions can be attributed to similar (or equivalent energy) crystallographic orientation among adjacent grains.

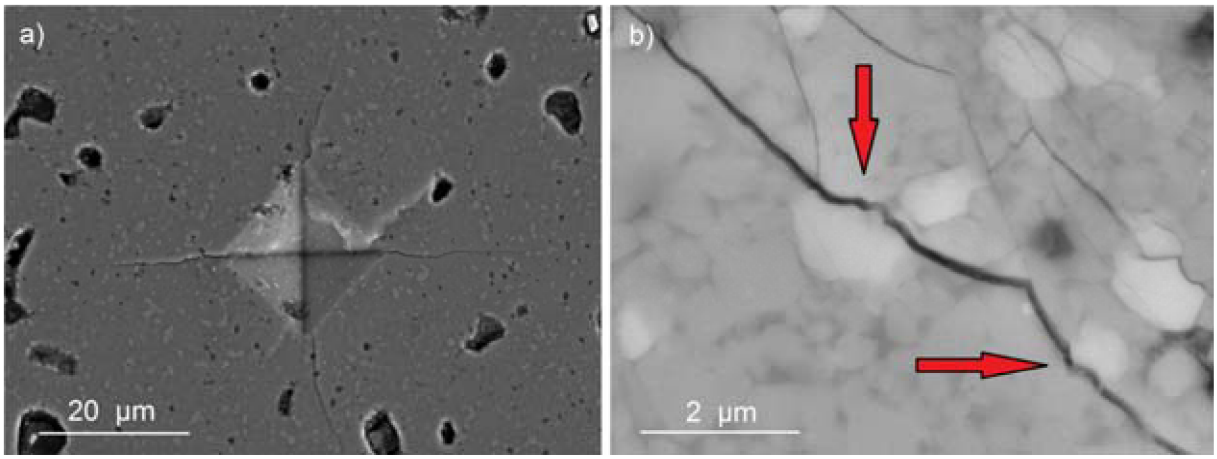

Fig. 54. Vickers indent on oven-sintered Bioglass® surface (1.96 N); b) crack deflection along the boundary of the nucleated crystal.

Residual stresses can also contribute to toughening even though they cause a decrease in toughness at low volume fraction of crystals because to the increased average tensile stresses in the glass matrix [205]. Young's modulus resulted as 89 GPa, being in agreement with values reported by Hench et al. about partially crystallized 45S5Bioglass®. Bending strength values were as well in agreement with those reported by Filho et al. for crystallized 45S5 Bioglass® [76]. Indentation fracture toughness values were as well close to those reported by Nychka et al. who reported a value of 0.23 ± 0.07 MPa·m$^{1/2}$ for indentation loads higher than 0.35 N [72].

6.1.2. SPS sintering

Sintering temperature and pressure were initially set as 600°C and 70 MPa respectively, according to the procedure reported by Grasso et al. [148] Additionally, in other studies was reported that mechanical pressure at low temperatures (550 – 600°C) is beneficial for the sake of densification during the sintering process. In this work, heating rate of 100°C /min (two times higher than the one used in Ref. [148]) was tested in order to assess whether a this could have beneficial effect on densification (i.e. by lowering T_{g1} and broadening of the sintering window).
The samples sintered at 600°C/100°C min^{-1}/70 MPa (Pre1-2-9) exhibited densities ranging from 96 to 97% of the theoretical one, being slightly lower than values reported by Grasso et al. (98.8 – 100%) [148]. K_{IC} measured by indentation technique, resulted 60 % higher than oven–sintered Bioglass®. In the case of Pre9 (sintered at 550°C /70 MPa for 30 min), the density and K_{IC} resulted considerably lower than those sintered in oven, being 2.61 g/cm^3 and to 0.25 MPa·m$^{1/2}$, respectively. In this case, rhenanite was not detected by XRD analysis, coherently to the fact that this phase crystallize in correspondence of the second crystallization peak (T_{c2} ~ 850°C). For samples Pre1-2-9, similar configuration of cracks was observed: Palmqvist cracks depart from the indents corners, similarly to samples sintered by conventional furnace. The length and shape of the cracks is comparable as well (20 < c < 50 µm). At higher magnification it is possible to observe an interconnected crack pattern, distributed along the interface between the glassy phase and the nucleated crystals (Fig. 55a).

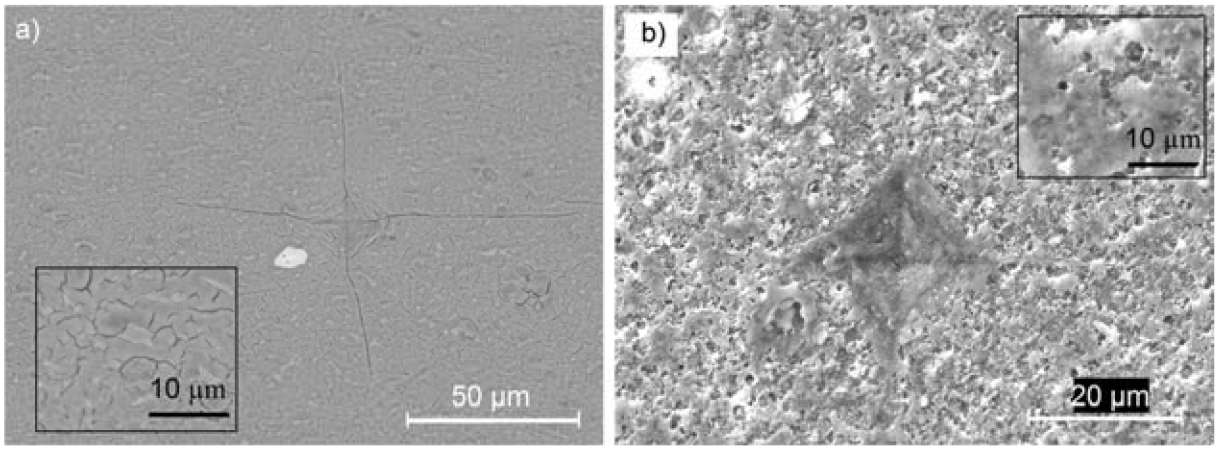

Fig. 55a) Comparison of Vickers indents (1.96 N) on Bioglass® samples sintered at 600°C /70MPa/100°C min^{-1} (Pre1) and b) 1050°/pressureless/100°C ·min^{-1}(PL8). Insets are taken at higher magnification.

Cracking at crystallites–glass interface might occur due to thermal mismatch strain generated in the samples after the phase transformation during crystallization and upon cooling. However, a lack of property data concerning the crystalline and amorphous phases prevents further model development to calculate such thermal residual stresses. Their aspect ratio and largest size were measured by image analysis, ranging from 2 to 10 and from 3 to 10 µm, respectively.

On the contrary, the samples sintered in absence of pressure, at 1050°C and heating/cooling rates ranging from 100 to 300°C /min, exhibited densities close or equal to the theoretical one and a much finer microstructure (Fig. 55b). The absence of detectable pores from SEM pictures is consistent with the material being theoretically dense. From SEM observation of PL6 and PL8 surface, the crystalline and amorphous phases are tightly interlocked at sub-micrometric scale. Even at higher magnification it resulted very hard to clearly distinguish the crystalline domains from the amorphous matrix.

While, the estimation of toughness based on the Anstis approach could have been carried out for samples Pre1-2-9, for PL6 and PL8 would have been subject to consistent error and uncertainty due to the configuration of cracks. As it is possible to observe in Fig. 55b, cracks were hardly visible at the indents corner. For these reasons, the Chevron-notch technique offered a more suitable alternative for the determination of fracture toughness. For the second set of samples, K_{IC} was measured by Chevron technique. Values were found to be from 3 to 5 times higher than oven-sintered Bioglass reaching the maximum values for PB07 and PB08 (respectively 1.4 ± 0.11 and 1.5 ± 0.10 MPa·m$^{1/2}$). Abe et al. [206] demonstrated that a glass-ceramics that features an interlocking crystal microstructure exhibit the highest toughness. Beside the spatial distribution of amorphous and crystalline phase, it should be taken into account the orientation of nucleated crystals. According to Kashyap et al. [38] the crack propagation might be hindered by crack deflection if the crystals are oriented at different angles to the direction of the crack path. In this case, more energy would be required for the deflection towards the preferred crystallographic orientation and the crack would be able to traverse from one preferred crystallographic plane to another.

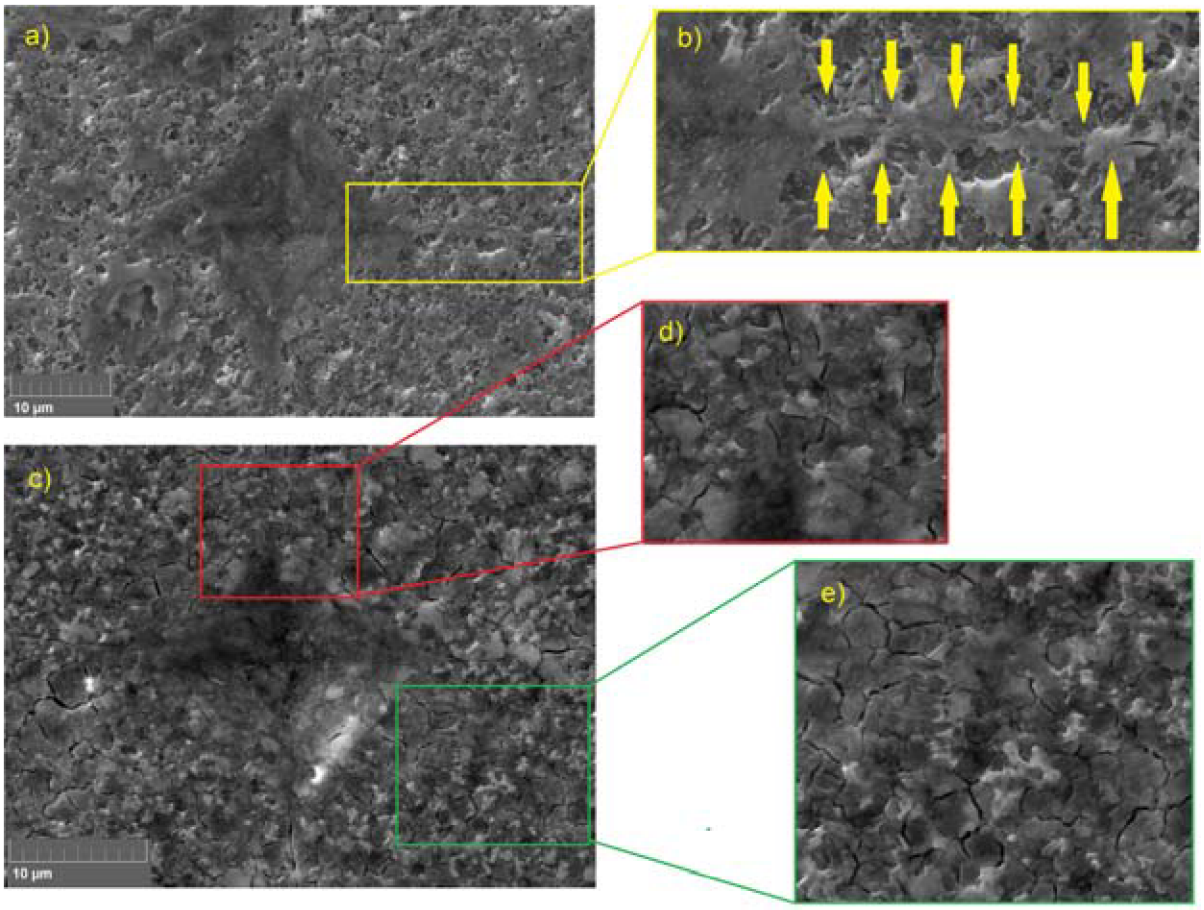

Fig. 56a, b). Vickers indent at 1.96 N on Pre6 observed one week after test. Transformation and healing seems to occur in correspondence of the crack path; c, d, e) Vickers indent at 1.96 N on PB06: Cracking and debonding at the interface of the two phases were observed.

For most of the samples sintered at 1050°C /30min/100°C min^{-1}, it was possible to observe oriented domains along a defined direction departing from the indent corners (Fig. 56a, b). The propagated cracks seemed to undergo a healing process which led to their complete closure. This represents a very interesting phenomenon which has not been reported yet for the 45S5 composition. Non-equilibrium phases might originate pursuant to rapid heating/cooling and recrystallize consequently to the mechanical interaction between the indenter tip and the specimen surface. Another influencing factor could be the atmosphere (vacuum in this case). Although the relationships between the several polymorphisms of silica and silica-based glasses and sintering temperature are well known, the effect of sintering atmosphere and high heating/cooling rates on the crystallization behaviour of silica glass has been poorly described yet. What it has been assessed is that, the composition of the sintering atmosphere and the partial pressure of its constituent influences the diffusivity in the sintering material as well as the densification kinetics, grain growth, phase stability and stoichiometry [143]. The measure of the tendency of a glass to crystallize underneath the indented region has been related to the bond energies of the species that nucleate to form crystallites. According to Clupper et al. [36] in the case on 45S5 Bioglass® this phenomenon should involve preferably the species with the smallest bond energies: Ca–O and Na–O bonds rather than Si–O or P–O bonds. Another factor which must be taken into account is the heating energy generated locally during mechanical deformation. Kim et al. [207] discovered nanocrystallites

beneath indents in bulk metallic glass at room temperature which were presumably nucleated and grown due to the heating energy.

Bioglass® sintered in furnace has the highest amount of $NaCa(PO_4)$ phase, and the amorphous peak in different position that the others. PB01 and PB08 exhibit very similar spectra. By considering values reported in Tab. 13, it can be inferred that the extension of holding time from 30 minutes to 1 hour does not promote a considerable growth of crystallites. As the heating rate increases from 100 to 300°C /min, the amount of β-rhenanite decreases. The amorphous hump increases and slightly shifts towards lower values of θ (Fig. 33).

The Young's modulus of PL8 resulted as 109 GPa, i.e. 22% higher than samples sintered in oven. On the other hand, Young modulus of Pre2 was found to be inferior to oven-sintered samples. This can be due to the lower extent of densification. The small standard deviation of mechanical properties of SPS samples indicates that their mechanical performance is reliable. In contrast, the oven-sintered compacts showed larger scatter of values due to inhomogeneous structure.

For the samples Pre1-2-9, the anelastic part of deformation energy was considerably higher in comparison with the pressureless samples (Tab 10). Nychka et al. [38] reported that there are different mechanisms which could contribute to the increase of anelastic part: heat generation, localized densification of the glass, or more extensive cracking (i.e. the formation of lateral cracks during unloading). The latter could be established as the dominant one, by considering the extent of cracking observed for those samples (Fig. 55a).

In order to determine the kinetic of the phase transformation, the indent morphology was reconstructed by confocal microscope immediately after the indentation and after 24 h from the indentation. The images are compared in Fig. 57. A change of the indent topography is better visible from 2D profiles traced at the center of the indent and at the corner. After 24 h, the area surrounding the indent appears as remarkably protruded, consequently to volumetric expansion. Hence, even if it is not easy to determine what occurs instantaneously in the matrix as the crack propagates (e.g. martensitic transformation) it is possible to conclude that such transformation is time–dependent.

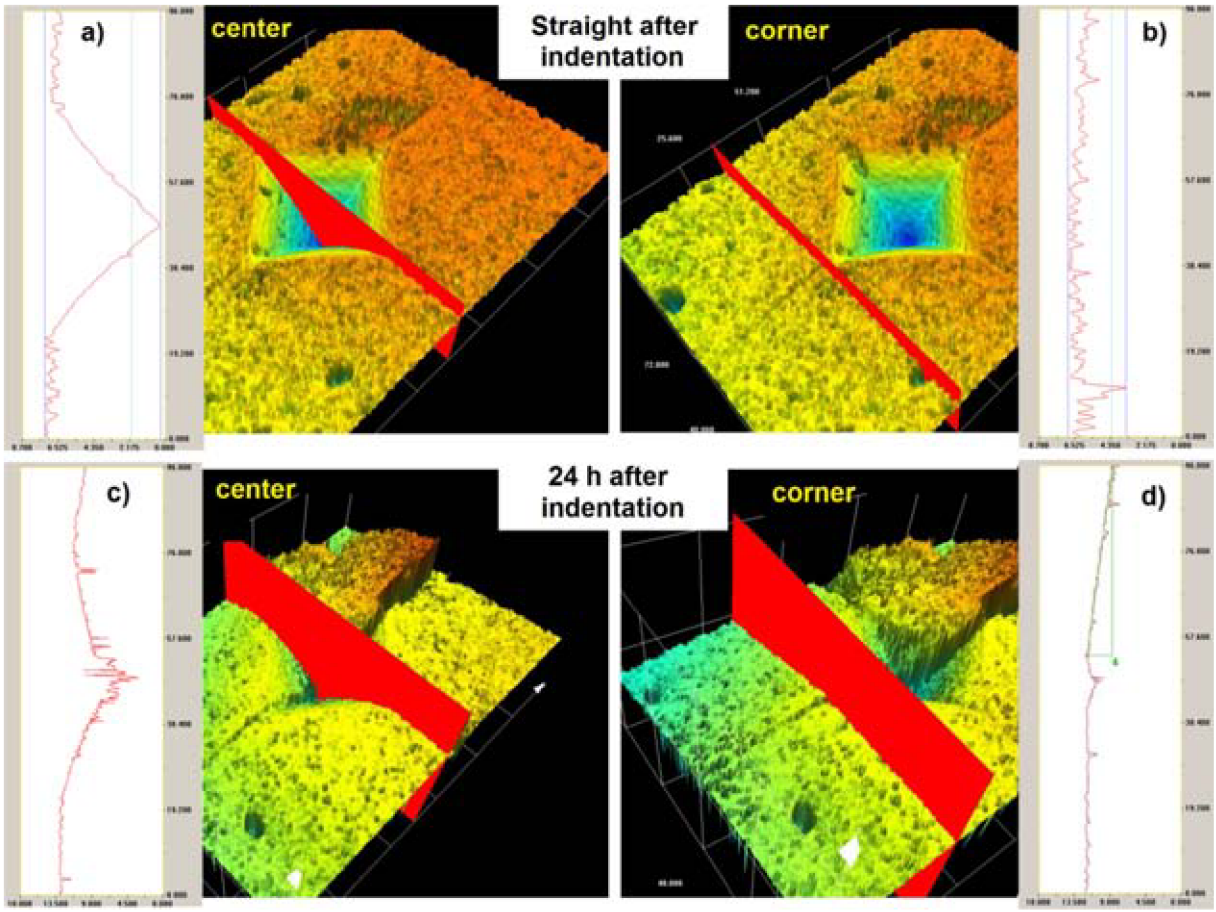

Fig. 57a) 3D reconstruction of the indent profile straight after indentation; b) 24 hours after the indentation with related 2D profiles.

6.2. Bioglass® scaffolds uncoated and coated with PVA/MFC composite coating

6.2.1. Microstructure

The scaffolds produced by the ethanol-based slurry exhibited higher degree of interconnection and open porosity in comparison to those produced according to Ref. [45]. The lower surface tension of ethanol likely results in a slurry with better wettability towards the PU surface and the unwanted formation of liquid membranes is prevented. Additionally, another interesting phenomenon was observed: the reversible swelling of PU template caused by ethanol induces volumetric expansion of the cells, easing the infiltration of the slurry into the inner cells of the template. Even if the ethanol-based slurry process may have not been optimized in the present study, it is important to note that these favourable aspects enable the production of foams having constant cell geometry and uniform strut thickness. Apart from facilitating the coating process, it has to be considered that binders also act as pore forming agent during the sintering process. For instance, Jamaludin et al. [208], reported that the samples produced by using natural binder resulted in foams with bulky struts, finer surface, and more uniform cell appearance than the synthetic binders. Anyhow, among the binder tested in this work (PVA and PVHB), it was difficult to assess from SEM images, which binder resulted in a minor amount of surface porosity. The shear thinning behaviour of the PVA

aqueous solutions suggests to carry out the dip–coating process in conditions of moderate stirring rather than into a stationary suspension. These should ease the penetration of the solution into the cells of the template due to its shear thinning behaviour. Conversely, after the coating process, the slurry viscosity increases thereby allowing the slurry to adhere to the PU template.

The solid in the fraction was kept as low (30% vol.) in order to promote a homogeneous distribution along the template struts. The sufficient amount slurry was therefore obtained by increasing the number of dipping. It has been reported that higher viscosity slurries (solid fraction: 50–70%) lead to accumulation of particles and blockage of the open cell, thus creating rough surface and closed cell morphology [208].

Recent modelling works based on finite element analysis refer to these two characteristics as beneficial for the strength of reticulated ceramics [65]. More specifically, the stress analysis showed that compression stresses tend to concentrate on the thinner struts. Therefore, the optimization of the processing route in order to minimize the distribution of struts thickness is a desired goal. As reported in several works dealing with scaffolds for bone replacement, the achievement of a highly open porous structure is one of the crucial requirements in order to ensure migration of cells and exchange of ions between the scaffold and the surrounding biological environment, and therefore to promote the bioactivity [19, 29, 201].

A sufficient degree of open porosity is also beneficial for a more effective penetration of the polymer coating along the struts surface. Image analysis of μ-CT slices revealed a non-uniform distribution of the ceramic phase along the foam height, indicating a higher amount at the centre of the sample. The mean value of 9.6% (Fig. 58) is anyhow in good agreement with the density values obtained by Eq. 17. This might be due to the presence of pores completely filled by the slurry and it is related to manual character of the process. Such configuration constitutes a disadvantage since the weakest parts are those in contact with testing apparatus and subject to premature fracture.

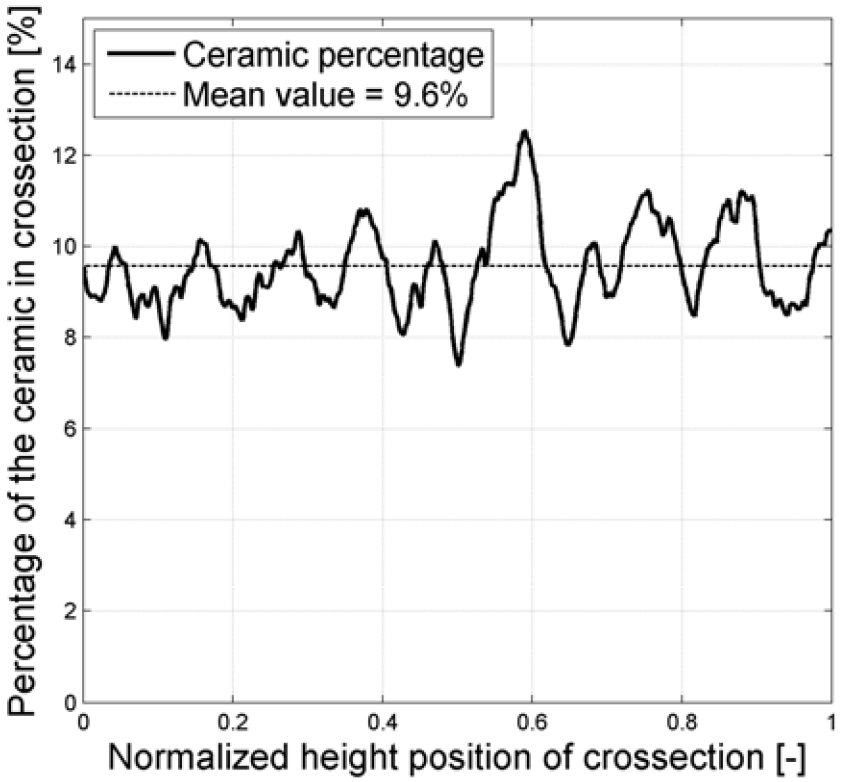

Fig. 58. Area fraction of ceramic in function of the normalized height of the cross-section from µ-CT.

6.2.2. Mechanical properties

The reduced struts thickness and surface defects, which are inherently associated with the manufacturing procedure, together with the low strength of Bioglass®, explain the poor mechanical capability of the non-coated scaffolds reported in this work. Nevertheless, the compressive behaviour observed differs from the one reported by GA model for brittle foams (Fig. 59a), which predict the collapse after reaching maximum critical compressive stress [30]. The samples produced in this study collapsed progressively during the test in a steady manner (Fig. 59b). The shape of the structure was still recognizable, but the height of the sample which was vertical to the force was progressively reduced. This phenomenon can be related to the intrinsic brittleness of the material, the existence of micro-pores in the struts, the non-constant distribution of the ceramic phase along the height of the sample (Fig. 58) and the high amount of porosity (~90%).

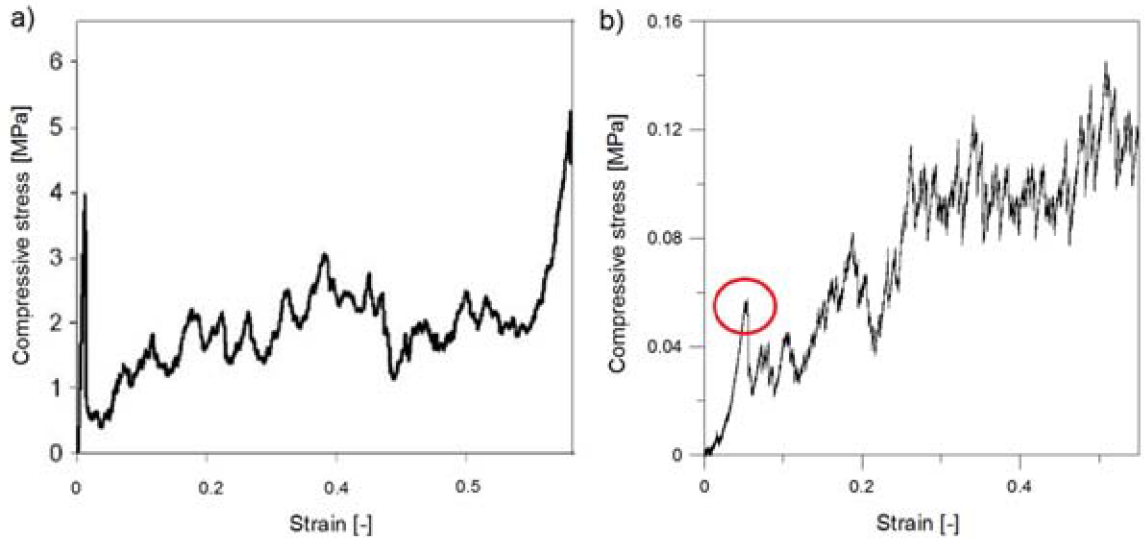

Fig. 59a) Stress vs. strain curve obtained from the compressive test of alumina foam and b) of uncoated Bioglass® scaffolds object of this work.

The coated samples exhibit demonstrably different mechanical behaviour in comparison to non-coated ones: the first fracture events take place at a remarkably higher load (at least of one order of magnitude) in comparison with non-coated samples and they are followed by a drastic drop of load. The PVA infiltrates and fills surface defects and cracks derived from the sintering process, suppressing them to act as stress concentrators and crack initiators, in agreement with the computed results reported in Fig. 45.

It has to be taken in account that in the case of polymer–coated foams, the foam inherits the strain rate-dependence of the solid polymeric material constituting the coating. A relationship for the strain–rate dependency of the yield strength of a polymers is given by Eyring [211]:

$$\sigma_{ys} = \frac{kT}{v_{act}} ln\left(\frac{\dot{\varepsilon}}{C_3}\right) \tag{33}$$

In which σ_{ys} is the yield strength of the solid polymer, k is the Bolzmann constant, T is the current temperature and ν_{act} is a so called activation volume. The strain rate is given by $\dot{\varepsilon}$ and C_3 is a temperature–dependent parameter.

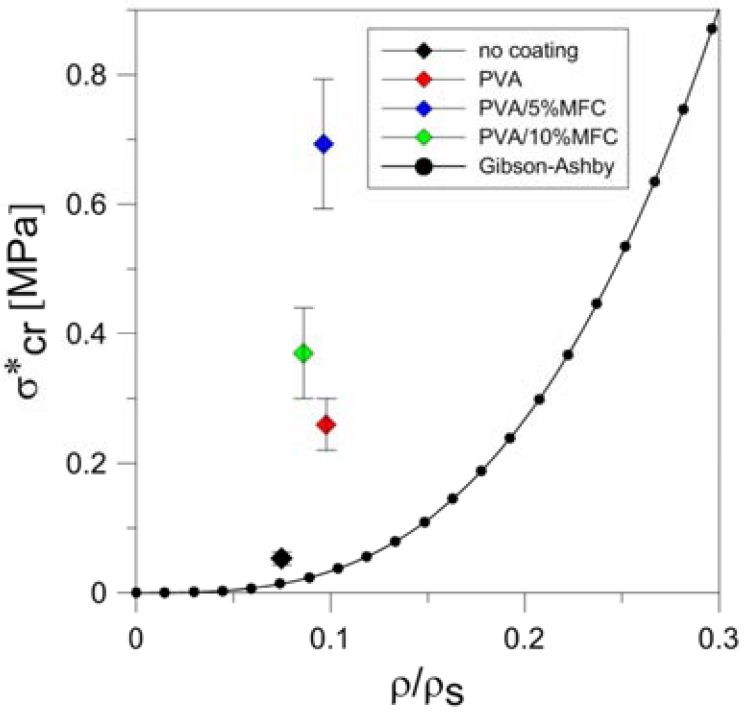

Fig. 60. Comparison of compressive strength predicted by Gibson-Ashby model and experimental values measured for uncoated and coated scaffolds (right).

In Fig. 60 it is possible to see the comparison between the experimental values of compressive strength of scaffolds and those predicted by GA model. The threshold value obtained from the three-parameters Weibull distribution was substituted to σ_{fs} in Eq. 12. The underestimation of experimental values by the GA model can be ascribed to different reasons, for example the deformation mechanisms of the GA unit cell that is not truly representative of the real cell structure. Additionally, GA model is based on the assumption that the material is defect-free and homogeneous and it does not take into account of other factors such as the slenderness of the struts, presence of filled cells etc.

Internal Von Mises stress distribution computed in a previous study [65] elucidates how the nodes are subjected to tensile stresses along to the load direction as the scaffold undergoes a compression load. In these regions, concentrated tensile stress can trigger crack propagation. From this standpoint, the presence of coating on struts surface would be therefore beneficial also for compressive properties of reticulated ceramics. The magnitude and appearance of the plateau depends on the mechanical response of the coating to the applied stress. PVA/5%MFC-coated samples exhibit a jagged plateau characterized by sharp and wide peaks, differing from PVA-coated samples, whose plateau area appears as much smoother. Such peaks likely correspond to the fracture events of MFC fibrils embedded in the PVA matrix. The increase of weight after coating was slightly higher for PVA-coated samples and decreased for PVA/MFC coated samples. According to Gibson [58], the compressive strength of spongy bone (not the strut) is in the range of 0.2–4 MPa, when the porosity is 90%. Hence, the measured compressive strength (0.3–0.7 MPa) of the PVA/MFC coated-foams falls in this range. Based on the author's experience, as the compressive strength overcomes 0.2 MPa, it is possible to handle the foam. In addition, it has to be

considered that the compressive strength of a scaffold might significantly increase (e.g. from 10 to 30 MPa) consequently to the tissue ingrowth in vivo [212]. It has also been speculated that it might not be necessary to fabricate a scaffold with a mechanical strength equal to bone because cultured cells on the scaffold and new tissue formation in vitro will create a biocomposite and will increase the time-dependent strength of the scaffold. PVA/MFC-coated Bioglass® scaffolds exhibit therefore an appropriate mechanical competence.

The addition of 5 wt. % and 10 wt. % of MFC fibres cause depletion of elastic modulus and strength as the precursor mixtures are stirred for 24 h. By increasing the mixing time of PVA/MFC mixture up to 48 h, the MFC fibres seems to become effective as a reinforcing element and noticeable enhancement of strength and modulus is achieved. As previously reported [122, 127, 130], the achievement of a homogeneous and intimate dispersion of MFC fibres in polymeric matrix is a key parameter for the mechanical strengthening of MFC-reinforced composites. A comprehensive study about the influence of different processing parameters on the PVA/MFC composite microstructure has been provided by Bulota et al. [213]. Contrary to the author's results, they recorded a depletion of the overall mechanical properties of the PVA/MFC composites as the stirring time increase, yet a satisfactory explanation has not been provided. In fact the viscosity and pH measurements reported in Ref. [213], excluded the occurrence of PVA degradation during mixing. Furthermore, polarized light microscopy also excluded the presence of contaminating nuclei, hence their thesis is questionable.

SEM observations carried out on the surface of pure MFC films provided insights about sizes and aspect ratio of the MFC fibrils used in this work (Fig. 61) Fracture surfaces of the broken films are shown. Fig. 61b and 61c reflect the mechanisms of deformation and fracture for PVA/10%MFC stirred for 24 h and for PVA/10%MFC foil stirred for 48 h, respectively. For the former, the inner structure appears as inhomogeneous because of sedimentation of MFC longer fibrils at the side in contact with Teflon® plate. This phenomenon indicates a poor dispersion of MFC and the precipitation of bundles of fibres, similarly to the precipitation of flocculated particles occurring in a colloidal suspension. PVA/10%MFC film stirred for 48 h appears much rougher and exhibits two level of the MFC influence. A micro-level represented by very fine fracture features caused by separate MFC fibrils and a macro-level associated with the fracture of packs formed by the MFC fibrils bundle and surrounding PVA matrix. Both this fracture mechanisms contribute to the overall increase of the fracture energy. Hence, the optimal reinforcing effect of the composite coating is expected when the coating exhibits the highest rigidity and toughness. It is also worth noticing that the fracture surface shown in Fig. 61c exhibits fibrous character, similarly to the coating fracture reported in Fig. 39d. In both cases, the amount of fibres is the same but the processing conditions differ (24h vs. 48h stirring). Additionally, the substrate on which the coating is deposed (i.e., material and morphology) might also influence the final film morphology.

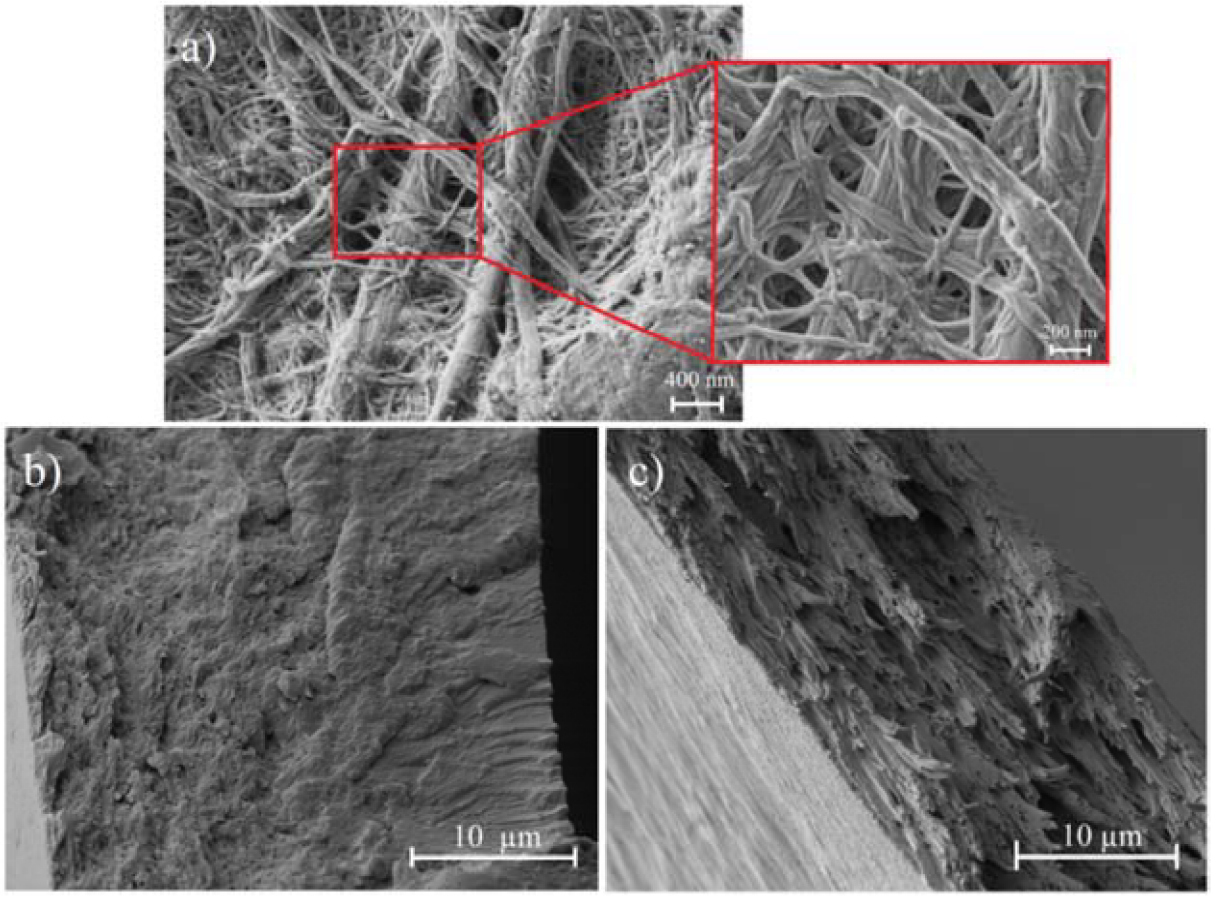

Fig. 61. MFC fibrils observation a), fracture surfaces of a PVA/10MFC foil stirred for 24 h b) and a PVA/10MFC film stirred for 48 h c).

6.2.3. FEM results

For all the cell unit models analysed (O, O-S1, O-S2 and O-S3), Von Mises stresses resulted as comparable (from 3.71 MPa for "O" to 3.8 MPa for the "O-S3"). Therefore, the presence of the cavity does not induce any severe stress concentration within the structure. The highest Von Mises stresses occur at the constrained faces of unit cell. More precisely, the location of the stress peaks are at the corners of the triangle faces (Fig. 43). Stress concentration is induced by the outer shape of the unit cell respect to loading and constraints configuration. From this perspective, it would be beneficial to design scaffolds having rounded cross-sectional shape, avoiding sharp edges. Additionally it has been demonstrated that maximum local stresses occur at the middle-length of the struts or at the nodes, in agreement with Marciàn et al. [210]. While the central cavity does not strongly affect the mechanical properties of the structure, the cross-sectional irregularities cause stress concentration.

In previous works, the reinforcement of scaffolds due to the presence of coating was ascribed to a lowering of the stress concentration at the defect sites on the strut surface, allowing a further increase of the remote load without any failure occurs [190, 212, 213]. Results from FEM on the two dimensional strut confirmed this fact, demonstrating that the dominant criterion for the sake of

strengthening is extent of coating infiltration into surface cracks, which is maximized as the polymer reaches the crack tip. In fact, as the polymer reaches the crack tip, the highest reduction of K_I and σ_{yy} is achieved. It is therefore crucial to optimize the wettability and viscosity of polymeric solutions designed for dip-coating (i.e. the choice of a suitable polymer-solvent system and polymer concentration) in order to maximize the infiltration capability into the surface defects. Although the FE analysis was based on a single strut, these outputs, together with contact angle and viscosity measurements, can offer a good interpretation of the experimental results obtained from tensile test of scaffolds. Previous studies on brittle open-cell ceramic foams confirmed that the mechanical properties of the constituting struts determine the mechanical behaviour of the whole foam [216].

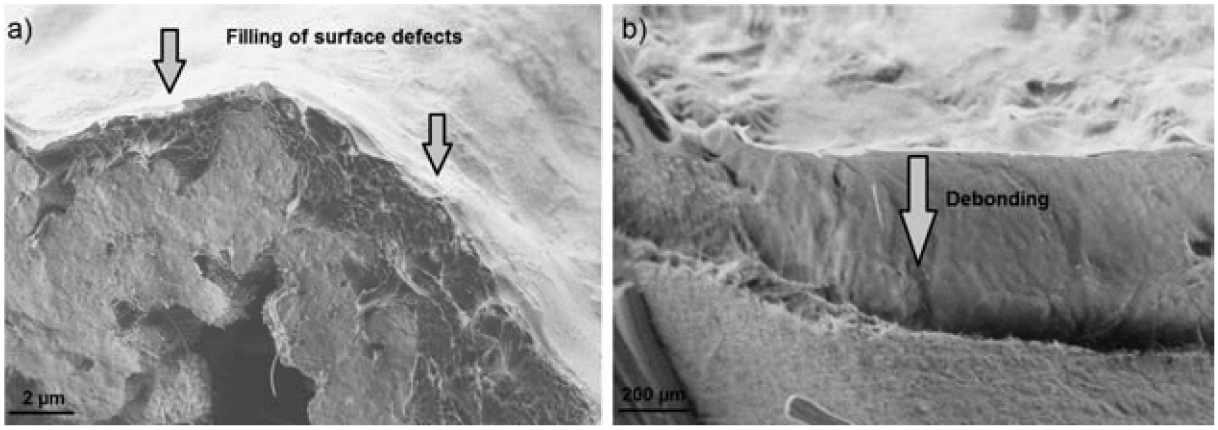

Fig. 62a) PVA/MFC coating filling the surface defects and b) PVA/MFC coating debonded in proximity of a fracture surface.

By considering that MFC has been proven to enhance the infiltration of coating into cracks and that the latter is the main criteria for the reduction of K_I, it can be stated that the experimental results obtained from tensile tests are in good agreement with computed values.
In Tab. 18, the contact angles, linear viscosities of all the coatings produced, together with the tensile strength and porosities of related scaffolds (σ_t) are summarized. The experimental tensile curves of uncoated and coated scaffolds and the variation of $\sigma_{yy}(r)$ at (y=0) plotted for models 1-5 are compared in Fig. 63.

Coating	**α** (°)	**Linear η** (Pa·s)	**P** (%)	**σ_t** (MPa)
-	-	-	-	0.014 ± 0.0031
PVA	45.14 ± 0.66	0.0043	90.22 ±	0.196 ± 0.009
PVA/5%MFC	34.02 ± 0.74	0.0083	90.38 ± 1.49	0.271 ± 0.012
PVA/10%MFC	32.83 ± 1.67	0.650	91.39 ± 1.59	0.335 ± 0.066

Tab. 18. Summary of coating produced, contact angles, linear viscosities, and porosity and σ_t of related scaffolds.

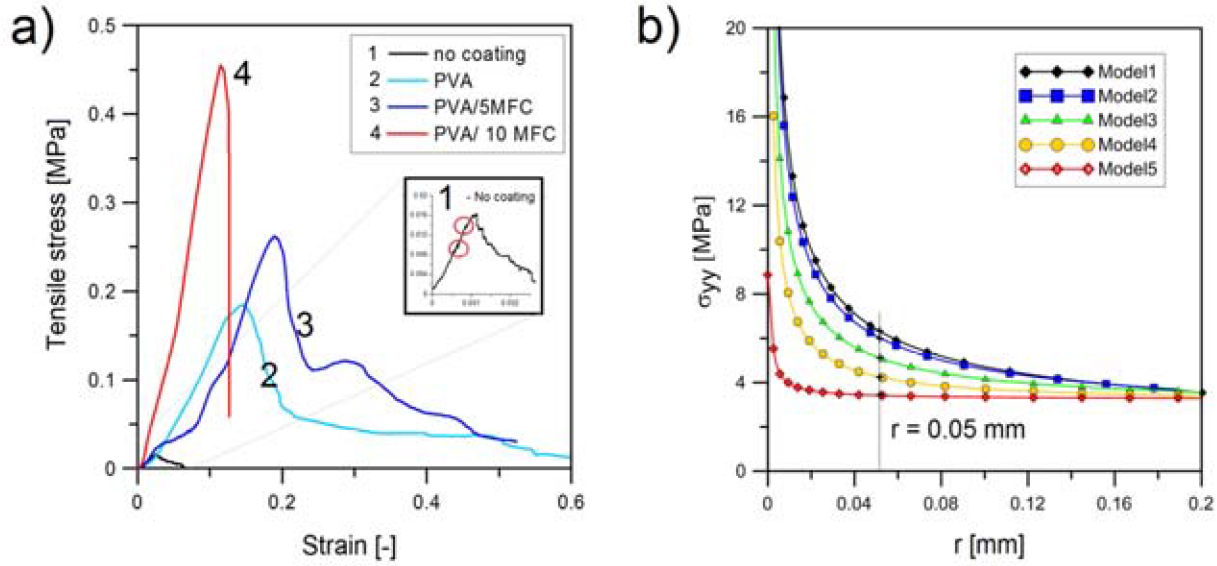

Fig. 63a) Characteristic stress vs. strain curves from tensile test for uncoated and coated scaffolds and b)σ_{22} as a function of distance of the crack tip (y=0).

Cellulose fibrils are also characterized by a high density of –OH groups on the surface, which have the tendency to bond with adjacent –OH groups by weak hydrogen bonding with other fibres, with PVA and water. Similarly for PVA, this phenomenon can be responsible for the further decrease of surface tension and contact angle, as observed. Cellulose fibrils are also characterized by a high density of –OH groups on the surface, which have the tendency to bond with adjacent –OH groups by weak hydrogen bonding with other fibres, with PVA and water.

Concerning, the rheology of PVA aqueous solutions, it depends on several factors such as temperature, PVA concentration, percentage of hydrolysis and degree of polymerization (DP) [217]. Nevertheless DP and concentration have been reported as having the stronger effect on the viscosity [218]. The reason is that the chain length or the higher chain concentration promotes in larger extent the formation of inter- and intra- molecular hydrogen bonding. As a result, water becomes a poorer solvent and hence the viscosity of the solution increases. Several authors have reported the rheological behaviour of PVA solution as shear thinning [213, 214]. The PVA solution analysed in this work (0.02 g/mL) showed Newtonian behaviour in a shear rate range from 0 to 400 1/s. This means that for such concentration, inter– and intra– molecular interaction are not sufficient to determine a consistent increase of viscosity. The viscosity increased due to the presence of MFC, as expected. Cellulose fibres in fact act as a thickener in aqueous solution because of their hydrophilicity [221]. For PVA/5%MFC and For PVA/10%MFC the changes of behaviour from Herschel-Bulkely to Newtonian at respectively 80 and 100 1/s, suggest that beyond these points, structural rearrangement takes place.

6.3. Bioglass®/BNNSs composites

Ball milling resulted successful for the exfoliation of BNNSs and it was initially taken into account for the fabrication of Bioglass®/BNNSs through a wet process, i.e. by mixing Bioglass® slurry and

BNNSs aqueous suspension in order to obtain composite green body containing the desired of BNNSs. Such slurry could have been used as well for the preparation of porous scaffolds by replication technique. As reported in previous study [160], the most straightforward method to determine the number of layers of a BNNS is to directly count the straight lines at the folded edges from TEM images. By following this procedure, the average number of layers in BNNSs exfoliated by ball-milling technique, were found to range from 3 to 15. Anyhow, due to the difficulty to find such places, the resulting statistics was very poor and could not be considered representative of all population. Nevertheless it is interesting to notice from high magnification plan views (Fig. 47c, d) the abundance of defect-free areas, confirming that ball-milling performed under tailored conditions enables the production of good quality BNNSs. Other quantitative data are in good agreement with the literature as well [161]: the distance of periodic bright regions in is about 0.24-0.25 nm and the spacing of edge fringes at the edges 0.32-0.37 nm. Although the AA stacking is always observed in few-layered BNNSs prepared by top-down exfoliation processes [222], there have been calculations that suggest that the adjacent BN layers might freely slide from AA stacking to one of the AB stacking types (N-centered on borazine rings on adjacent layers) along certain energetically favourable directions despite a bandgap reduction of 0.6 eV. Such phenomenon can be observed on the superimposed BN planes shown in Fig. 49c.
Concerning BNNSs prepared by sonication, the as-obtained dispersion appeared as “milky”, similar to those reported by Lin et al [160]. Also comparable was the apparent stability of the aqueous h-BN dispersions, with no precipitation detectable over a few days. The size of BNNSs and size distribution resulted as smaller (longest size < 1 μm).

HSM of Bioglass®/1%BNNSs powder mixture evidenced a relevant volumetric expansion starting at T_4 ~ 928°C and reaches its peak at nearly 1070°C . This phenomenon could be likely related to the formation of N_2 gas, pursuant to oxidation. This is not surprising, since several works reported that BN can be oxidized into boric oxide at temperature ranging from 800-900°C in presence of oxygen and moisture according to Eqs. 34 and 35:

$$B1.0N0.9(s) + 2O_2(g) \rightarrow 2B_2O_3(1) + 1.8\ N_2(g) \quad (34)$$

$$4B1.0N0.9(s) + 3H_2O(g) \rightarrow 2B_2O_3(1) + 3H_2(g) + 0.9N_2(g) \quad (35)$$

The formation of NO_2 as a by-product has been also reported by Samsonov et al. [223]. In the absence of moisture, BN experiences minimal oxidation up to 800°C , above which B_2O_3 glass is formed on its surface. At temperatures lower than 1100°C , B_2O_3 has a low vapour pressure (less than 2 x 10^{-3} Torr) and consequently volatilizes slowly. These issues suggested to use SPS technique for the sintering of Bioglass®/BNNSs composite. Unfortunately the endeavours carried out by the author did not result as successful. The sintered sample broke during the cooling process or exhibited large amount of defects.

7. Conclusions

Mechanically reinforced Bioglass® scaffolds were successfully prepared and properties demonstrated within this work. A number of achievements were reached in the various fields thanks to the complexity of the research conducted. Modified production route of scaffolds, effect of coating wettability, preparation of fully dense bulk Bioglass®, self-healing ability of Bioglass® at room temperature and production of BNNSs are some of them. Main results of the work are summarised in the following chapters and remaining open questions about possible further directions of investigation are also outlined.

For the first time ethanol-based slurry has been adopted for the production of 45S5 Bioglass® scaffolds. Resulting scaffolds exhibited 3D interconnected structure with higher degree of open porosity in comparison with water-based Bioglass® slurries commonly reported in literature. Both PVA and MFC composite coatings were successfully applied to the scaffolds by dip–coating without reducing the open porosity. PVA-coated scaffolds exhibited approximately 5 fold increase of compressive strength compared to uncoated ones and the addition of 5 wt. % of MFC fibres led to a noticeable 10 fold increase of compressive strength. Also tensile strength has been found to be remarkably improved by the PVA/MFC composite coating; the scaffold coating containing PVA with addition of 10 wt. % of MFC exhibited more than 20 fold increase of tensile strength compared to non-coated samples. Fractographic SEM observations showed how PVA is able to infiltrate within the struts surface defects reducing the stress concentrations and providing effective load transfer from the scaffold to the MFC fibres. In addition, fracture of MFC fibres contributed to the energy dissipation process which led to the increase of the overall toughness of the scaffolds.

As future development, the rheology of the polymeric solution (i.e. optimal MFC/PVA ratio) must be investigated in order to achieve a more homogeneous distribution of the composite film on the struts surface and possibly to enable an effective penetration and filling of the central hole in the struts. Strut-coating adhesion strength measurements are also required to assess the quality of the bonding between the coating and the strut surfaces which has a marked effect on the extent of toughening by the coating.

Results from numerical simulations demonstrated that the dominant criterion for the strengthening for polymer-coated scaffolds is the extent of coating infiltration into surface defects, which is maximized as the polymer fill the defect completely. As was shown when the polymer reaches the crack tip, the highest reduction of stress intensity factor K_I and applied stress σ_{yy} is achieved. It is therefore crucial to optimize the wettability and viscosity of polymeric solutions designed for dip-coating (i.e. the choice of a suitable polymer-solvent system and polymer concentration) in order to maximize the infiltration capability into the surface defects. PVA resulted in a suitable option for this application. Contact angle measurements of PVA aqueous solutions with different amount of MFC on Bioglass® surfaces were carried out, showing that the addition of MFC leads to the decrease of contact angle towards the Bioglass® surface, therefore leading to a better wettability. On the other hand the presence of fibres determines a consistent increase of viscosity in the system. Thus, a balance between these two effects must be achieved. In this work 5 to 10 wt. % of MFC fibres were found optimal. SEM observations confirmed a homogeneous distribution of the coating

on the struts surface and a sufficiently strong interface to guarantee load transfer from the struts to the coating. The influence of the cavity derived from the burning of the template on the mechanical performance was studied as well by FEM. Its presence does not cause a considerable increase of stress concentration at the strut surface and the reduction of strength is therefore ascribable to a reduction of load-bearing cross section.

Conventional sintering was found to be not suitable for fully dense bulk Bioglass® preparation; therefore, other techniques were investigated. SPS turned out to be a successful technique for the production of fully dense bulk Bioglass® samples having additionally enhanced mechanical properties. For all explored sintering routes, a sufficient level of densification could have been achieved only as the holding temperature and time reached 1050°C and 30 min, respectively. SPS performed in absence of mechanical pressure and at heating rates ranging from 100 to 300°C /min enabled the production of materials reaching nearly theoretical density and having superior mechanical properties in comparison with materials produced by conventional sintering. The main toughening contribution was identified as crack deflection at amorphous–crystalline interphase. Moreover a time–dependent crack healing process at room temperature was identified. As explanation for the latter phenomenon, the author postulates that the crystallization of an amorphous metastable phase might occur pursuant to the release of strain energy stored in the material after indent. Additionally, a deeper investigation in order to fully understand the role of atmosphere and pressure will have to be performed. As far as author's knowledge concerns, the occurrence of crack healing at room temperature has been never reported for glasses of the SiO–CaO–NaO–P_2O_5 system, and it definitely represents a very interesting finding.

DTA revealed two crystallization peaks at approximately 600 and 810°C respectively. In correspondence of T_{c1} combeite crystallized, in agreement with works of Lefebvre et al. The high temperature crystalline phase was identified as β-NaCa(PO_4) (β–rhenanite). The spectrum of β–rhenanite better fitted the experimental spectrum in comparison with silicorhenanite, which was previously reported. Nevertheless, Raman and FTIR analysis will be performed in the future in order to determine with more certainty the presence of (β–rhenanite).

The application of BNNSs as reinforcement of scaffold was considered as promising but satisfactory results were not achieved so far. However, some findings regarding BNNSs preparation were reached. Concerning the exfoliation of BNNSs, high energy sonication gave better results in comparison with ball milling. It was possible to obtain an extremely fine and stable dispersion of BNNSs, having much narrower size distribution in comparison with ball-milled BNNSs. The absence of organic solvents or thickener agents (i.e. polar/non polar polymers) renders this technique more suitable for the production of BNNS–reinforced composites by SPS.

Nevertheless, prior to extensive clinical trials, it is necessary to conduct studies of static and dynamic response of these materials in simulated physiological environments, in order to assay their reliability and that the mechanical properties do not degrade over time.

References

[1] R. R. Pelker and G. E. Friedlaender, “Biomechanical aspects of bone autografts and allografts.,” *Orthop. Clin. North Am.*, vol. 18, no. 2, pp. 235–9, Apr. 1987.

[2] E. M. Younger and M. W. Chapman, “Morbidity at bone graft donor sites.,” *J. Orthop. Trauma*, vol. 3, no. 3, pp. 192–5, Jan. 1989.

[3] L. Zhang, J. Hu, and K. A. Athanasiou, “The role of tissue engineering in articular cartilage repair and regeneration.,” *Crit. Rev. Biomed. Eng.*, vol. 37, no. 1–2, pp. 1–57, Jan. 2009.

[4] S. Sundelacruz and D. L. Kaplan, “Stem cell- and scaffold-based tissue engineering approaches to osteochondral regenerative medicine,” *Semin. Cell Dev. Biol.*, vol. 20, no. 6, pp. 646–655, Aug. 2009.

[5] M. Navarro, A. Michiardi, O. Castaño, and J. A. Planell, “Biomaterials in orthopaedics.,” *J. R. Soc. Interface*, vol. 5, no. 27, pp. 1137–58, Oct. 2008.

[6] L. L. Hench and J. Wilson, “Surface-active biomaterials.,” *Science*, vol. 226, no. 4675, pp. 630–6, Nov. 1984.

[7] L. L. Hench, “The story of Bioglass.,” *J. Mater. Sci. Mater. Med.*, vol. 17, no. 11, pp. 967–78, Nov. 2006.

[8] *Bioactive Glasses*. Elsevier, 2011.

[9] B. A. Allo, D. O. Costa, S. J. Dixon, K. Mequanint, and A. S. Rizkalla, “Bioactive and biodegradable nanocomposites and hybrid biomaterials for bone regeneration.,” *J. Funct. Biomater.*, vol. 3, no. 2, pp. 432–63, Jan. 2012.

[10] B. A. Allo, D. O. Costa, S. J. Dixon, K. Mequanint, and A. S. Rizkalla, “Bioactive and biodegradable nanocomposites and hybrid biomaterials for bone regeneration.,” *J. Funct. Biomater.*, vol. 3, no. 2, pp. 432–63, Jan. 2012.

[11] E. Hamed, I. Jasiuk, A. Yoo, Y. Lee, and T. Liszka, “Multi-scale modelling of elastic moduli of trabecular bone.,” *J. R. Soc. Interface*, vol. 9, no. 72, pp. 1654–73, Jul. 2012.

[12] P. Nooeaid, V. Salih, J. P. Beier, and A. R. Boccaccini, “Osteochondral tissue engineering: scaffolds, stem cells and applications.,” *J. Cell. Mol. Med.*, vol. 16, no. 10, pp. 2247–70, Oct. 2012.

[13] D. W. Hutmacher, “Scaffolds in tissue engineering bone and cartilage.,” *Biomaterials*, vol. 21, no. 24, pp. 2529–43, Dec. 2000.

[14] S. Bose, M. Roy, and A. Bandyopadhyay, “Recent advances in bone tissue engineering scaffolds.,” *Trends Biotechnol.*, vol. 30, no. 10, pp. 546–54, Oct. 2012.

[15] G. Kaur, O. P. Pandey, K. Singh, D. Homa, B. Scott, and G. Pickrell, "A review of bioactive glasses: Their structure, properties, fabrication and apatite formation," *J. Biomed. Mater. Res. Part A*, vol. 102, no. 1, pp. 254–274, Jan. 2014.

[16] T. Dvir, B. P. Timko, D. S. Kohane, and R. Langer, "Nanotechnological strategies for engineering complex tissues.," *Nat. Nanotechnol.*, vol. 6, no. 1, pp. 13–22, Jan. 2011.

[17] L. L. Hench, "Bioceramics: From Concept to Clinic," *J. Am. Ceram. Soc.*, vol. 74, no. 7, pp. 1487–1510, Jul. 1991.

[18] L. L. Hench, "Bioceramics," *J. Am. Ceram. Soc.*, vol. 81, no. 7, pp. 1705–1728, Jan. 2005.

[19] J. R. Jones, "Review of bioactive glass: from Hench to hybrids.," *Acta Biomater.*, vol. 9, no. 1, pp. 4457–86, 2013.

[20] A. A. Gorustovich, J. A. Roether, and A. R. Boccaccini, "Effect of bioactive glasses on angiogenesis: a review of in vitro and in vivo evidences.," *Tissue Eng. Part B. Rev.*, vol. 16, no. 2, pp. 199–207, Apr. 2010.

[21] G. Jell and M. M. Stevens, "Gene activation by bioactive glasses.," *J. Mater. Sci. Mater. Med.*, vol. 17, no. 11, pp. 997–1002, 2006.

[22] M. Bellantone, N. J. Coleman, and L. L. Hench, "Bacteriostatic action of a novel four-component bioactive glass.," *J. Biomed. Mater. Res.*, vol. 51, no. 3, pp. 484–90, Sep. 2000.

[23] C. Wu, Y. Zhou, M. Xu, P. Han, L. Chen, J. Chang, and Y. Xiao, "Copper-containing mesoporous bioactive glass scaffolds with multifunctional properties of angiogenesis capacity, osteostimulation and antibacterial activity.," *Biomaterials*, vol. 34, no. 2, pp. 422–33, Jan. 2013.

[24] E. Gentleman, Y. C. Fredholm, G. Jell, N. Lotfibakhshaiesh, M. D. O'Donnell, R. G. Hill, and M. M. Stevens, "The effects of strontium-substituted bioactive glasses on osteoblasts and osteoclasts in vitro," *Biomaterials*, vol. 31, no. 14, pp. 3949–3956, May 2010.

[25] A. A. Gorustovich, J. M. P. López, M. B. Guglielmotti, and R. L. Cabrini, "Biological performance of boron-modified bioactive glass particles implanted in rat tibia bone marrow.," *Biomed. Mater.*, vol. 1, no. 3, pp. 100–5, Sep. 2006.

[26] A. Tilocca, "The initial stages of bioglass dissolution: a Car-Parrinello molecular-dynamics study of the glass-water interface," *Proc. R. Soc. A Math. Phys. Eng. Sci.*, vol. 467, no. 2131, pp. 2102–2111, 2011.

[27] A. Martínez, I. Izquierdo-Barba, and M. Vallet-Regí, "Bioactivity of a CaO–SiO 2 Binary Glasses System," *Chem. Mater.*, vol. 12, no. 10, pp. 3080–3088, Oct. 2000.

[28] Y. Minaberry and M. Jobbágy, "Macroporous bioglass scaffolds prepared by coupling sol-gel with freeze drying," *Chem. Mater.*, vol. 23, no. 9, pp. 2327–2332, 2011.

[29] L.-C. Gerhardt and A. R. Boccaccini, "Bioactive Glass and Glass-Ceramic Scaffolds for Bone Tissue Engineering," *Materials (Basel).*, vol. 3, no. 7, pp. 3867–3910, 2010.

[30] “L.J. Gibson and M.F. Ashby, Cellular solids: Structure & properties, Oxford: Pergamon Press, 1988,” *Adv. Polym. Technol.*, vol. 9, no. 2, pp. 165–166, Jan. 1989.

[31] L. Lefebvre, L. Gremillard, J. Chevalier, R. Zenati, and D. Bernache-Assolant, “Sintering behaviour of 45S5 bioactive glass,” *Acta Biomater.*, vol. 4, no. 6, pp. 1894–1903, 2008.

[32] O. Bretcanu, X. Chatzistavrou, K. Paraskevopoulos, R. Conradt, I. Thompson, and A. R. Boccaccini, “Sintering and crystallisation of 45S5 Bioglass powder,” *J. Eur. Ceram. Soc.*, vol. 29, no. 16, pp. 3299–3306, 2009.

[33] L. Lefebvre, J. Chevalier, L. Gremillard, R. Zenati, G. Thollet, D. Bernache-Assolant, and a. Govin, “Structural transformations of bioactive glass 45S5 with thermal treatments,” *Acta Mater.*, vol. 55, no. 10, pp. 3305–3313, 2007.

[34] P. Gentile, M. Mattioli-Belmonte, V. Chiono, C. Ferretti, F. Baino, C. Tonda-Turo, C. Vitale-Brovarone, I. Pashkuleva, R. L. Reis, and G. Ciardelli, “Bioactive glass/polymer composite scaffolds mimicking bone tissue,” *J. Biomed. Mater. Res. Part A*, vol. 100A, no. 10, pp. 2654–2667, 2012.

[35] H. E. Kissinger, “Variation of peak temperature with heating rate in differential thermal analysis,” *J. Res. Natl. Bur. Stand. (1934).*, vol. 57, no. 4, p. 217, 1956.

[36] D. C. Clupper and L. L. Hench, “Crystallization kinetics of tape cast bioactive glass 45S5,” *J. Non. Cryst. Solids*, vol. 318, no. 1–2, pp. 43–48, 2003.

[37] Y. Liu, Q. Xiang, Y. Tan, and X. Sheng, “Nucleation and growth of needle-like fluorapatite crystals in bioactive glass–ceramics,” *J. Non. Cryst. Solids*, vol. 354, no. 10–11, pp. 938–944, 2008.

[38] S. Kashyap, K. Griep, and J. a. Nychka, “Crystallization kinetics, mineralization and crack propagation in partially crystallized bioactive glass 45S5,” *Mater. Sci. Eng. C*, vol. 31, no. 4, pp. 762–769, 2011.

[39] D. Bellucci, V. Cannillo, and A. Sola, “An overview of the effects of thermal processing on bioactive glasses,” *Sci. Sinter.*, vol. 42, no. 3, pp. 307–320, 2010.

[40] A. Karamanov, I. Avramov, L. Arrizza, R. Pascova, and I. Gutzow, “Variation of Avrami parameter during non-isothermal surface crystallization of glass powders with different sizes,” *J. Non. Cryst. Solids*, vol. 358, no. 12–13, pp. 1486–1490, 2012.

[41] X. Chatzistavrou, T. Zorba, K. Chrissafis, G. Kaimakamis, E. Kontonasaki, P. Koidis, and K. M. Paraskevopoulos, “Influence of particle size on the crystallization process and the bioactive behaviour of a bioactive glass system,” *J. Therm. Anal. Calorim.*, vol. 85, no. 2, pp. 253–259, 2006.

[42] “Cellular Ceramics: Structure, Manufacturing, Properties and Applications: Michael Scheffler, Paolo Colombo: 9783527313204: Amazon.com: Books.” [Online]. Available: http://www.amazon.com/Cellular-Ceramics-Manufacturing-Properties-Applications/dp/3527313206. [Accessed: 06-Oct-2015].

[43] “Handbook of Manufacturing Processes: How Products, Components and Materials Are Made: Amazon.it: James G. Bralla: Libri in altre lingue.” [Online]. Available: http://www.amazon.it/Handbook-Manufacturing-Processes-Components-Materials/dp/0831131799. [Accessed: 06-Oct-2015].

[44] R. S. Barnes, “The formation of internal gas bubbles in solids,” *J. Nucl. Energy*, vol. 5, no. 3–4, pp. 301–319, Jan. 1957.

[45] Q. Z. Chen, I. D. Thompson, and A. R. Boccaccini, “45S5 Bioglass-derived glass-ceramic scaffolds for bone tissue engineering.,” *Biomaterials*, vol. 27, no. 11, pp. 2414–25, Apr. 2006.

[46] O. Lyckfeldt and J. M. F. Ferreira, “Processing of porous ceramics by ‘starch consolidation,’” *J. Eur. Ceram. Soc.*, vol. 18, no. 2, pp. 131–140, Jan. 1998.

[47] Minnear, “Processing of foamed ceramics,” *Ceram. Trans.*, 1991.

[48] H. R. Ramay and M. Zhang, “Preparation of porous hydroxyapatite scaffolds by combination of the gel-casting and polymer sponge methods,” *Biomaterials*, vol. 24, no. 19, pp. 3293–3302, Aug. 2003.

[49] P. Sepulveda, J. G. Binner, S. O. Rogero, O. Z. Higa, and J. C. Bressiani, “Production of porous hydroxyapatite by the gel-casting of foams and cytotoxic evaluation.,” *J. Biomed. Mater. Res.*, vol. 50, no. 1, pp. 27–34, Apr. 2000.

[50] Z. Živcová, E. Gregorová, W. Pabst, D. S. Smith, A. Michot, and C. Poulier, “Thermal conductivity of porous alumina ceramics prepared using starch as a pore-forming agent,” *J. Eur. Ceram. Soc.*, vol. 29, no. 3, pp. 347–353, Feb. 2009.

[51] P. Sepulveda and J. G. . Binner, “Processing of cellular ceramics by foaming and in situ polymerisation of organic monomers,” *J. Eur. Ceram. Soc.*, vol. 19, no. 12, pp. 2059–2066, Oct. 1999.

[52] F. S. Ortega, F. A. O. Valenzuela, C. H. Scuracchio, and V. C. Pandolfelli, “Alternative gelling agents for the gelcasting of ceramic foams,” *J. Eur. Ceram. Soc.*, vol. 23, no. 1, pp. 75–80, Jan. 2003.

[53] “The Physics of Foams: Denis Weaire, Stefan Hutzler: 9780198510970: Amazon.com: Books.” [Online]. Available: http://www.amazon.com/The-Physics-Foams-Denis-Weaire/dp/0198510977. [Accessed: 06-Oct-2015].

[54] J. C. Maxwell, “On the calculation of the equilibrium and stiffness of frames.,” *Philos Mag*, no. 27, pp. 294–99, 1864.

[55] A. Roberts and E. Garboczi, “Elastic moduli of model random three-dimensional closed-cell cellular solids,” no. 1, pp. 1–13, 2000.

[56] A. P. Roberts and E. J. Garboczi, “Elastic properties of model random three-dimensional open-cell solids,” *J. Mech. Phys. Solids*, vol. 50, no. 1, pp. 33–55, 2002.

[57] J. Gubicza, a. Juhasz, P. Tasnadi, P. Arato, and G. Vörös, “Determination of the hardness and elastic modulus from continuous vickers indentation testing,” *J. Mater. Sci.*, vol. 31, pp. 3109–3114, 1996.

[58] L. J. Gibson, “Biomechanics of cellular solids,” *J. Biomech.*, vol. 38, no. 3, pp. 377–399, 2005.

[59] J. L. Zhang and Z. X. Lu, “Numerical modelling of the compression process of elastic open-cell foams,” *Chinese J. Aeronaut.*, vol. 20, no. 3, pp. 215–222, 2007.

[60] A. Ajdari, “Mechanical behaviour of cellular structures : a finite element study,” *Mech. Eng.*, 2008.

[61] Y. X. Gan, C. Chen, and Y. P. Shen, “Three-dimensional modelling of the mechanical property of linearly elastic open cell foams,” *Int. J. Solids Struct.*, vol. 42, no. 26, pp. 6628–6642, 2005.

[62] J. Bock and A. M. Jacobi, “Geometric classification of open-cell metal foams using X-ray micro-computed tomography,” *Mater. Charact.*, vol. 75, pp. 35–43, 2013.

[63] J. S. Bauer, I. Sidorenko, D. Mueller, T. Baum, A. S. Issever, F. Eckstein, E. J. Rummeny, T. M. Link, and C. W. Raeth, “Prediction of bone strength by μCT and MDCT-based finite-element-models: how much spatial resolution is needed,” *Eur. J. Radiol.*, vol. 83, no. 1, pp. e36–42, 2014.

[64] W. Y. Jang, A. M. Kraynik, and S. Kyriakides, “On the microstructure of open-cell foams and its effect on elastic properties,” *Int. J. Solids Struct.*, vol. 45, no. 7–8, pp. 1845–1875, 2008.

[65] C. D’Angelo, A. Ortona, and P. Colombo, “Finite element analysis of reticulated ceramics under compression,” *Acta Mater.*, vol. 60, no. 19, pp. 6692–6702, 2012.

[66] M. L. Bouxsein, S. K. Boyd, B. A. Christiansen, R. E. Guldberg, K. J. Jepsen, and R. Müller, “Guidelines for assessment of bone microstructure in rodents using micro-computed tomography.,” *J. Bone Miner. Res.*, vol. 25, no. 7, pp. 1468–86, 2010.

[67] A. Laib, O. Barou, L. Vico, M. H. Lafage-Proust, C. Alexandre, and P. Rügsegger, “3D micro-computed tomography of trabecular and cortical bone architecture with application to a rat model of immobilisation osteoporosis,” *Med. Biol. Eng. Comput.*, vol. 38, no. 3, pp. 326–332, May 2000.

[68] C. D’Angelo, A. Ortona, and P. Colombo, “Influence of the loading direction on the mechanical behaviour of ceramic foams and lattices under compression,” *Acta Mater.*, vol. 61, no. 14, pp. 5525–5534, 2013.

[69] D. J. Duval, S. H. Risbud, and J. F. Shackelford, *Ceramic and Glass Materials*. 2008.

[70] I. Dlouhý and A. R. Boccaccini, “Fracture behaviour of brittle (glass) matrix composites,” vol. 482, pp. 115–120, 2005.

[71] J. Nychka, D. Li, and B. Alexander, “In vitro bioactivity of 45S5 bioactive glass as a function of indentation load,” *J. Mech. Behav. Biomed. Mater.*, vol. 1, no. 3, pp. 243–251, 2008.

[72] D. Li, F. Yang, and J. Nychka, “Indentation-induced residual stresses in 45S5 bioglass and the stress effect on the material dissolution,” *Eng. Fract. Mech.*, vol. 75, no. 17, pp. 4898–4908, 2008.

[73] M. Erol and A. R. Boccaccini, *Bioactive Glasses*. Elsevier, 2011.

[74] I. D. Thompson and L. L. Hench, “Mechanical properties of bioactive glasses, glass-ceramics and composites.,” *Proc. Inst. Mech. Eng. H.*, vol. 212, no. 2, pp. 127–36, Jan. 1998.

[75] “An Introduction to Bioceramics (2nd Edition): Larry L Hench: 9781908977151: Amazon.com: Books.” [Online]. Available: http://www.amazon.com/An-Introduction-Bioceramics-2nd-Edition/dp/1908977159. [Accessed: 07-Oct-2015].

[76] O. P. Filho, G. P. La Torre, and L. L. Hench, “Effect of crystallization on apatite-layer formation of bioactive glass 45S5,” *J. Biomed. Mater. Res.*, vol. 30, no. 4, pp. 509–514, Apr. 1996.

[77] C. . Hernandez, G. . Beaupré, T. . Keller, and D. . Carter, “The influence of bone volume fraction and ash fraction on bone strength and modulus,” *Bone*, vol. 29, no. 1, pp. 74–78, Jul. 2001.

[78] T. M. Keaveny, E. F. Morgan, G. L. Niebur, and O. C. Yeh, “Biomechanics of trabecular bone.,” *Annu. Rev. Biomed. Eng.*, vol. 3, pp. 307–33, Jan. 2001.

[79] K. Rezwan, Q. Z. Chen, J. J. Blaker, and A. R. Boccaccini, “Biodegradable and bioactive porous polymer/inorganic composite scaffolds for bone tissue engineering.,” *Biomaterials*, vol. 27, no. 18, pp. 3413–31, Jun. 2006.

[80] S.-S. Sun, H.-L. Ma, C.-L. Liu, C.-H. Huang, C.-K. Cheng, and H.-W. Wei, “Difference in femoral head and neck material properties between osteoarthritis and osteoporosis,” *Clin. Biomech.*, vol. 23, pp. S39–S47, Jan. 2008.

[81] A. Nazarian, D. von Stechow, D. Zurakowski, R. Müller, and B. D. Snyder, “Bone volume fraction explains the variation in strength and stiffness of cancellous bone affected by metastatic cancer and osteoporosis.,” *Calcif. Tissue Int.*, vol. 83, no. 6, pp. 368–79, Dec. 2008.

[82] V. Karageorgiou and D. Kaplan, “Porosity of 3D biomaterial scaffolds and osteogenesis,” *Biomaterials*, vol. 26, no. 27, pp. 5474–5491, 2005.

[83] T. L. Anderson and T. L. Anderson, *Fracture Mechanics: Fundamentals and Applications, Second Edition*. CRC Press, 1994.

[84] M. Yoda, “Subcritical crack growth of glass,” *Eng. Fract. Mech.*, vol. 28, no. 1, pp. 77–84, Jan. 1987.

[85] A. Tilocca and A. N. Cormack, “Modelling the water-bioglass interface by ab initio molecular dynamics simulations.,” *ACS Appl. Mater. Interfaces*, vol. 1, no. 6, pp. 1324–33, Jun. 2009.

[86] G. D. Quinn and R. C. Bradt, “On the Vickers Indentation Fracture Toughness Test,” *J. Am. Ceram. Soc.*, vol. 90, no. 3, pp. 673–680, Mar. 2007.

[87] W. C. Oliver and G. M. Pharr, “Measurement of hardness and elastic modulus by instrumented indentation: Advances in understanding and refinements to methodology,” *J. Mater. Res.*, vol. 19, no. 01, pp. 3–20, 2004.

[88] “Oliver, Pharr - 1992 - An improved technique for determining hardness and elastic modulus using load and displacement.pdf.” .

[89] A. R. Franco Jr., G. Pintaúde, A. Sinatora, C. E. Pinedo, and A. P. Tschiptschin, “The use of a vickers indenter in depth sensing indentation for measuring elastic modulus and vickers hardness,” *Mater. Res.*, vol. 7, no. 3, pp. 483–491, Sep. 2004.

[90] A. . Boccaccini, R. . Rawlings, and I. Dlouhý, “Reliability of the chevron-notch technique for fracture toughness determination in glass,” *Mater. Sci. Eng. A*, vol. 347, no. 1–2, pp. 102–108, Apr. 2003.

[91] L. J. Gibson and M. F. Ashby, “The Mechanics of Three-Dimensional Cellular Materials,” *Proc. R. Soc. A Math. Phys. Eng. Sci.*, vol. 382, no. 1782, pp. 43–59, Jul. 1982.

[92] D. J. Green, “An Introduction to the Mechanical Properties of Ceramics,” p. 336, 1998.

[93] S. K. Maiti, L. J. Gibson, and M. F. Ashby, “Deformation and energy absorption diagrams for cellular solids,” *Acta Metall.*, vol. 32, no. 11, pp. 1963–1975, Nov. 1984.

[94] H. Hagiwara and D. J. Green, “Elastic Behaviour of Open-Cell Alumina,” *J. Am. Ceram. Soc.*, vol. 70, no. 11, pp. 811–815, Nov. 1987.

[95] H. M. Princen and P. Levinson, “The surface area of Kelvin’s minimal tetrakaidecahedron: The ideal foam cell,” *J. Colloid Interface Sci.*, vol. 120, no. 1, pp. 172–175, Nov. 1987.

[96] M. J. M. John B. Wachtman, W. Roger Cannon, *Mechanical Properties of Ceram*. 2009.

[97] G. Yang, X. Yang, L. Zhang, M. Lin, X. Sun, X. Chen, and Z. Gou, “Counterionic biopolymers-reinforced bioactive glass scaffolds with improved mechanical properties in wet state,” *Mater. Lett.*, vol. 75, pp. 80–83, May 2012.

[98] D. Mohamad Yunos, O. Bretcanu, and A. R. Boccaccini, “Polymer-bioceramic composites for tissue engineering scaffolds,” *J. Mater. Sci.*, vol. 43, no. 13, pp. 4433–4442, 2008.

[99] M. Peroglio, L. Gremillard, J. Chevalier, L. Chazeau, C. Gauthier, and T. Hamaide, “Toughening of bio-ceramics scaffolds by polymer coating,” *J. Eur. Ceram. Soc.*, vol. 27, no. 7, pp. 2679–2685, 2007.

[100] C. Xu, P. Su, X. Chen, Y. Meng, W. Yu, A. P. Xiang, and Y. Wang, "Biocompatibility and osteogenesis of biomimetic Bioglass-Collagen-Phosphatidylserine composite scaffolds for bone tissue engineering.," *Biomaterials*, vol. 32, no. 4, pp. 1051–8, Feb. 2011.

[101] V. Mouriño, P. Newby, and A. R. Boccaccini, "Preparation and Characterization of Gallium Releasing 3-D Alginate Coated 45S5 Bioglass® Based Scaffolds for Bone Tissue Engineering," *Adv. Eng. Mater.*, vol. 12, no. 7, pp. B283–B291, Jul. 2010.

[102] X. Zhang, J. Zhang, and B. Shi, "Mesoporous bioglass/silk fibroin scaffolds as a drug delivery system: Fabrication, drug loading and release in vitro and repair calvarial defects in vivo," *J. Wuhan Univ. Technol. Sci. Ed.*, vol. 29, no. 2, pp. 401–406, Apr. 2014.

[103] A. L. Metze, A. Grimm, P. Nooeaid, J. A. Roether, J. Hum, P. J. Newby, D. W. Schubert, and A. R. Boccaccini, "Gelatin Coated 45S5 Bioglass®-Derived Scaffolds for Bone Tissue Engineering," *Key Eng. Mater.*, vol. 541, pp. 31–39, Feb. 2013.

[104] Q. Yao, P. Nooeaid, R. Detsch, J. A. Roether, Y. Dong, O.-M. Goudouri, D. W. Schubert, and A. R. Boccaccini, "Bioglass®/chitosan-polycaprolactone bilayered composite scaffolds intended for osteochondral tissue engineering.," *J. Biomed. Mater. Res. A*, vol. 102, no. 12, pp. 4510–8, Dec. 2014.

[105] D. M. Yunos, Z. Ahmad, V. Salih, and A. R. Boccaccini, "Stratified scaffolds for osteochondral tissue engineering applications: electrospun PDLLA nanofibre coated Bioglass®-derived foams.," *J. Biomater. Appl.*, vol. 27, no. 5, pp. 537–51, Jan. 2013.

[106] Q. Yao, P. Nooeaid, J. A. Roether, Y. Dong, Q. Zhang, and A. R. Boccaccini, "Bioglass®-based scaffolds incorporating polycaprolactone and chitosan coatings for controlled vancomycin delivery," *Ceram. Int.*, vol. 39, no. 7, pp. 7517–7522, Sep. 2013.

[107] S.-I. Roohani-Esfahani, S. Nouri-Khorasani, Z. Lu, R. Appleyard, and H. Zreiqat, "The influence hydroxyapatite nanoparticle shape and size on the properties of biphasic calcium phosphate scaffolds coated with hydroxyapatite-PCL composites.," *Biomaterials*, vol. 31, no. 21, pp. 5498–509, Jul. 2010.

[108] W. Li, P. Nooeaid, J. A. Roether, D. W. Schubert, and A. R. Boccaccini, "Preparation and characterization of vancomycin releasing PHBV coated 45S5 Bioglass®-based glass–ceramic scaffolds for bone tissue engineering," *J. Eur. Ceram. Soc.*, vol. 34, no. 2, pp. 505–514, Feb. 2014.

[109] F. Martínez-Vázquez, A. Pajares, F. Guiberteau, and P. Miranda, "Effect of Polymer Infiltration on the Flexural Behaviour of β-Tricalcium Phosphate Robocast Scaffolds," *Materials (Basel).*, vol. 7, no. 5, pp. 4001–4018, May 2014.

[110] L. E. Scriven, "Physics and Applications of DIP Coating and Spin Coating," *MRS Proc.*, vol. 121, p. 717, Feb. 2011.

[111] V. Levich, *Physicochemical hydrodynamics.* Englewood Cliffs N.J.: Prentice-Hall, 1962.

[112] B. Deri͡agin, *Film coating theory.* Focal Press, 1964.

[113] T. Young, “An Essay on the Cohesion of Fluids,” *Philos. Trans. R. Soc. London*, vol. 95, pp. 65–87, Jan. 1805.

[114] J. H. Snoeijer and B. Andreotti, “A microscopic view on contact angle selection,” *Phys. Fluids*, vol. 20, no. 5, p. 057101, May 2008.

[115] J. J. Blaker, V. Maquet, A. R. Boccaccini, R. Jérôme, and A. Bismarck, “Wetting of bioactive glass surfaces by poly(alpha-hydroxyacid) melts: interaction between Bioglass (R) and biodegradable polymers,” *e-Polymers*, vol. 23, Apr. 2005.

[116] W. Li, M.-I. Pastrama, Y. Ding, K. Zheng, C. Hellmich, and A. R. Boccaccini, “Ultrasonic elasticity determination of 45S5 Bioglass®-based scaffolds: Influence of polymer coating and crosslinking treatment,” *J. Mech. Behav. Biomed. Mater.*, vol. 40, pp. 85–94, 2014.

[117] Z. Q. Gu, J. M. Xiao, and X. H. Zhang, “The development of artificial articular cartilage--PVA-hydrogel.,” *Biomed. Mater. Eng.*, vol. 8, no. 2, pp. 75–81, Jan. 1998.

[118] C.-J. Kim and P. I. Lee, “Composite Poly(vinyl alcohol) Beads for Controlled Drug Delivery,” *Pharm. Res.*, vol. 9, no. 1, pp. 10–16.

[119] S. M. Tadavarthy, J. H. Moller, and K. Amplatz, “Polyvinyl alcohol (Ivalon)--a new embolic material.,” *Am. J. Roentgenol. Radium Ther. Nucl. Med.*, vol. 125, no. 3, pp. 609–16, Nov. 1975.

[120] R. A. Lang, P. M. Grüntzig, C. Weisgerber, C. Weis, E. K. Odermatt, and M. H. Kirschner, “Polyvinyl alcohol gel prevents abdominal adhesion formation in a rabbit model,” *Fertil. Steril.*, vol. 88, no. 4, pp. 1180–1186, Oct. 2007.

[121] N. Lavoine, I. Desloges, A. Dufresne, and J. Bras, “Microfibrillated cellulose – Its barrier properties and applications in cellulosic materials: A review,” *Carbohydr. Polym.*, vol. 90, no. 2, pp. 735–764, 2012.

[122] T. Miyamoto, S. Takahashi, H. Ito, H. Inagaki, and Y. Noishiki, “Tissue biocompatibility of cellulose and its derivatives,” *J. Biomed. Mater. Res.*, vol. 23, no. 1, pp. 125–133, Jan. 1989.

[123] Y. Ikada, “Surface modification of polymers for medical applications,” *Biomaterials*, vol. 15, no. 10, pp. 725–736, Aug. 1994.

[124] T. Hayashi, “Biodegradable polymers for biomedical uses,” *Prog. Polym. Sci.*, vol. 19, no. 4, pp. 663–702, Jan. 1994.

[125] I. Siró and D. Plackett, “Microfibrillated cellulose and new nanocomposite materials: a review,” *Cellulose*, vol. 17, no. 3, pp. 459–494, 2010.

[126] M. Pääkkö, M. Ankerfors, H. Kosonen, A. Nykänen, S. Ahola, M. Osterberg, J. Ruokolainen, J. Laine, P. T. Larsson, O. Ikkala, and T. Lindström, “Enzymatic hydrolysis combined with mechanical shearing and high-pressure homogenization for nanoscale cellulose fibrils and strong gels.,” *Biomacromolecules*, vol. 8, no. 6, pp. 1934–41, Jun. 2007.

[127] S. J. Eichhorn and R. J. Young, "The Young's modulus of a microcrystalline cellulose," *Cellulose*, vol. 8, no. 3, pp. 197–207.

[128] N. Lavoine, I. Desloges, A. Dufresne, and J. Bras, "Microfibrillated cellulose - its barrier properties and applications in cellulosic materials: a review.," *Carbohydr. Polym.*, vol. 90, no. 2, pp. 735–64, Oct. 2012.

[129] G. Siqueira, J. Bras, and A. Dufresne, "Cellulosic Bionanocomposites: A Review of Preparation, Properties and Applications," *Polymers (Basel).*, vol. 2, no. 4, pp. 728–765, 2010.

[130] S. Virtanen, J. Vartianen, H. Setälä, T. Tammelin, and S. Vuoti, "Modified nanofibrillated cellulose–polyvinyl alcohol films with improved mechanical performance," *RSC Adv.*, vol. 4, no. 22, p. 11343, Feb. 2014.

[131] T. Zimmermann, N. Bordeanu, and E. Strub, "Properties of nanofibrillated cellulose from different raw materials and its reinforcement potential," *Carbohydr. Polym.*, vol. 79, no. 4, pp. 1086–1093, 2010.

[132] T. Zimmermann, E. Pöhler, and T. Geiger, "Cellulose Fibrils for Polymer Reinforcement," *Adv. Eng. Mater.*, vol. 6, no. 9, pp. 754–761, Sep. 2004.

[133] J. Leitner, B. Hinterstoisser, M. Wastyn, J. Keckes, and W. Gindl, "Sugar beet cellulose nanofibril-reinforced composites," *Cellulose*, vol. 14, no. 5, pp. 419–425, 2007.

[134] B. Wang, M. Sain, and K. Oksman, "Study of Structural Morphology of Hemp Fibre from the Micro to the Nanoscale," *Appl. Compos. Mater.*, vol. 14, no. 2, pp. 89–103, Jan. 2007.

[135] A. Mihranyan, "Viscoelastic properties of cross-linked polyvinyl alcohol and surface-oxidized cellulose whisker hydrogels," *Cellulose*, vol. 20, no. 3, pp. 1369–1376, 2013.

[136] M. Roohani, Y. Habibi, N. M. Belgacem, G. Ebrahim, A. N. Karimi, and A. Dufresne, "Cellulose whiskers reinforced polyvinyl alcohol copolymers nanocomposites," *Eur. Polym. J.*, vol. 44, no. 8, pp. 2489–2498, Aug. 2008.

[137] J. Lu, T. Wang, and L. T. Drzal, "Preparation and properties of microfibrillated cellulose polyvinyl alcohol composite materials," *Compos. Part A Appl. Sci. Manuf.*, vol. 39, no. 5, pp. 738–746, 2008.

[138] S.-Y. Lee, D. J. Mohan, I.-A. Kang, G.-H. Doh, S. Lee, and S. O. Han, "Nanocellulose reinforced PVA composite films: Effects of acid treatment and filler loading," *Fibres Polym.*, vol. 10, no. 1, pp. 77–82, Mar. 2009.

[139] Q. Cheng, S. Wang, and T. G. Rials, "Poly(vinyl alcohol) nanocomposites reinforced with cellulose fibrils isolated by high intensity ultrasonication," *Compos. Part A Appl. Sci. Manuf.*, vol. 40, no. 2, pp. 218–224, Feb. 2009.

[140] J. Lu, T. Wang, and L. T. Drzal, "Preparation and properties of microfibrillated cellulose polyvinyl alcohol composite materials," *Compos. Part A Appl. Sci. Manuf.*, vol. 39, no. 5, pp. 738–746, May 2008.

[141] N. Ouali, J. Y. Cavaille, and J. Perez, “Elastic, viscoelastic and plastic behaviour of multiphase polymer blends,” *Plast. Rubber Compos. Process. Appl.*, pp. 55–60, 1991.

[142] “Sintering of Ceramics - CRC Press Book.” [Online]. Available: https://www.crcpress.com/Sintering-of-Ceramics/Rahaman/9780849372865. [Accessed: 08-Oct-2015].

[143] O. Guillon, J. Gonzalez-Julian, B. Dargatz, T. Kessel, G. Schierning, J. Räthel, and M. Herrmann, “Field-Assisted Sintering Technology/Spark Plasma Sintering: Mechanisms, Materials, and Technology Developments,” *Adv. Eng. Mater.*, vol. 16, no. 7, pp. 830–849, Jul. 2014.

[144] J. E. Garay, “Current-Activated, Pressure-Assisted Densification of Materials,” *Annu. Rev. Mater. Res.*, vol. 40, no. 1, pp. 445–468, Jun. 2010.

[145] H. B. Guo, X. Miao, Y. Chen, P. Cheang, and K. A. Khor, “Characterization of hydroxyapatite– and bioglass–316L fibre composites prepared by spark plasma sintering,” *Mater. Lett.*, vol. 58, no. 3–4, pp. 304–307, Jan. 2004.

[146] H. Porwal, M. Estili, A. Grünewald, S. Grasso, R. Detsch, C. Hu, Y. Sakka, A. R. Boccaccini, and M. J. Reece, “45S5 Bioglass(®)-MWCNT composite: processing and bioactivity.,” *J. Mater. Sci. Mater. Med.*, vol. 26, no. 6, p. 199, Jun. 2015.

[147] Q. Z. Chen, J. L. Xu, L. G. Yu, X. Y. Fang, and K. A. Khor, “Spark plasma sintering of sol–gel derived 45S5 Bioglass®-ceramics: Mechanical properties and biocompatibility evaluation,” *Mater. Sci. Eng. C*, vol. 32, no. 3, pp. 494–502, Apr. 2012.

[148] S. Grasso, R. K. Chinnam, H. Porwal, A. R. Boccaccini, and M. J. Reece, “Low temperature spark plasma sintering of 45S5 Bioglass®,” *J. Non. Cryst. Solids*, vol. 362, pp. 25–29, Feb. 2013.

[149] H. Porwal, S. Grasso, L. Cordero-Arias, C. Li, A. R. Boccaccini, and M. J. Reece, “Processing and bioactivity of 45S5 Bioglass®-graphene nanoplatelets composites,” *J. Mater. Sci. Mater. Med.*, vol. 25, no. 6, pp. 1403–1413, Feb. 2014.

[150] J. Zhang, C. Jia, Z. Jia, J. Ladegard, Y. Gu, and J. Nie, “Strengthening mechanisms in carbon nanotube reinforced bioglass composites,” *Front. Chem. Sci. Eng.*, vol. 6, no. 2, pp. 126–131, 2012.

[151] J. Cho, F. Inam, M. J. Reece, Z. Chlup, I. Dlouhy, M. S. P. Shaffer, and A. R. Boccaccini, “Carbon nanotubes: do they toughen brittle matrices?,” *J. Mater. Sci.*, vol. 46, no. 14, pp. 4770–4779, 2011.

[152] A. R. Boccaccini, B. J. C. Thomas, G. Brusatin, and P. Colombo, “Mechanical and electrical properties of hot-pressed borosilicate glass matrix composites containing multi-wall carbon nanotubes,” *J. Mater. Sci.*, vol. 42, no. 6, pp. 2030–2036, Feb. 2007.

[153] C. Oshima and A. Nagashima, “Ultra-thin epitaxial films of graphite and hexagonal boron nitride on solid surfaces,” *J. Phys. Condens. Matter*, vol. 9, no. 1, p. 1, 1997.

[154] G. Ciofani, S. Danti, D. D'Alessandro, S. Moscato, and A. Menciassi, "Assessing cytotoxicity of boron nitride nanotubes: Interference with the MTT assay," *Biochem. Biophys. Res. Commun.*, vol. 394, no. 2, pp. 405–411, 2010.

[155] L. Horváth, A. Magrez, D. Golberg, C. Zhi, Y. Bando, R. Smajda, E. Horváth, L. Forró, and B. Schwaller, "In vitro investigation of the cellular toxicity of boron nitride nanotubes.," *ACS Nano*, vol. 5, no. 5, pp. 3800–10, May 2011.

[156] X. Chen, P. Wu, M. Rousseas, D. Okawa, Z. Gartner, A. Zettl, and C. R. Bertozzi, "Boron Nitride Nanotubes Are Noncytotoxic and Can Be Functionalized for Interaction with Proteins and Cells," *J. Am. Chem. Soc.*, vol. 131, no. 3, pp. 890–891, Jan. 2009.

[157] D. Lahiri, V. Singh, A. P. Benaduce, S. Seal, L. Kos, and A. Agarwal, "Boron nitride nanotube reinforced hydroxyapatite composite: Mechanical and tribological performance and in-vitro biocompatibility to osteoblasts," *J. Mech. Behav. Biomed. Mater.*, vol. 4, no. 1, pp. 44–56, 2011.

[158] Q. Weng, B. Wang, X. Wang, N. Hanagata, X. Li, D. Liu, X. Wang, X. Jiang, Y. Bando, and D. Golberg, "Highly Water-Soluble, Porous, and Biocompatible Boron Nitrides for Anticancer Drug Delivery," *ACS Nano*, vol. 8, no. 6, pp. 6123–6130, Jun. 2014.

[159] P. Tatarko, S. Grasso, H. Porwal, Z. Chlup, R. Saggar, I. Dlouhý, and M. J. Reece, "Boron nitride nanotubes as a reinforcement for brittle matrices," *J. Eur. Ceram. Soc.*, vol. 34, no. 14, pp. 3339–3349, 2014.

[160] Y. Lin and J. W. Connell, "Advances in 2D boron nitride nanostructures: nanosheets, nanoribbons, nanomeshes, and hybrids with graphene," *Nanoscale*, vol. 4, no. 22, p. 6908, 2012.

[161] C. Li, Y. Bando, C. Zhi, Y. Huang, and D. Golberg, "Thickness-dependent bending modulus of hexagonal boron nitride nanosheets.," *Nanotechnology*, vol. 20, no. 38, p. 385707, Sep. 2009.

[162] L. H. Li, Y. Chen, G. Behan, H. Zhang, M. Petravic, and A. M. Glushenkov, "Large-scale mechanical peeling of boron nitride nanosheets by low-energy ball milling," *J. Mater. Chem.*, vol. 21, no. 32, p. 11862, 2011.

[163] B.-Q. Dai and G.-L. Zhang, "A DFT study of hBN compared with graphite in forming alkali metal intercalation compounds," *Mater. Chem. Phys.*, vol. 78, no. 2, pp. 304–307, Feb. 2003.

[164] C. Suryanarayana, "Mechanical alloying and milling," *Prog. Mater. Sci.*, vol. 46, no. 1–2, pp. 1–184, 2001.

[165] N. Rathod and S. G. Hatzikiriakos, "The effect of surface energy of boron nitride on polymer processability," *Polym. Eng. Sci.*, vol. 44, no. 8, pp. 1543–1550, 2004.

[166] W. D. Harkins and F. E. Brown, "The determination of surface tension (free surface energy) and the weight of falling drops: the surface tension of water and benzene by the capillary height method.," *J. Am. Chem. Soc.*, vol. 41, no. 4, pp. 499–524, Apr. 1919.

[167] Y. Lin, T. V. Williams, T. B. Xu, W. Cao, H. E. Elsayed-Ali, and J. W. Connell, “Aqueous dispersions of few-layered and monolayered hexagonal boron nitride nanosheets from sonication-assisted hydrolysis: Critical role of water,” *J. Phys. Chem. C*, vol. 115, no. 6, pp. 2679–2685, 2011.

[168] L. H. Li, Y. Chen, G. Behan, H. Zhang, M. Petravic, and A. M. Glushenkov, “Large-scale mechanical peeling of boron nitride nanosheets by low-energy ball milling,” *J. Mater. Chem.*, vol. 21, no. 32, p. 11862, Aug. 2011.

[169] C. Shuai, Z. Han, P. Feng, C. Gao, T. Xiao, and S. Peng, “Akermanite scaffolds reinforced with boron nitride nanosheets in bone tissue engineering,” *J. Mater. Sci. Mater. Med.*, vol. 26, no. 5, p. 188, Apr. 2015.

[170] J. R. Jones, “Review of bioactive glass: from Hench to hybrids.,” *Acta Biomater.*, vol. 9, no. 1, pp. 4457–86, Jan. 2013.

[171] C. C. Sun, “True density of microcrystalline cellulose.,” *J. Pharm. Sci.*, vol. 94, no. 10, pp. 2132–4, Oct. 2005.

[172] R. Zsigmondy, “Kolloidchemie: Ein Lehrbuch (German Edition),” 1920.

[173] D. F. Swinehart, “The Beer-Lambert Law,” *J. Chem. Educ.*, vol. 39, no. 7, p. 333, Jul. 1962.

[174] J. N. Coleman, M. Lotya, A. O’Neill, S. D. Bergin, P. J. King, U. Khan, K. Young, A. Gaucher, S. De, R. J. Smith, I. V Shvets, S. K. Arora, G. Stanton, H.-Y. Kim, K. Lee, G. T. Kim, G. S. Duesberg, T. Hallam, J. J. Boland, J. J. Wang, J. F. Donegan, J. C. Grunlan, G. Moriarty, A. Shmeliov, R. J. Nicholls, J. M. Perkins, E. M. Grieveson, K. Theuwissen, D. W. McComb, P. D. Nellist, and V. Nicolosi, “Two-dimensional nanosheets produced by liquid exfoliation of layered materials.,” *Science*, vol. 331, no. 6017, pp. 568–571, 2011.

[175] “BS EN 843-1:1995 - Advanced technical ceramics. Monolithic ceramics. Mechanical properties at room temperature. Determination of flexural strength.” .

[176] “ASTM E92 - 82(2003)e2 Standard Test Method for Vickers Hardness of Metallic Materials (Withdrawn 2010).” .

[177] G. R. Anstis, P. Chantikul, B. R. Lawn, and D. B. Marshall, “A Critical Evaluation of Indentation Techniques for Measuring Fracture Toughness: I, Direct Crack Measurements,” *J. Am. Ceram. Soc.*, vol. 64, no. 9, pp. 533–538, Sep. 1981.

[178] K. R. Brown, *Chevron-notch Fracture Test Experience: Metals and Non-metals*. ASTM International, 1992.

[179] “BS EN 843-2:2006 - Advanced technical ceramics. Mechanical properties of monolithic ceramics at room temperature. Determination of Young’s modulus, shear modulus and Poisson's ratio.” .

[180] C. a. Klein, “Characteristic strength, Weibull modulus, and failure probability of fused silica glass,” *Opt. Eng.*, vol. 48, no. 11, p. 113401, 2009.

[181] E. A. Elsayed, *Reliability Engineering*. John Wiley & Sons, 2012.

[182] L. Řehořek, Z. Chlup, D. Meng, D. M. Yunos, a. R. Boccaccini, and I. Dlouhý, "Response of 45S5 Bioglass® foams to tensile loading," *Ceram. Int.*, vol. 39, no. 7, pp. 8015–8020, 2013.

[183] P. Kenesei, "The influence of cell-size distribution on the plastic deformation in metal foams," *Scr. Mater.*, vol. 50, no. 2, pp. 295–300, Jan. 2004.

[184] X. Liu, M. N. Rahaman, G. E. Hilmas, and B. S. Bal, "Mechanical properties of bioactive glass (13-93) scaffolds fabricated by robotic deposition for structural bone repair.," *Acta Biomater.*, vol. 9, no. 6, pp. 7025–34, Jun. 2013.

[185] M. Doblaré, J. M. García, and M. J. Gómez, "Modelling bone tissue fracture and healing: a review," *Eng. Fract. Mech.*, vol. 71, no. 13–14, pp. 1809–1840, Sep. 2004.

[186] F. Baino and C. Vitale-Brovarone, "Mechanical properties and reliability of glass–ceramic foam scaffolds for bone repair," *Mater. Lett.*, vol. 118, pp. 27–30, 2014.

[187] S. Sihn and A. K. Roy, "Modelling and prediction of bulk properties of open-cell carbon foam," *J. Mech. Phys. Solids*, vol. 52, no. 1, pp. 167–191, 2004.

[188] M. I. Baker, S. P. Walsh, Z. Schwartz, and B. D. Boyan, "A review of polyvinyl alcohol and its uses in cartilage and orthopedic applications," *J. Biomed. Mater. Res. Part B Appl. Biomater.*, vol. 100B, no. 5, pp. 1451–1457, Jul. 2012.

[189] F. Chen, D.-J. Kang, and J.-H. Park, "New measurement method of Poisson's ratio of PVA hydrogels using an optical flow analysis for a digital imaging system," *Meas. Sci. Technol.*, vol. 24, no. 5, p. 055602, May 2013.

[190] L. Bertolla, I. Dlouhý, and A. R. Boccaccini, "Preparation and characterization of Bioglass®-based scaffolds reinforced by poly-vinyl alcohol/microfibrillated cellulose composite coating," *J. Eur. Ceram. Soc.*, vol. 34, no. 14, pp. 3379–3387, 2014.

[191] O. Peitl, E. D. Zanotto, F. C. Serbena, and L. L. Hench, "Compositional and microstructural design of highly bioactive P2O5-Na2O-CaO-SiO2 glass-ceramics.," *Acta Biomater.*, vol. 8, no. 1, pp. 321–32, Jan. 2012.

[192] A. Bhattacharya and P. Ray, "Studies on surface tension of poly(vinyl alcohol): Effect of concentration, temperature, and addition of chaotropic agents," *J. Appl. Polym. Sci.*, vol. 93, no. 1, pp. 122–130, Jul. 2004.

[193] C. Vitale-Brovarone, F. Baino, and E. Verné, "High strength bioactive glass-ceramic scaffolds for bone regeneration," *J. Mater. Sci. Mater. Med.*, vol. 20, no. 2, pp. 643–653, 2009.

[194] C.-C. Lin, L.-C. Huang, and P. Shen, "Na2CaSi2O6–P2O5 based bioactive glasses. Part 1: Elasticity and structure," *J. Non. Cryst. Solids*, vol. 351, no. 40–42, pp. 3195–3203, 2005.

[195] N. Koga, Z. Strnad, J. Šesták, and J. Strnad, "Thermodynamics of non-bridging oxygen in silica bio-compatible glass-ceramics," *J. Therm. Anal. Calorim.*, vol. 71, no. 3, pp. 927–938.

[196] O. Bretcanu, S. Misra, I. Roy, C. Renghini, F. Fiori, A. R. Boccaccini, and V. Salih, "In vitro biocompatibility of 45S5 Bioglass ® -derived glass-ceramic scaffolds coated with poly(3-hydroxybutyrate)," *J. Tissue Eng. Regen. Med.*, vol. 3, no. 2, pp. 139–148, Feb. 2009.

[197] M. Ben Amara, M. Vlasse, G. Le Flem, and P. Hagenmuller, "Structure of the low-temperature variety of calcium sodium orthophosphate, NaCaPO4," *Acta Crystallogr. Sect. C Cryst. Struct. Commun.*, vol. 39, no. 11, pp. 1483–1485, Nov. 1983.

[198] J. Ando and S. Matsuno, "Ca3(PO4)2 - CaNaPO4 System," *Bull. Chem. Soc. Jpn.*, vol. 41, no. 2, pp. 342–347, Mar. 1968.

[199] S. Jalota, S. B. Bhaduri, and A. C. Tas, "A new rhenanite (beta-NaCaPO(4)) and hydroxyapatite biphasic biomaterial for skeletal repair.," *J. Biomed. Mater. Res. B. Appl. Biomater.*, vol. 80, no. 2, pp. 304–16, Feb. 2007.

[200] W. Holand and G. H. Beall, *Glass Ceramic Technology*. John Wiley & Sons, 2012.

[201] M. Rivenet, O. Cousin, J. C. Boivin, F. Abraham, N. Ruchaud, and P. Hubert, "A study of the Na2O–CaO–P2O5–SiO2 system with respect to the behaviour of phosphate bonded basic refractories at high temperature," *J. Eur. Ceram. Soc.*, vol. 20, no. 8, pp. 1169–1178, Jul. 2000.

[202] R. Narayan, P. Colombo, O. Tatsuki, and Wereszczak, *Advances in Bioceramics and Porous Ceramics: Ceramic Engineering and Science Proceedings, Volume 29 , Issue 7*. John Wiley & Sons, 2009.

[203] F. C. M. Driessens, M. M. A. Ramselaar, H. G. Schaeken, A. L. H. Stols, P. J. Van Mullem, and J. R. De Wijn, "Chemical reactions of calcium phosphate implants after implantationin vivo," *J. Mater. Sci. Mater. Med.*, vol. 3, no. 6, pp. 413–417, Nov. 1992.

[204] W. Suchanek, M. Yashima, M. Kakihana, and M. Yoshimura, "β-Rhenanite (β-$NaCaPO_4$) as Weak Inerface for Hydroxyapatite Ceramics," *Key Eng. Mater.*, vol. 132–136, pp. 2025–2028, 1997.

[205] F. C. Serbena, I. Mathias, C. E. Foerster, and E. D. Zanotto, "Crystallization toughening of a model glass-ceramic," *Acta Mater.*, vol. 86, pp. 216–228, Mar. 2015.

[206] Y. Abe, T. Kasuga, H. Hosono, and K. Groot, "Preparation of High-Strength Calcium Phosphate Glass-Ceramics by Unidirectional Crystallization," *J. Am. Ceram. Soc.*, vol. 67, no. 7, pp. C–142–C–144, Oct. 2006.

[207] J.-J. Kim, Y. Choi, S. Suresh, and A. S. Argon, "Nanocrystallization During Nanoindentation of a Bulk Amorphous Metal Alloy at Room Temperature," *Science (80-.).*, vol. 295, no. 5555, pp. 654–657, Jan. 2002.

[208] A. R. Jamaludin, S. R. Kasim, A. K. Ismail, M. Z. Abdullah, and Z. A. Ahmad, "The effect of sago as binder in the fabrication of alumina foam through the polymeric sponge replication technique," *J. Eur. Ceram. Soc.*, vol. 35, no. 6, pp. 1905–1914, Jun. 2015.

[209] R. Comesaña, F. Lusquiños, J. del Val, F. Quintero, A. Riveiro, M. Boutinguiza, J. R. Jones, R. G. Hill, and J. Pou, "Toward Smart Implant Synthesis: Bonding Bioceramics of Different Resorbability to Match Bone Growth Rates," *Sci. Rep.*, vol. 5, no. April, p. 10677, 2015.

[210] S. M. Salazar Marocho, A. R. Studart, M. a. Bottino, and A. Della Bona, "Mechanical strength and subcritical crack growth under wet cyclic loading of glass-infiltrated dental ceramics," *Dent. Mater.*, vol. 26, no. 5, pp. 483–490, 2010.

[211] I. M. Ward and J. Sweeney, *An Introduction to the Mechanical Properties of Solid Polymers*. John Wiley & Sons, 2005.

[212] B. Feng, Z. Jinkang, W. Zhen, L. Jianxi, C. Jiang, L. Jian, M. Guolin, and D. Xin, "The effect of pore size on tissue ingrowth and neovascularization in porous bioceramics of controlled architecture in vivo," *Biomed. Mater.*, vol. 6, no. 1, p. 015007, Feb. 2011.

[213] M. Bulota, a. S. Jääskeläinen, J. Paltakari, and M. Hughes, "Properties of biocomposites: influence of preparation method, testing environment and a comparison with theoretical models," *J. Mater. Sci.*, vol. 46, no. 10, pp. 3387–3398, 2011.

[214] L. Bertolla, I. Dlouhý, a. Philippart, and a. R. R. Boccaccini, "Mechanical reinforcement of Bioglass®-based scaffolds by novel polyvinyl-alcohol/microfibrillated cellulose composite coating," *Mater. Lett.*, vol. 118, pp. 204–207, 2014.

[215] L. Řehořek, I. Dlouhý, and Z. Chlup, "Tensile behaviour of open cell ceramic foams," *Ceram. - Silikaty*, vol. 53, no. 4, pp. 237–241, 2009.

[216] R. Brezny, D. J. Green, and C. Q. Dam, "Evaluation of Strut Strength in Open-Cell Ceramics," *J. Am. Ceram. Soc.*, vol. 72, no. 6, pp. 885–889, Jun. 1989.

[217] "Wiley: Polyvinyl Alcohol--Developments, 2nd Edition - C. A. Finch." [Online]. Available: http://eu.wiley.com/WileyCDA/WileyTitle/productCd-0471998508.html. [Accessed: 26-Oct-2015].

[218] B. Briscoe, P. Luckham, and S. Zhu, "The effects of hydrogen bonding upon the viscosity of aqueous poly(vinyl alcohol) solutions," *Polymer (Guildf).*, vol. 41, no. 10, pp. 3851–3860, May 2000.

[219] H.-W. Gao, R.-J. Yang, J.-Y. He, and L. Yang, "Rheological behaviours of PVA/H 2 O solutions of high-polymer concentration," *J. Appl. Polym. Sci.*, p. NA–NA, 2009.

[220] S. S. Kim, I. S. Seo, J. H. Yeum, B. C. Ji, J. H. Kim, J. W. Kwak, W. S. Yoon, S. K. Noh, and W. S. Lyoo, "Rheological properties of water solutions of syndiotactic poly(vinyl alcohol) of different molecular weights," *J. Appl. Polym. Sci.*, vol. 92, no. 3, pp. 1426–1431, May 2004.

[221] S. Shafiei-Sabet, W. Y. Hamad, and S. G. Hatzikiriakos, "Rheology of nanocrystalline cellulose aqueous suspensions.," *Langmuir*, vol. 28, no. 49, pp. 17124–33, Dec. 2012.

[222] D. Pacilé, J. C. Meyer, C. O. Girit, and A. Zettl, “The two-dimensional phase of boron nitride: Few-atomic-layer sheets and suspended membranes,” *Appl. Phys. Lett.*, vol. 92, no. 13, p. 133107, Apr. 2008.

[223] G. V. Samsonov, Ed., *Chemical Properties and Analysis of Refractory Compounds / Khimicheskie Svoistva I Metody Analiza Tugoplavkikh Soedinenii / Химические Свойства И Методы Анализа Тугоплавких Соединений*. Boston, MA: Springer US, 1995.

Appendix

The two volumes are the green body (PRE) and the sintered body (POST). The volumes are the largest common box shared between the two reconstructed volumes. They have been coarsely aligned, but have not been aligned using iterative correlation.

Voxel sizes: Pre=3.515um, Post=3.466(5)
*The difference in voxel size along with the shrinkage is responsible for the different image volume sizes
The 'PRE' reconstruction was found to be much noisier, probably due to lower density/attenuation. Because of this, the POST volume was aligned to the PRE volume for coarse alignment between the volumes, rotated in all three axes using interpolation.
The as-reconstructed data was filtered with a non-local means filter in Avizo Fire filter after reconstruction. The search window for both was 41, the similarity value was 0.95, and the local neighbourhood was 5 for the pre volume and 3 for the post volume. The parameters were chosen for best results with trial and error. The local neighbourhood is thought to vary between the two datasets because of the change in feature size with shrinkage, as the change in voxel size is much less, relatively. The filter was applied in 2D to all images reconstructed perpendicular to the rotation axis. The ‘PRE’ volume required more smoothing.

The basic steps for segmentation are described as follows:
Segmentation was performed on the post volume using:
1) Threshold 0.00027
2) Manual Clean (zingers)
3) remove islands 3d, 100pixels
4) Dark material limited threshold of pores

Segmentation was performed on the pre volume using:
1) threshold 0.00014,
2) smooth 3d size 3,
3) smooth all slices
4) Manual Clean (zingers)
5) Dark, material limited, threshold removal of pores 0 to 0.000138
6) remove islands 3d, 100pixels, smooth all slices

The scans were conducted with the following parameters:

POST:
Scan: 200 degree range, 0.16 degree imaging increment, ~19K counts in background
X-ray: 40kV, 200uA target current, solid reflection style W target, no x-ray filtering,
Detector: 250um LuAG:Ce scintillator optically coupled to CCD (2048^2, 15um pixel) with lens mag of 3.2063x
Geometry: X-ray-To-Sample= 33.97mm, X-ray-To-Scintillator=45.85

PRE:
Scan: 200 degree range, 0.16 degree imaging increment, ~16K counts in background
X-ray: 40kV, 200uA target current, solid reflection style W target, no x-ray filtering,
Detector: 250um LuAG:Ce scintillator optically coupled to CCD (2048^2, 15um pixel) with lens mag of 2.9789x
Geometry:X-ray-To-Sample= 34.06mm, X-ray-To-Scintillator=48.79

Reconstruction was performed using shepp-logan filtered back projection, FFT cone beam algorithm (FDK based).

List of publications related to thesis

International conferences

- **Luca Bertolla,** Ivo Dlouhý, Řehořek, Zdeněk Chlup. Tensile properties of open cell ceramic foams. E-MRS 2012 fall meeting, September 17-21, Warsaw, Poland (poster).
- **Luca Bertolla,** Ivo Dlouhý, Lukáš Řehořek, Zdeněk Chlup. Tensile properties of open cell ceramic foams, Fractography of Advanced Ceramics 2012, October 21-24, Stara Lesna, Slovak Republic (oral).
- **Luca Bertolla,** Ivo Dlouhý, Aldo Boccaccini. Mechanical reinforcement of Bioglass®–based scaffolds by novel polyvinyl-alcohol/microfibrillated cellulose composite coating, Fractography of Advanced Ceramics 2014, October 21-24, Slovak Republic (oral).
- **Luca Bertolla,** Ivo Dlouhý, Aldo Boccaccini. Mechanical reinforcement of Bioglass®–based scaffolds by novel polyvinyl-alcohol/microfibrillated cellulose composite coating.13th Conference of the European Ceramic Society, 23-27 June 2013, Limoges, France (oral).
- **Luca Bertolla,** Ivo Dlouhý, Aldo Boccaccini. Preparation and characterization of Bioglass®–based scaffolds Cimtec 2014, 8-13 June 2014, Montecatini Terme, Italy (oral).
- **Luca Bertolla,** Ivo Dlouhý, Aldo Boccaccini. Reinforcement of Bioglass® scaffolds by polyvinyl alcohol/microfibrillated cellulose composite coating. MSE 2014, September 23-25th, Darmstadt, Germany (oral).
- **Luca Bertolla**, Ivo Dlouhý, Aldo Boccaccini. Bioglass® Scaffolds Reinforced by a Composite Polyvinyl Alcohol/Microfibrillated Cellulose Coating MS&T 2014, September 10-12/2014 Pittsburgh, PA, USA (oral).

Journals

- **Luca Bertolla**, Ivo Dlouhý, Lukáš Řehořek, Zdeněk Chlup. Tensile properties of open cell ceramic foams. Acta Metallurgica Slovaca (2013); 3:106–13.
- **Luca Bertolla**, Ivo Dlouhý, Anahí Philippart, Aldo R. Boccaccini. Mechanical reinforcement of Bioglass®–based scaffolds by novel polyvinyl-alcohol/microfibrillated cellulose composite coating. Materials Letters (2014); 118:204–7.
- **Luca Bertolla**, Ivo Dlouhý, Aldo R. Boccaccini. Preparation and characterization of Bioglass®–based scaffolds, Journal of the European Ceramic Society (2014); 34(14):3379–87.
- **Luca Bertolla**, Zdeněk Chlup, Luděk Stratil, Aldo R. Boccaccini, Ivo Dlouhý. Effect of hybrid polymer coating of Bioglass foams on mechanical response during tensile loading, Advances in Applied Ceramics (2015); 114:63–9.